NOTE TO USERS

This reproduction is the best copy available.

UMI®

University of Alberta

INTERNAL WAVE GENERATION FROM A TURBULENT MIXED REGION

by

Kathleen Dohan ©

A thesis submitted to the Faculty of Graduate Studies and Research
in partial fulfillment of the requirements for the degree of

Doctor of Philosophy

in

Applied Mathematics

Department of Mathematical and Statistical Sciences

Edmonton, Alberta

Fall, 2004

Library and Archives Canada

Published Heritage Branch

395 Wellington Street
Ottawa ON K1A 0N4
Canada

Bibliothèque et Archives Canada

Direction du Patrimoine de l'édition

395, rue Wellington
Ottawa ON K1A 0N4
Canada

Your file Votre référence
ISBN: 0-612-95924-4
Our file Notre référence
ISBN: 0-612-95924-4

The author has granted a non-exclusive license allowing the Library and Archives Canada to reproduce, loan, distribute or sell copies of this thesis in microform, paper or electronic formats.

The author retains ownership of the copyright in this thesis. Neither the thesis nor substantial extracts from it may be printed or otherwise reproduced without the author's permission.

L'auteur a accordé une licence non exclusive permettant à la Bibliothèque et Archives Canada de reproduire, prêter, distribuer ou vendre des copies de cette thèse sous la forme de microfiche/film, de reproduction sur papier ou sur format électronique.

L'auteur conserve la propriété du droit d'auteur qui protège cette thèse. Ni la thèse ni des extraits substantiels de celle-ci ne doivent être imprimés ou aturement reproduits sans son autorisation.

In compliance with the Canadian Privacy Act some supporting forms may have been removed from this thesis.

While these forms may be included in the document page count, their removal does not represent any loss of content from the thesis.

Conformément à la loi canadienne sur la protection de la vie privée, quelques formulaires secondaires ont été enlevés de cette thèse.

Bien que ces formulaires aient inclus dans la pagination, il n'y aura aucun contenu manquant.

Canada

Acknowledgements

First of all, I want to thank my supervisor, Bruce Sutherland, who has made my experience the best possible one. Bruce has treated me more like a colleague than a student and has been my support both academically and personally. His advice extends well-past the technical aspects of my research. I have had the opportunity to attend several conferences and workshops, making international connections throughout my degree. I have been successful with scholarships in large part due to his help in grant applications as well as due to the opportunities with which he has provided me. Almost as importantly, I have also experienced the benefits of the social discussion of research.

I have too often taken advantage of his open door and availability. We have shared ideas and he has tirelessly dealt with my almost daily anxieties. Bruce has supported me in my odd hours and let me work in the way that suited my needs, not his own. Bruce shares his life with his students and introduces us to the excitement and sometimes the trials of academia. I find it difficult to fully thank him for all of his effort and I can only hope I can show him his success as a supervisor by following his example in my own career.

I feel very fortunate to have been part of this group. The comaraderie amongst both professors and students makes us the envy of other students in the department. I have learned so much from everyone in the group, both past and present. Paul Choboter was my office-mate, classmate, and sounding-board. Matt Reszka, Morris Flynn, Gordon Swaters, Andrew Bush, and Bryant Moodie have all made the last few years an enjoyable as well as

fulfilling experience. I consider everyone friends as well as continued colleagues.

I also want to thank my family. I have had the amazing experience of never having had to justify my choices, despite numerous years of living as a student. Their strength and grounding have been a consistent part of my life and I cannot imagine how I could have accomplished this degree without their support. They have contributed to my education in so many ways. For example, Dan and Nadia started it all by providing me with a home while I sorted out my applications to graduate school. Mom and Dad have made me feel at home everywhere I have gone with all of their advice, travel opportunities, and interest in my life. Karl and Tamara gave me hope and focus before my candidacy exam by giving me a chance to relax and recharge with them afterwards.

The level of my sanity has been a function of the discussions and distractions of my friends and I very much appreciate their support over the years.

And lastly, I'd like to thank Sarah Gleeson. Without her, this page would not be here.

This work has been supported by the Killam Trust, the Natural Sciences and Engineering Research Council of Canada (NSERC), the Department of Fisheries and Oceans Canada (DFO), and the Alberta Informatics Circle of Research Excellence (iCORE).

Table of Contents

List of Tables

List of Figures

1 Introduction and Motivation 1

1.1 Motivation 1

1.2 Background 4

1.3 Thesis Overview 7

2 Turbulence Measurements 9

2.1 Introduction 9

2.2 Experimental Set-Up and Analysis 10

2.2.1 Apparatus 10

2.2.2 Time Series 12

2.2.3 Determination of Time-Scales 15

2.2.4 Velocity Measurements 20

2.3 Observations 21

2.4 Scaling Theory 26

2.5 Results 28

2.6 Discussion 36

3 Laboratory Experiments with Internal Waves **39**

3.1 Introduction 39

3.2 Experimental Set-Up and Analysis Technique 40

3.2.1 Apparatus 40

3.2.2 Dye-Line Technique 43

3.2.3 Synthetic Schlieren Technique 46

3.3 Qualitative Observations 49

3.4 Quantitative Results 53

3.4.1 Tank-Scale Internal Waves 53

3.4.2 Synthetic Schlieren Results 57

3.5 Discussion 69

4 Numerical Simulations - Large Scale Forcing **71**

4.1 Introduction 71

4.2 Numerical Model 72

4.2.1 Model Description 72

4.2.2 Initial Conditions 74

4.2.3 Damping of the Mixed Region 75

4.3 Observations 76

4.3.1 Wave Fields 76

4.3.2 Time Series 79

4.4 Results 84

4.4.1 Wave Amplitudes with No Rayleigh Damping 84

4.4.2 Wave Amplitudes with Rayleigh Damping 87

4.5 Discussion 91

5 Numerical Simulations - Small-Scale Forcing **93**

5.1 Introduction 93

5.2 Numerical Model 94

5.3 Observations 95

5.3.1 Qualitative Features 95

5.3.2 Length Scales 99

5.3.3 Comparison with Laboratory Experiments 103

5.3.4 Effect of the Interface 105

5.4 Results 107

5.4.1 Wave Amplitudes 107

5.4.2 Frequencies 112

5.5 Discussion 116

6 Discussion **118**

7 Conclusions **121**

Bibliography **125**

A Linear Internal Wave Properties **130**

B Standing Wave Theory **135**

C Calculations of Internal Wave Energy Flux **137**

List of Tables

A.1 Polarization relations for linear inviscid Boussinesq internal waves. 133

List of Figures

1.1 Different time-scales for observations of wave fields. 3

2.1 The experimental set-up. 13

2.2 Vertical time series showing the start of an experiment. 15

2.3 Autocorrelations of time series. 16

2.4 Horizontal time series at several vertical positions. 23

2.5 Vertical time series at several horizontal positions. 25

2.6 Plots of eddy time-scales $\mathcal{T}_2$ as a function of distance from grid. 30

2.7 Comparison of profiles for timescales $\mathcal{T}_2$ and $\mathcal{T}_1$. 31

2.8 Power law dependence of timescale with distance from grid. . 34

2.9 The velocity field. 35

3.1 Experimental set-up for the two methods. 41

3.2 Front views of dye-line experiment. 43

3.3 A sample vertical time series. 44

3.4 Sample vertical time series of an N_t^2 field. 48

3.5 Horizontal time series of the vertical displacement from start position. 50

3.6 Schematic of the two scales of internal waves. 52

3.7 Average amplitudes of contours of the dye-lines. 54

3.8 The variation in A_ξ with buoyancy frequency. 56
3.9 Power spectra of time series. 59
3.10 Average power spectra. 60
3.11 Wave frequencies and wavenumbers with N. 61
3.12 Amplitude measurements of the N_t^2 field. 63
3.13 Amplitude measurements as a function of N. 64
3.14 The relative amplitudes vs. angle of propagation. 65
3.15 Time series of wave decay. 68

4.1 Initial conditions. 75
4.2 Kinetic energy of mixed region. 77
4.3 Wave fields at $t = 3T_{buoy}$. 78
4.4 Sample vertical time series. 79
4.5 Spectrum of vertical wavenumbers in time. 80
4.6 Initial amplitude with depth. 81
4.7 Variation in vertical number with time. 83
4.8 Variation of A_ξ with N. 85
4.9 Variation of A_ξ with time. 86
4.10 Variation of A_ξ with depth. 87
4.11 Variation of A_ξ with F_0. 88
4.12 Variation of A_ξ with N. 89
4.13 Variation of kinetic energy with N. 91

5.1 Instantaneous wave field at $8T_{buoy}$. 96
5.2 Interface structure. 97
5.3 Sample vertical time series. 99
5.4 Vertical profile of horizontal wavenumbers. 100

5.5 Vertical profiles of k_x at increasing times. 102
5.6 Internal wave fields for a laboratory experiment and a simulation. 103
5.7 Vertical time series of the N_i^2 fields. 104
5.8 The effect of a density step. 106
5.9 Amplitude variation with depth. 108
5.10 Variation of amplitude with N. 109
5.11 Wave amplitude vs. forcing amplitude. 110
5.12 Variation of kinetic energy with N. 111
5.13 Power spectrum of the time series. 112
5.14 Frequencies in the vertical. 113
5.15 Variation of wave frequency with N. 114
5.16 Universal energy spectra. 115

Chapter 1

Introduction and Motivation

1.1 Motivation

The Earth's climate is significantly influenced by the meridional transport of heat by the general circulations of both the atmosphere and oceans. It is currently believed that the ocean is responsible for 8% of the transport of heat in the southern hemisphere and 22% in the northern hemisphere [Trenberth and Caron 2001]. The vertical mixing of heat across density surfaces in the ocean is a vital step in ocean circulation. Determining the vertical mixing rate is difficult because ocean models cannot resolve the scales of turbulent motions, and it is impractical to measure the turbulent dissipation rates throughout the oceans. An understanding of the mechanisms of turbulent mixing is necessary in order to parameterize the small-scale processes for use in large-scale ocean models.

Until recently, it was assumed out of simplicity that diapycnal mixing occurred uniformly throughout the ocean interior. A clear contradiction of this assumption was revealed by observations of enhanced mixing in the deep ocean

during the Mid-Atlantic Ridge Tracer Release Experiment, [Polzin et al. 1997; Ledwell et al. 2000] in which large turbulent dissipation rates were found over the rough, steep slopes of the ridge. Egbert and Ray (2000) used satellite altimetry data to estimate the dissipation of tidal energy throughout the oceans and showed that between 25-30 percent of the total tidal dissipation takes place in the deep ocean, generally near areas of rough topography. This deep ocean mixing is a result of the dissipation of internal waves generated by the movement of the tides near these particular areas.

Measurements by Ledwell et al. (2000) have indicated that internal tides play a major role, although it is uncertain as to where in the water column the mixing occurs [Garrett and St.Laurent 2002]. The turbulence over rough topography may be responsible for additional generation of internal waves and may add to the enhanced mixing.

The emphasis on the properties of the observed wave field generated by flow over bottom topography vary with the observation time, as depicted in the schematic of Figure 1.1. Over very long times relative to the inertial period ($t_{obs} \gg T_{inertial}$, where $T_{inertial} \equiv 2\pi/f$ and f is the Coriolis frequency) the long-term properties of the internal tides can be observed. Over intermediate times, on the order of a day, the tidal flow can be viewed as uniform flow over topography. On very fast time scales, such as hours or minutes, the details of the small-scale processes such as turbulence generated by flow over rough topography can be observed.

Much attention has been devoted to the investigation of the tidal conversion from both supercritical and subcritical topography (*e.g.* recently by Llewellyn Smith and Young (2002), Balmforth, Ierley and Young (2002) and St. Laurent and Garrett (2002)). Here we discuss the possibility of the third generation

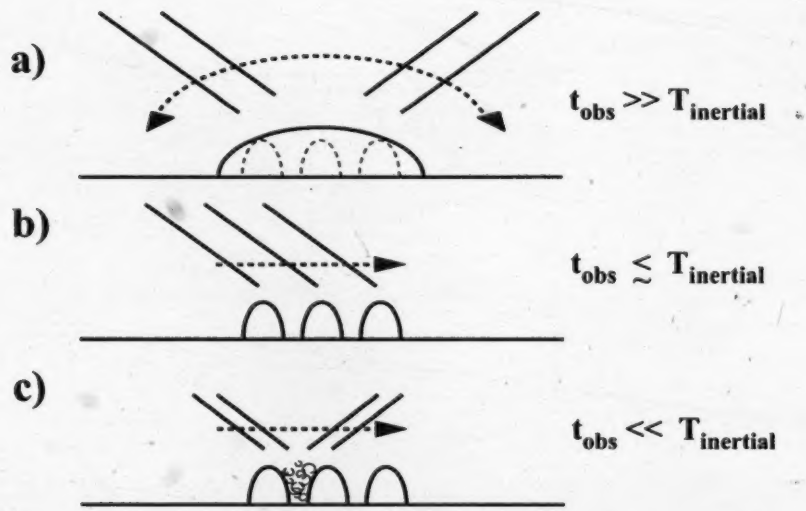

Figure 1.1: Different time-scales for observations of wave fields. a) Time-scales of observations, t_{obs}, longer than the inertial period result in measurements of average statistics of internal tides. b) On time-scales on the order of the inertial period, the motion of the tides can be locally viewed as uniform flow over topography, with internal waves viewed as lee waves. c) On very short observation time scales, the small-scale generation mechanisms can be considered.

situation depicted in Fig. 1.1c, in which non-hydrostatic internal waves are generated from the turbulent eddies.

Turbulent regions adjacent to stably stratified regions in which internal waves may propagate are a common occurrence in geophysical flows. For example, the oceanic boundary layer is a turbulent layer overlying the seasonal thermocline and it has been suggested that internal waves generated at the base of this region may act as a source of energy driving deep ocean equatorial currents [Sutherland 1996]. Munk and Wunsch (1998) estimated that wind-generated internal waves may provide half of the energy needed for mixing the ocean interior. Although inertial waves created by large motions such as

severe storms are likely the main source of energy, the generation of small-scale waves and the role they play in momentum and energy transport remain poorly understood.

The goal of this work is to elucidate some of these small-scale processes through laboratory experiments and numerical simulations.

1.2 Background

Though much has been learned about the dynamics of homogeneous, isotropic turbulence that is uniformly forced, in many physical systems turbulence is generated at a localized source and is affected by the presence of rigid boundaries. The decay with distance from a source is examined in wind tunnel ("grid generated" turbulence) experiments [Comte-Bellot and Corrsin 1971; Tennekes and Lumley 1972] and mixing box experiments ("oscillating grid" turbulence) [Turner 1973]. In wind tunnel experiments, a uniform mean flow passing through a mesh creates locally homogeneous turbulence in planes parallel to the mesh. The turbulence decays with distance from the mesh and, by the Taylor hypothesis, with time as it is transported by the mean flow away from the source. Examination of the statistical properties of turbulence in these experiments is useful, for example, in examining turbulent wakes behind moving objects.

Mixing box experiments are useful in understanding the properties of turbulence in circumstances where there is no mean flow. The experiments are performed in an enclosed tank and fluid is supplied continuously with turbulent kinetic energy generated by rapid vertical oscillations of a horizontal grid of bars. As in wind tunnel experiments, the turbulence is shear-free, and

approximately horizontally isotropic and homogeneous. Unlike wind tunnel experiments, however, the supplied energy remains contained within the finite volume of the box. Steady state is achieved through a balance between the energy supplied and the energy lost internally and at the boundaries.

A large body of work has been devoted to investigating the spatial decay of turbulence in mixing box experiments such as the work of Thompson and Turner (1975) and Hopfinger and Toly (1976). They found the following scaling dependence upon depth, z, measured from a virtual origin which lies close to the grid:

$$l \sim z, \tag{1.1}$$

$$u \sim Kz^{-1}, \tag{1.2}$$

where l is the integral length scale of the turbulence, u is the root-mean-square horizontal velocity, and K, determined by Long (1978a), parameterizes the turbulent production by the grid. K depends on viscosity, ν, as well as the stroke length, frequency, and mesh size of the oscillating grid (S, f and M). For an oscillating grid with square bars, $K \sim fS^{3/2}M^{1/2}$, whereas for cylindrical bars, $K \sim (SfM/\nu)^{1/3} fS^{3/2}M^{1/2}$.

Their experiments were performed in mixing boxes with a square horizontal cross-section and analyzed mostly with the use of single-point measurements, such as laser-Doppler anemometry or hot-wire probes.

In the first of our investigations, we use a mixing box with a high aspect ratio to investigate the effects of the bottom boundary on the scalings within a turbulent region, in the absence of an underlying stratified layer.

In two classic laboratory experiments, Linden (1975) and E and Hopfinger (1986) examined the deepening of a grid-generated turbulent mixed layer.

In both studies, the entrainment rates were compared for two-layer and continuously stratified fluids, and the internal wave properties were measured from trajectories of suspended particles viewed by slit lighting. Linden found that the deepening rates were reduced by $10 - 50$ percent when the region adjoining the mixed layer was stratified and could therefore support internal waves. He calculated that a significant portion of the energy available at the turbulent interface could be lost to internal waves. E and Hopfinger considered the variation in entrainment rate, E, with the local Richardson number, $\mathrm{Ri} = g\Delta\rho l/\overline{\rho}u^2$, where $\Delta\rho$ is the density jump across the interface, $\overline{\rho}$ is the density in the mixed region, and l and u are the integral length-scale and root-mean-square (rms) velocity of the turbulence. They found that the entrainment rate followed a power law relation of $E = K\mathrm{Ri}^{-n}$, with $K \approx 3.8$ and $n \approx 1.5$, for both two-layer and continuously stratified experiments, and thereby concluded that the entrainment rate was not affected by the radiation of energy by internal waves. In both cases internal waves were observed, although the conclusions on the significance of the internal wave radiation of energy to the deepening of the mixed layer differed.

The emphasis of the majority of past oscillating-grid studies has been on the properties of the turbulent region such as examining the structure of turbulence at a density interface for either two-layer, three-layer, or continuously stratified fluids [Crapper and Linden 1974; Kit, Strang and Fernando 1997] or examining the entrainment rate across a density interface [Linden 1975; Hopfinger and Toly 1976; Fernando and Long 1983; E and Hopfinger 1986].

The properties of waves generated in the thin interface between a turbulent layer and the adjoining region have been studied experimentally [Hannoun and List 1988; Perera, Fernando and Boyer 1994; McGrath, Fernando and

Hunt 1997] and theoretically [Fernando and Hunt 1997]. There has been some theoretical work by Carruthers and Hunt (1986) and numerical studies by Briggs et al. (1998) studying the propagating internal waves from a turbulent region into an adjoining stratified region, but few experimental measurements of the wave properties have been made.

In the second of our investigations, we have used laboratory experiments to examine the properties of an internal wave field in a stably stratified region below a turbulent mixed layer. The wave field is excited by the eddies within oscillating-grid generated turbulence.

Lastly, we complement the laboratory experiments with numerical simulations of a mixed layer overlying a stratified region. We directly compare the qualitative features and trends of the wave field generated in the laboratory experiments with the numerical simulations as a step to understanding the general properties of turbulence-generated waves.

1.3 Thesis Overview

The thesis is organized as follows: In Chapter 2 we describe the laboratory experiments on turbulence scalings using oscillating-grid turbulence. We develop a new method to visualize and measure the eddy scales within the turbulence. We show how the eddy scalings within a turbulent region are sensitive to the position of a bottom boundary.

We extend the mixing box experiments from a turbulent region which fills the tank to one that overlies a uniformly stratified region in Chapter 3. The properties of internal waves which are generated from the turbulent layer are examined.

In Chapters 4 and 5 we use numerical simulations of a mixed layer overlying a uniformly stratified layer to continue the investigation into the wave properties. In Chapter 4 the mixed layer is forced with two counter-rotating vortices and in Chapter 5 the mixed layer is forced with small-scale random noise. In Chapter 6 and 7 we summarize and discuss the results of both laboratory experiments and numerical simulations.

Descriptions of internal wave properties are provided in the appendices. In Appendix A are properties of propagating internal waves and in Appendix B are properties of standing waves. In Appendix C are energy flux calculations for the internal waves in the simulations.[1]

[1]Aspects of this material have been published; see Dohan and Sutherland (2002) and Dohan and Sutherland (2003).

Chapter 2

Turbulence Measurements

2.1 Introduction

In the experiments reported upon here we use a mixing box with a high aspect ratio (approximately 5:1) horizontal cross-section in order to investigate the effects of the bottom boundary on the scalings within a turbulent region. As well as enabling a study of the effect of horizontal confinement upon the turbulence dynamics, the tank geometry allows us to employ a new technique to visualize and measure statistical properties of the entire turbulent flow field. This technique uses pearlescent dye and digital image processing to measure eddy time-scales as a function of the distance from the oscillating grid throughout the flow field. This technique also provides a new method to measure eddy velocities in the turbulence.

The purpose of this chapter is to use this technique to investigate the effects of the high aspect ratio geometry and the position of the bottom boundary upon the spatial dependence of turbulence time-scales in a homogeneous fluid. The details of the analysis technique will be first described, and the eddy time-

scale results and velocity measurements will then be related to scaling theory for eddy time-scales.

2.2 Experimental Set-Up and Analysis

2.2.1 Apparatus

Experiments were performed in an acrylic tank of horizontal dimensions $W = 9.7\,\text{cm}$, $L = 47.6\,\text{cm}$ and of height $H = 49\,\text{cm}$, as shown in Figure 2.1a. The horizontal cross-section had a high aspect ratio compared with conventional experiments performed in tanks with square cross-sections. An acrylic "false bottom" was inserted horizontally at different levels so that the structure of turbulent eddies in fluid of different depths could be examined. The tank was filled with water up to 2 cm from the top of the tank. A stainless steel mixer was inserted 7 cm from the top of the tank, and 5 cm below the free surface of the water. The mixer was a ladder-shaped square grid of cylindrical bars of diameter 0.6 cm spaced 3.2 cm apart (solidity 27%) with 'rungs' that extended beyond the struts of the ladder so the ends of the bars extended to within 2 mm of the walls. The rungs extended 0.9 cm along the length and 2.6 cm along the width of the tank. When switched on, the mixer moved vertically up and down with a frequency of 7 Hz and with a peak-to-peak stroke length of 2.6 cm.

A digital camera was positioned a distance $L_{camera} \approx 3\,\text{m}$ from the tank as shown in Fig. 2.1b. Black paper was fastened to the rear wall of the tank. A bank of fluorescent lights illuminated the interior of the tank through its left side from the point of view of the camera.

Figure 2.1a illustrates the co-ordinate system used in the discussion that follows: the downward distance from the mean grid position is denoted by δz, which increases from zero at the mean vertical position of the mixer to the depth D ($\leq 42\,\mathrm{cm}$) at the position of the false bottom; x is the distance from the left side; y is the distance from the front side of the tank, with respect to the camera's point of view.

The turbulent region was visualized using pearlescent dye (Mearlmaid Natural Pearl Essence AA). Unlike typical dye-tracking techniques that identify motion by tracking the Lagrangian transport of the dye, pearlescence visualizes motion even when the dye is uniformly distributed throughout the fluid. Natural Pearlescence is composed of microscopic ($30 \times 6\,\mu\mathrm{m}$) reflective crystals obtained from fish scales. The crystals scatter light evenly throughout a stationary fluid, but align due to the eddy-induced shear once the fluid is in motion. This alignment visualizes the large turbulent eddy motions by reflecting the incident light in bright patches.

Although the specific gravity of the particles is 1.6, they are sufficiently small that their effect upon the flow is negligible. For example, the Stokes velocity of a falling sphere with the same density and with a diameter of $30\mu\mathrm{m}$ is $0.03\,\mathrm{cm/s}$. This speed, which overestimates that of a falling plate, is a small fraction of the observed flow speeds. Likewise, the time over which co-aligned plates decorrelate due to Brownian processes is very large compared with the turbulence time-scales.

Visualization of turbulence by reflective particles has been exploited, for example, by Voropayev and Fernando (1996), who used pearlescence, and by Dickinson and Long (1978), who observed turbulent fronts using suspended aluminum particles. An added advantage of our technique is that we not only

visualize turbulent eddies, but we also compute eddy time- and length-scales from digitized images of the experiments.

The pearlescent dye was injected along the surface of the tank prior to the start of the experiment. After the mixer was turned on, the mixing region deepened and the dye was passively transported by the turbulent eddies. Thus the dye simultaneously revealed the depth of the mixed region and the characteristics of the eddies themselves.

The images recorded by the digital camera are a weighted superposition of the turbulent motions across the width of the tank. Though the strongest signal came from eddies near the front of the tank, experiments performed with a collimated beam 1 cm wide illuminating the centre of the tank gave the same statistical results as those with the side wall fully illuminated. Thus, the camera predominantly recorded images of the interior eddy motions which were highlighted by the pearlescent dye, not the motions in the boundary layer of the front wall.

The recorded images in the $x - z$ plane were analyzed using the image processing software package, DigImage [Dalziel 1993]. Snapshots of the experiment were digitized, enhanced, and analyzed using statistical methods. These methods are described in the subsections below.

2.2.2 Time Series

A vertical time series is constructed by extracting a column of pixels at successive times from digitized images of the experiment as it evolves. The columns are positioned side by side to form a time series image. The time series can be constructed with a temporal resolution as small as 1/30 th second (limited by

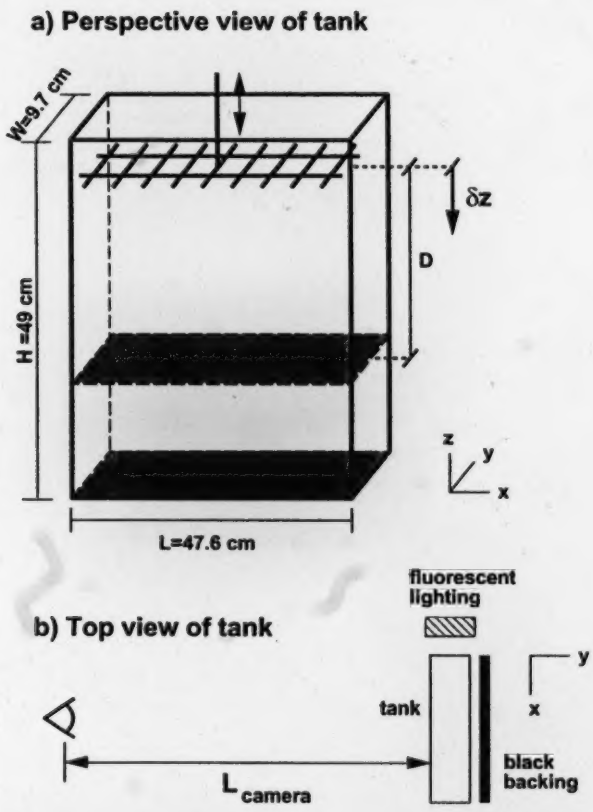

Figure 2.1: The experimental set-up. a) Perspective view of the tank. The distance down from the midplane of the grid is denoted δz and the location of the replaceable bottom is at $\delta z = D$. b) Top view, showing the relative positions of the lighting, tank and camera.

the standard NTSC video frame rate). Up to 31 vertical time series (taken at 31 different horizontal positions) can be taken simultaneously. Likewise, one can construct horizontal time series.

Figure 2.2 shows a vertical time series for one minute of an experiment with $D = 42\,\text{cm}$. The image is enhanced by representing intensities with a false colour gray scale. The image shows the evolution of the mixing region along a vertical slice taken at a horizontal position $x = 16\,\text{cm}$ from the left

side of the tank and starting when the mixer is initially set in motion. The deepening of the mixed layer is marked by the vertical extent of the pearlescent dye which is initially at the level of the mixer and is transported downward as the turbulent region deepens. The figure shows that the mixed region deepens over the full depth of the tank after approximately 40 s. This time is consistent with that predicted by Dickinson and Long (1978; 1983).

While deepening, the mean intensity of light incident upon the camera decreases as the pearlescent dye is diluted. The variations from the mean reveal eddy motions. A bright streak in the time series indicates the presence of an eddy in the field of view of the raw time series image. In particular, the dye shows an increase in turbulent eddy time-scales from the top to the bottom of the mixed region: the streaks are broader at the bottom of the image. In this way, the width in time of any particular streak is a measure of the corresponding eddy turnover time and the slope of the streak measures the local vertical velocity in the turbulence. In a similar fashion, the horizontal velocities and time-scales can be determined from horizontal time series.

Vertical time series are taken from the experimental images with a time step of 1/15 s and a duration of 30 s. This duration is chosen as a compromise between resolving the fast eddy motions and acquiring enough data for sufficient time-averaging. In order to ensure that the time series includes only the fully developed turbulence in statistically steady state, the time series are taken one minute into the experiment. The vertical extent of the time series is chosen to include the turbulent region of the time series while avoiding the mixer and the tank boundaries. Each time series is then passed through a high-pass Fourier filter in the horizontal direction to subtract the mean intensity from the digitized images. This removes the effects of light attenuation

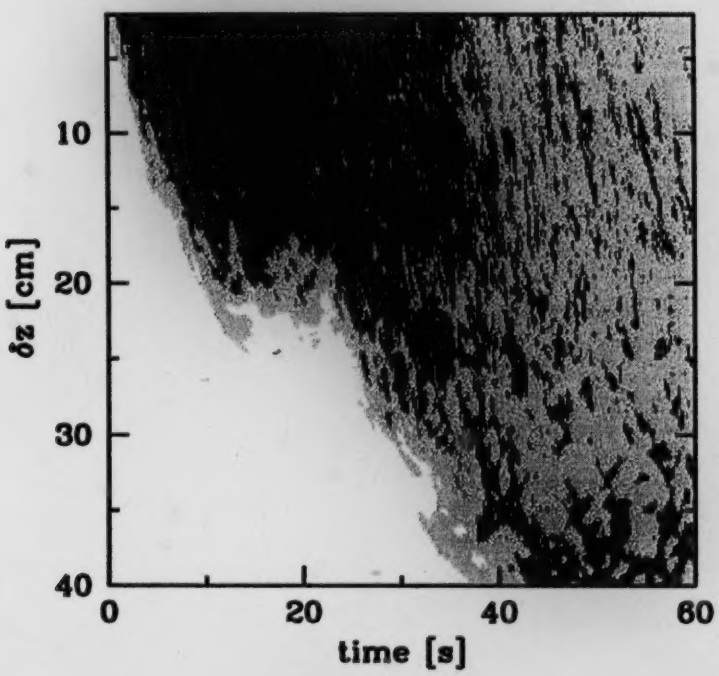

Figure 2.2: Vertical time series showing the start of an experiment, taken 16 cm from the left edge of the tank. The field of view extends from just below the oscillating grid to the bottom boundary. A false colour scheme is used to display the image, with black representing the strongest intensities, grays representing weaker intensities, and white representing the weakest intensities.

across the tank so that the resulting average intensity of each time series at each horizontal position is the same. Figure 2.3a shows a time series after these enhancements, displayed as a false colour representation of the image.

2.2.3 Determination of Time-Scales

We have used autocorrelations of intensity functions derived from (filtered) vertical time series to measure the eddy time-scale as a function of the distance from the grid.

We define a discrete function $f_{\&}(t_n)$ as the variation in intensity over time

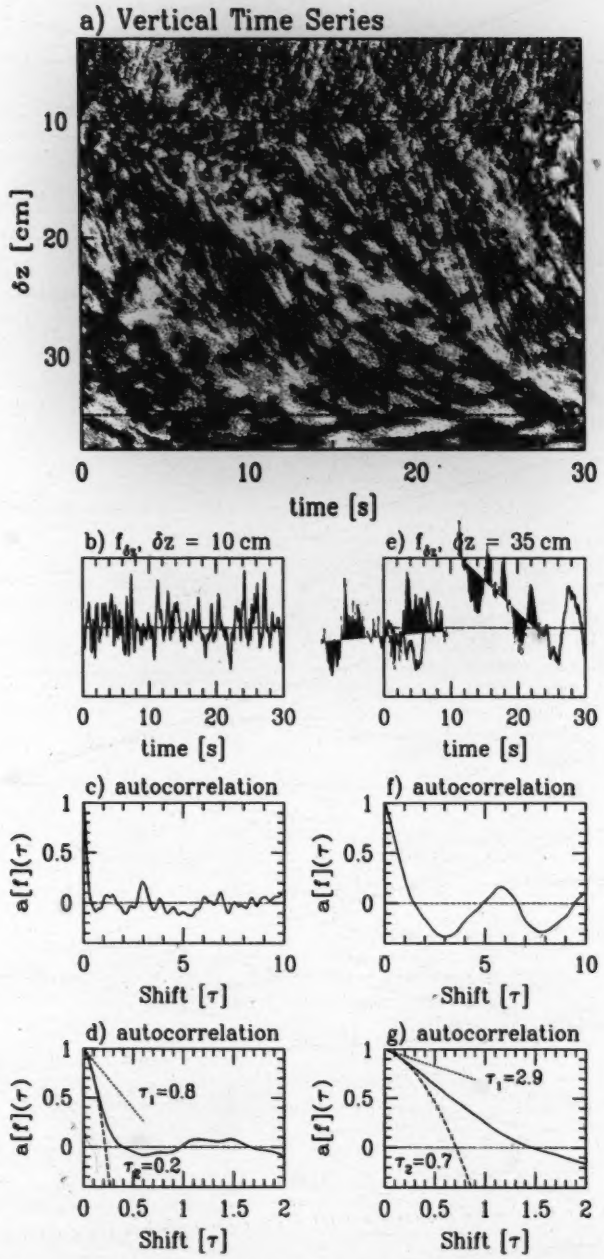

Figure 2.3: a) Vertical time series taken at $x = 16\,\text{cm}$ in an experiment with $D = 42\,\text{cm}$. The time series is started at $t = 60\,\text{s}$. The same gray scale as in Fig. 2.2 is used. b) Intensity plot in time at location 10 cm below grid. c) Normalized autocorrelation of Fig. 2.3b). d) Autocorrelation and tangent near shift $\tau = 0$. Fig. 2.3 e)-g): Corresponding functions at location 35 cm below grid.

at the vertical position δz from a vertical time series, where n is the (integer) time index. Explicitly, $t_n = n\Delta t$ for $n = 0, 1, \ldots, N$, where Δt is the temporal resolution of the time series. Figures 2.3b and e show typical profiles $f_{\delta z}(t_n)$ for $\delta z = 10\,\text{cm}$ and $35\,\text{cm}$, respectively. Both are taken from the time series in Fig. 2.3a along the cross-sections marked by the horizontal dotted lines. The location of strong eddies, marked as black in the time series image, show up as peaks in the intensity functions. The increase in eddy time-scale with distance from the grid is evident: the peaks at $\delta z = 35\,\text{cm}$ are much wider than those at $\delta z = 10\,\text{cm}$.

In general, for a discrete signal $f(t_n)$, the autocorrelation is a discrete function of the (stepwise) temporal shift $\tau_i \equiv i\Delta t$ defined by

$$A[f](\tau_i) = \sum_{n=i}^{N} f(t_n) f(t_n - \tau_i), \quad \tau : i = 0, 1, \ldots, N. \tag{2.1}$$

The normalized autocorrelation is defined by $a[f](\tau) = \frac{A[f](\tau)}{A[f](0)}$. It is invariant to changes in scale of a function but is sensitive to a shift in the mean value. By setting the mean intensity to zero in each filtered time series, this sensitivity is removed.

Figures 2.3c and f show the corresponding normalized autocorrelation functions of the signals in Figs. 2.3b and e, respectively. The narrow peaks in Fig. 2.3b result in a rapid decorrelation of the signal (the autocorrelation drops to zero within a small time shift). The wider peaks in Fig. 2.3e result in a slower decorrelation.

To characterize the eddy time-scale we define two time-scales based upon the behaviour of the autocorrelation function at $\tau = 0$.

We define the time-scale based on the instantaneous change in the auto-

correlation function about $\tau = 0$ to be

$$\mathcal{T}_1 = -\left(\frac{d\, a[f](\tau)}{d\tau}\bigg|_{\tau=0} \right)^{-1}. \tag{2.2}$$

Time-scale $\mathcal{T}_1$ is an accurate measure of the widths of the peaks of an approximately piecewise constant function, but the time-scale varies significantly as the discontinuities of the function become less pronounced and the changes from positive to negative values become more gradual. In fact, the tangent to the autocorrelation at $\tau = 0$ of a continuous function is horizontal, and $\mathcal{T}_1$ becomes infinite. For discrete signals, the derivative is calculated from the first three points of the autocorrelation and is zero only in the continuous limit.

The autocorrelation of a continuous time series has strictly negative curvature near $\tau = 0$. The first three terms in the Taylor series expansion of $a[f](\tau)$ about $\tau = 0$ are given by $1 + a_1\tau + a_2\tau^2/2$, where $a_1 = da[f](0)/d\tau$ and $a_2 = d^2a[f](0)/d\tau^2$. We can then define a second time-scale as the τ-intercept of this quadratic approximation to the value of $a[f](\tau)$. Explicitly,

$$\mathcal{T}_2 = \frac{-a_1 - \sqrt{a_1^2 - 2a_2}}{a_2}. \tag{2.3}$$

The time-scale definition (2.3) is similar to the definition of the Taylor microscale for isotropic turbulence as described in Hinze (1959) although the functions that we are examining, rather than turbulence velocity components, are intensity functions which are related to the local shear in the flow.

If the signal is a piecewise constant function (as for a rapidly varying discretely sampled signal), $\mathcal{T}_1$ time-scale is the appropriate time-scale. $\mathcal{T}_2$ is the appropriate time-scale for a smoothly varying function and measures the char-

acteristic width of the dominant peaks for a triangular wave. In particular, for a rectangular wave with period T, we find $\mathcal{T}_1 = T/4$. For a triangular wave with period T, we find $\mathcal{T}_2 = \sqrt{6}T/12$.

The autocorrelation functions in Figs. 2.3c and f are redrawn on a small τ-scale in Figs. 2.3d and g, respectively. The tangents to $a[f](\tau)$ at $\tau = 0$ are superimposed as the dotted lines. The corresponding time scales $\mathcal{T}_1$ are the intercepts of these lines with the τ-axis. The second order approximations to the curves are plotted as the dashed lines. Note that $\mathcal{T}_1$ gives consistently higher values than $\mathcal{T}_2$ and that the intercepts of both time-scale curves with the τ axis are larger in the case $\delta z = 35\,\mathrm{cm}$ (Fig. 2.3g).

Using either method, a profile of time-scale value as it varies with distance from the midplane of the grid can be assembled for each time series by calculating the time-scale associated with the intensity functions $f_{\delta z}(t_n)$ at increasing values of δz. A similar method could be used to determine the length-scale in the turbulence at the time t_0 using functions of position $f_{t_0}(z_n)$, $z_n = \delta z_0 + n\Delta z$, where Δz is the spatial resolution of the vertical time series.

The integral time-scale (the integral of the normalized autocorrelation function) is the standard time-scale for turbulence measurements. This time-scale is inappropriate for our data since it assumes a negligible contribution to the integral from shifts far from the origin, whereas with our data non-negligible contributions to the integral will occur when two eddies overlap. This results in significant peaks in the autocorrelation function far from the origin, as seen in Figs. 2.3c and f. Similarly, the first zero-crossing is not used as a time-scale since contributions from overlapping eddies may result in secondary peaks prior to the occurrence of the zero-crossing.

Another standard technique in turbulence measurements is the Fourier

transform. This method is also not applicable to our time series data. Results show that although there is a high-frequency cut-off at each vertical level, the edge of the cut-off is ambiguous and the power in the signal is spread throughout the lower frequencies without any clear peaks.

2.2.4 Velocity Measurements

To measure velocity, consider two time-discretized signals $f_0(t_n)$ and $f_j(t_n)$, $n = 0, \pm 1, \pm 2...$ where, for notational convenience, $f_0 \equiv f_{\delta z_0}$ and $f_j \equiv f_{\delta z_j} = f_{\delta z_0 + j\Delta z}$. The cross-correlation is defined as a function of the temporal shift $\tau_i \equiv i\Delta t$ given by

$$C[f_0, f_j](\tau_i) = \sum_{n=\max(0,i)}^{\min(N,N+i)} f_0(t_n) f_j(t_n - \tau_i) \tag{2.4}$$

where $|i| \leq N$.

Eddies advected by a background flow appear as diagonal streaks in a vertical time series, the slopes of which provide the local background vertical velocities. Similarly, the slopes of streaks in a horizontal time series provide the local background horizontal velocities in the turbulence.

To extract the vertical velocity information from a vertical time series, a reference signal $f_0(t_n)$ is chosen as the intensity function at the position δz_0 in the time series taken along a vertical cross-section at $x = x_0$. Neighbouring signals $f_{-i}(t_n)$ and $f_i(t_n)$ are cross-correlated with $f_0(t_n)$ for a prescribed integer shift i. The smallest value τ at which $C[f_0, f_{-i}](\tau)$ is maximal is denoted by τ^-. Similarly τ^+ is the time shift for which $C[f_0, f_{+i}](\tau)$ is maximum. In practice, the critical points τ^+ and τ^- are each determined by quadratic in-

terpolation of C from three points about $\tau = 0$. Finally, the average vertical velocity at δz_0 is estimated from the second order accurate derivative at $\tau = 0$ (hence where $\delta z = \delta z_0$) for the function that passes through the three points $(\tau^-, \delta z_0 - i\Delta z)$,$(0, \delta z_0)$, $(\tau^+, \delta z_0 + i\Delta z)$. Explicitly,

$$v(x_0, \delta z_0) = \frac{-i\Delta z}{(\tau^+ - \tau^-)} \left(\frac{\tau^+}{\tau^-} + \frac{\tau^-}{\tau^+} \right) \tag{2.5}$$

This procedure is used to evaluate the vertical velocity at every vertical position, δz, along the time series. A Gaussian-weighted filter is used to determine the mean vertical velocity at a subset of vertical positions. Likewise, horizontal time series are used to determine horizontal velocities, and these are locally averaged to determine their values at the same spatial co-ordinates as the vertical velocities. Thus the velocity vector field is produced. In cases for which the mixing region exhibits a background circulation on a time-scale longer than that of the turbulent eddies, the above method may be used to measure the velocity of the background flow. The technique effectively filters the fast time-scale of the eddy motions and so provides an efficient method for determining the long-time behaviour of the flow.

2.3 Observations

When the mixer was set in motion tiny jets and vortices were shed from the bars of the grid. Near the grid were small, fast eddies. Further below the grid the eddies persisted for longer times as they coalesced to form larger eddies and as viscosity damped the motion on small length- and time-scales. Depending upon the total depth of the tank, D, these eddies were further modified by a

large-scale circulation that developed in the tank. If $D \gg W$, we observed that an overall circulation developed in the form of a pair of counter-rotating vortices oriented with vorticity vectors directed along the y-axis (perpendicular to the long side of the tank). This circulation occurred in experiments with large values of D.

A sequence of horizontal time series for an experiment with $D = 42\,\text{cm}$ is shown in Figure 2.4. Figure 2.4a shows a horizontal time series taken at $\delta z = 6\,\text{cm}$, with each subsequent time series taken 4 cm further below the grid. The increase in horizontal eddy length-scales is evident in the images. Near the bottom of the tank, the eddies are on the order of 2-3 cm. The overall circulation pattern can be detected from these images. A streak with a shallow slope corresponds to fast horizontal advection of an eddy, a negative slope corresponds to motion to the left and a positive slope corresponds to motion to the right of the tank. In all horizontal time series, except the two nearest the grid, there is a symmetric divergence of fluid from the centre of the tank toward the sides. As expected, at the edges there is almost no detectable horizontal motion. Near the grid (*e.g.* Fig. 2.4a) eddies exhibit less coherent fluctuations.

In experiments with $D \gg W$ the typical variations in vertical motions across the tank are illustrated in the nine vertical time series shown in Figure 2.5 (from the same experiment as Fig. 2.4). The time series are taken starting 3.8 cm from the left side of the tank and are spaced 5 cm apart. As in Fig. 2.4, the increase in eddy time-scales and length-scales from the top to bottom of the tank is evident from the plots. The plots also show a change in vertical motions from large upward velocities at the sides (apparent by the positive slopes of the streaks), through a transition to downward velocities

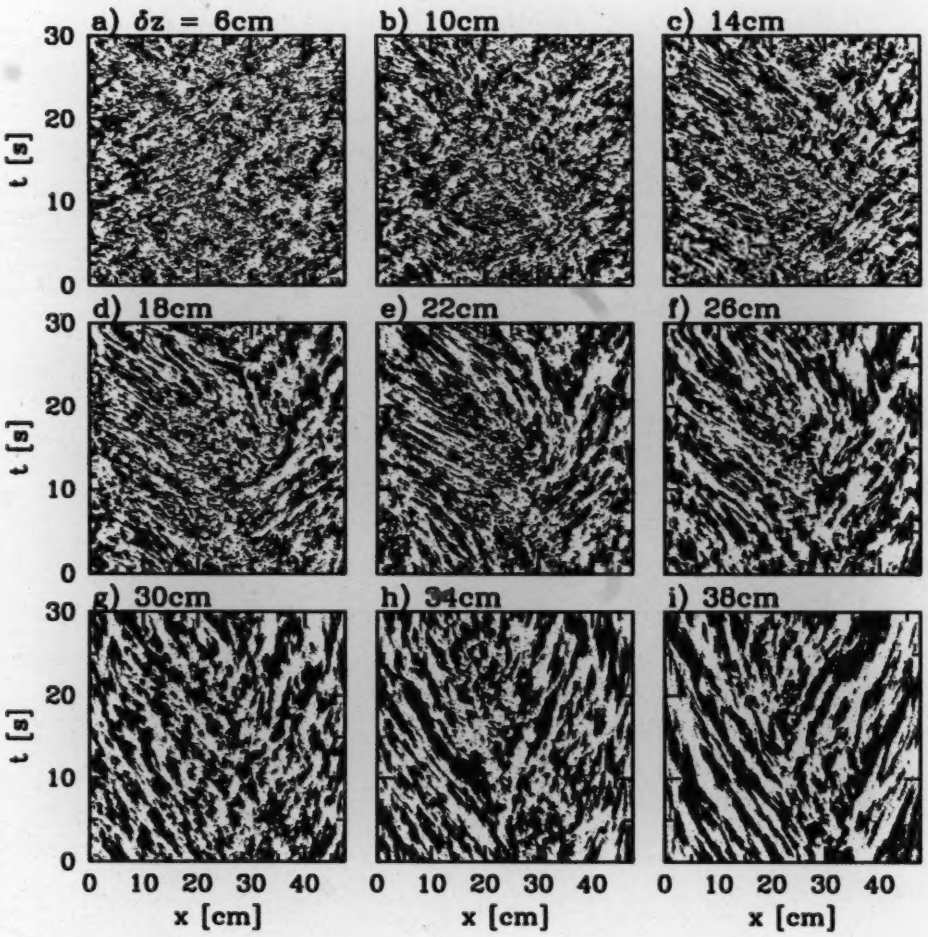

Figure 2.4: Horizontal time series for an experiment with $D = 42\,\text{cm}$ taken at locations 6 cm to 38 cm below grid, every 4 cm. A divergence from the center of the tank to the sides is evident from the symmetric diagonal streaks of fluid. Intensities below the mean intensity value are marked as white, above the mean as gray.

near the middle of the tank (apparent by the negative slopes). Although there are significant vertical motions throughout the tank, the fastest motions occur in the top half of the tank.

The two sets of time series illustrate the typical overall circulation which moved down the middle of the tank, left and right toward the sides, and rapidly upward along a thin boundary layer extending approximately 2 cm from the side walls (with no mean flow along the front and back walls). Smaller scale eddies were embedded within this overall circulation, and their associated time-scales increased with distance away from the grid. This circulation was a robust feature of experiments with $D \gg W$. On a slower time-scale, transient upwelling near the centre of the tank was also sometimes observed. In experiments with large D, fluid upwelled from the bottom over significant patches far from the side walls. This upwelling phenomenon became more pronounced in experiments with progressively larger values of D, and the circulation pattern organized to form two counter-rotating cells as previously described.

In experiments where D was comparable to W, a large-scale circulation did not develop except within a small region at the side walls near the oscillating grid. Furthermore, the structure of the eddies embedded within the large-scale circulation changed as D varied. For $D \approx W$ the turbulence appeared to be approximately horizontally homogeneous.

These circulation patterns occurred whether the mixed region was bounded below by a rigid wall or by a deformable interface between the turbulent fluid and unmixed fluid of larger density. We ascribe the transition of the circulation pattern as D increased to a change between the turbulence behaving as though fully three-dimensional, if $D \approx W$, and quasi-two-dimensional, if $D \gg W$. In the latter case, the high horizontal aspect ratio of the tank restricted the

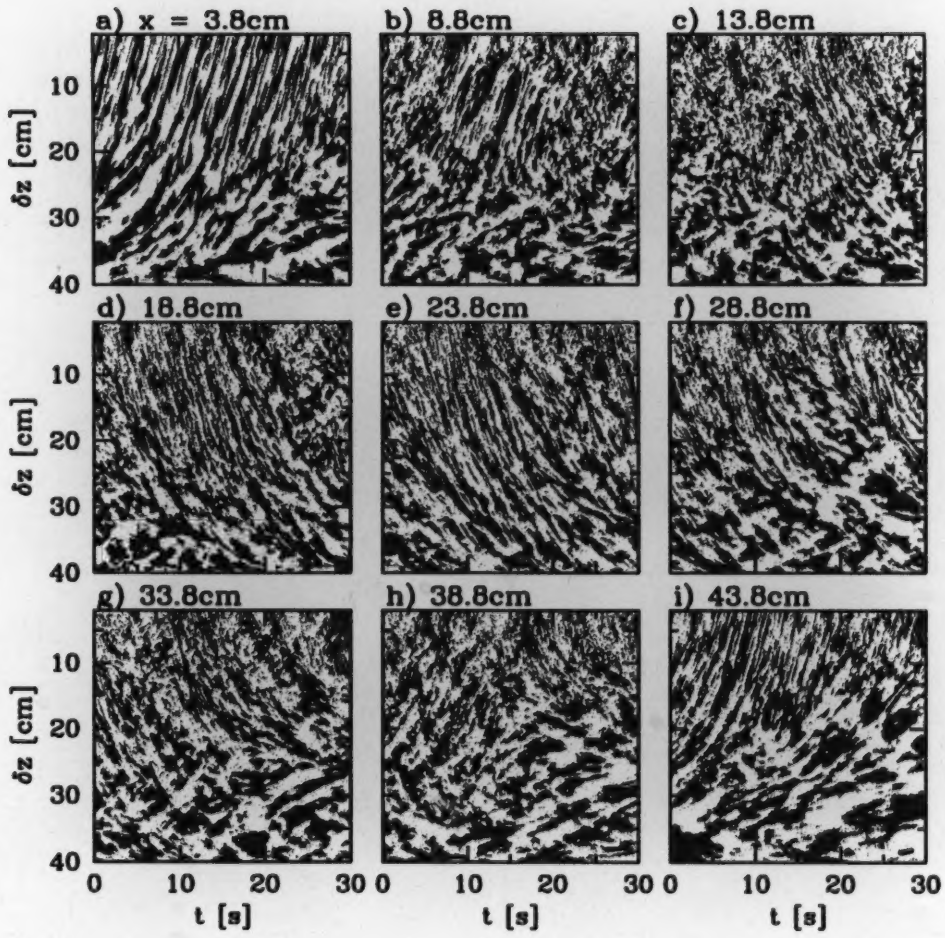

Figure 2.5: Vertical time series for an experiment with $D = 42\,\text{cm}$ taken every 5 cm across the front of the tank, starting 3.8 cm from the left edge of the tank. Streaks with positive slopes indicate upward motion of fluid, seen at the sides of the tank, and negative slopes indicate downward motion in the center of the tank. The gray scale is defined in the same way as in Fig. 2.4.

development of isotropic eddies to length-scales smaller than W. However, if D was large, turbulent motions with length-scales larger than W acted as if they were two-dimensional. That is, there was no mean flow along the front and back tank walls. This circulation may have been enhanced by the relatively high grid frequency (7 Hz), which was the critical frequency at which secondary motions occurred in the experiments of McDougall (1979). The secondary motions were not, however, in the form of counter-rotating vortices.

Changes in turbulent properties when the depth of the mixed region rivals the horizontal dimensions of the tank have been previously observed. A change in the dynamics of a turbulent front in a homogeneous fluid was observed for $D > W$ in the cylindrical tank experiments of Dickinson and Long (1978). As well, in the two-layer experiments of Fernando and Long (1983), the deepening rate of the turbulent region showed a marked increase after deepening past a breakpoint.

2.4 Scaling Theory

The energy dissipation rate, ϵ, in a statistically steady forced turbulent flow scales according to

$$\epsilon \sim \frac{u^3}{\ell} \tag{2.6}$$

where u is the rms fluctuating velocity and ℓ is the integral length-scale of the eddies [Tennekes and Lumley 1972].

In three-dimensional turbulence there is a transfer of energy from the integral length-scale to the Kolmogorov microscale, η. The latter is the typical length-scale at which kinetic energy is irreversibly dissipated through the ac-

tion of molecular viscosity. The value of η is related to the energy dissipation rate by

$$\eta \propto (\nu^3/\epsilon)^{1/4} \tag{2.7}$$

Assuming the grid supplies energy evenly across the horizontal area of the tank at grid level, and assuming the tank dimensions do not affect the turbulence, the relevant vertical length-scale characterizing the turbulence is δz, the distance below the energy source. In theory, δz is measured with respect to a virtual origin [Long 1978b; Thompson and Turner 1975]. In practice we find that it is sufficient to take the virtual origin at the mean vertical position of the oscillating grid. Dimensional arguments then predict that $\ell \propto \delta z$ and $\eta \propto \delta z$. Combining these results with equations (2.6) and (2.7), the velocity is found to scale with distance from grid as $u \propto \delta z^{-1}$. This scaling was also derived by Long (1978b), although using a different theoretical approach. This dependence has been documented experimentally (*e.g.* E and Hopfinger (1986)) in tanks with square horizontal cross-sectional area.

The characteristic time scale, $\tau = \ell/u$, of horizontally homogeneous 3-D turbulence is thus expected to obey the scaling law

$$\tau_{3D} \propto \delta z^2. \tag{2.8}$$

The scaling for the experiments in which $D \gg W$ cannot be derived following the same dimensional arguments as in the three-dimensional case. Eddies that extend to sufficiently large depths increase in size until the extent is comparable to the tank width, W. Below this depth the eddies are constrained laterally and are thus free to move only in an approximately two-

dimensional plane (the $x - z$ plane). Because energy cascades to larger scale in two-dimensional turbulence [Fjørtoft 1953] the eddies continue to increase in size to fill the extent of the domain in which they are contained. Thus a mean circulation develops.

However, the eddy motions at scales $\ell \ll W$ are not confined by the tank geometry and the turbulence at the small scales is still approximately isotropic in horizontal planes. This small-scale turbulence is advected and distorted by the mean circulation.

Therefore, as D is increased, there is a transition from three-dimensional unconstrained turbulence to quasi-two dimensional turbulence at large scales with embedded three-dimensional small-scale turbulence. The dynamically important length scales are then D/W as well as &z, and the time scale dependence need not necessarily follow (2.8). Indeed, Hopfinger and Toly (1976) measured a distortion of the scaling given by (2.8) in the presence of a secondary flow.

2.5 Results

In this section we measure the variation of eddy time-scales with depth from grid midplane and investigate how the structure of the turbulence changes for different values of D, which varies from 7.7 cm to 34.7 cm.

For each experiment, 27 vertical time series are taken across the tank, starting at 4 cm from the left wall, spaced 1 cm apart, to 30 cm from the left wall. The time series are collected sufficiently far from the side walls to avoid strong upward moving jets in the 2 cm wide boundary layer near the tank side walls. Time series far from the left wall of the tank are not used to measure

time-scales because of weak intensity signals resulting from light attenuation across the tank by the pearlescent dye.

In several large aspect ratio experiments, fluid upwelled near the centre of the tank. In these upwelling regions the turbulence was observed to evolve with much longer eddy time and length-scales than those in the downwelling turbulence. For consistency, time-scale analyses are performed only where the centre motion is downward.

Time-scale analyses are performed individually on each of the (at most 27) time series. The resulting profiles of time-scale versus depth are then averaged. For example, the time-scales determined from an experiment with $D = 37.4\,\mathrm{cm}$ is shown in Figure 2.6. Figure 2.6a shows three time-scale profiles calculated for the time series at 5, 10, and 15 cm from the left wall of the tank. The profiles are vertically offset for clarity. Along all three profiles the time-scale generally increases with depth, though values fluctuate greatly for large δz. The fluctuations are reduced after averaging, as evident in Fig. 2.6b, which shows the average and standard deviation of 15 time-scale profiles across the width of the tank in the same experiment. The plot shows how the fluctuations in each time-scale profile are smoothed by the averaging process.

Log-log plots of the averaged time-scale profiles of $\mathcal{T}_1(\delta z)$ and $\mathcal{T}_2(\delta z)$ are shown in Figure 2.7 for three experiments with $D = 14.6, 24.7, 34.7\,\mathrm{cm}$.

Particularly evident in the $\mathcal{T}_1$ results, but common to both time-scales, are different scaling regimes of the turbulence. Crudely, we identify three regimes: a near-grid regime, a mid-depth regime and a near-bottom regime. The first and second regimes occur approximately over the respective ranges $\delta z = 3-7\,\mathrm{cm}$ and $\delta z = 12-20\,\mathrm{cm}$ (when $D \geq 20\,\mathrm{cm}$). These are distinguished

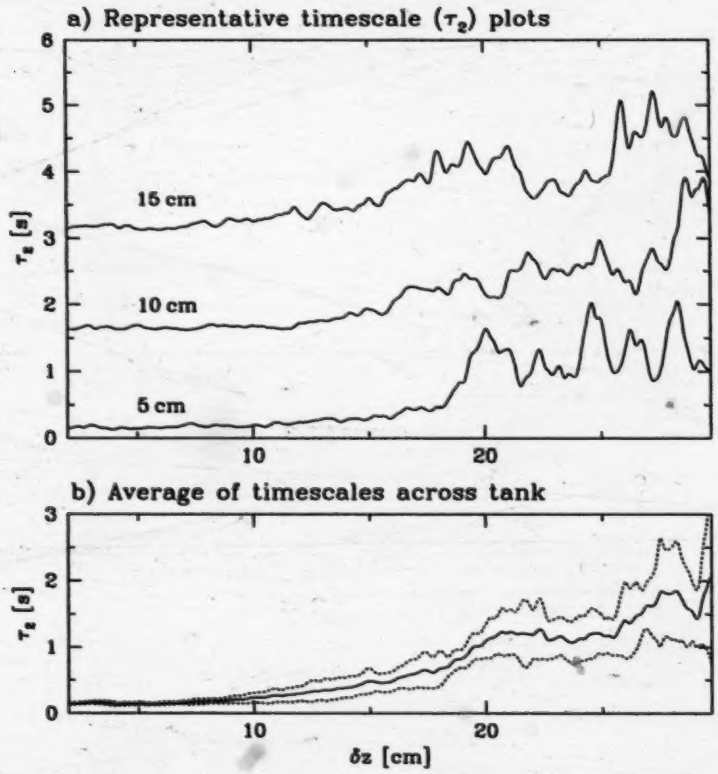

Figure 2.6: a) Three plots of eddy time-scales $\mathcal{T}_2$ as a function of distance from grid, δz, in an experiment with $D = 34.7\,\mathrm{cm}$ taken from time series at $x = 5\,\mathrm{cm}$, $10\,\mathrm{cm}$, and $15\,\mathrm{cm}$. b) Average and standard deviation (dotted line) of 15 timescale profiles taken at successive horizontal positions across the tank.

by different power law dependencies of the form

$$\mathcal{T} = (\delta z)^p. \tag{2.9}$$

The power law exponent is smaller in the near-grid regime. Indeed, the time-scale profiles characterized by $\mathcal{T}_1$ show a distinct elbow in all experiments, whereas with $\mathcal{T}_2$ the change is more gradual. In experiments with $D \gg W$, a third near-bottom regime is evident in which there is no power law dependence.

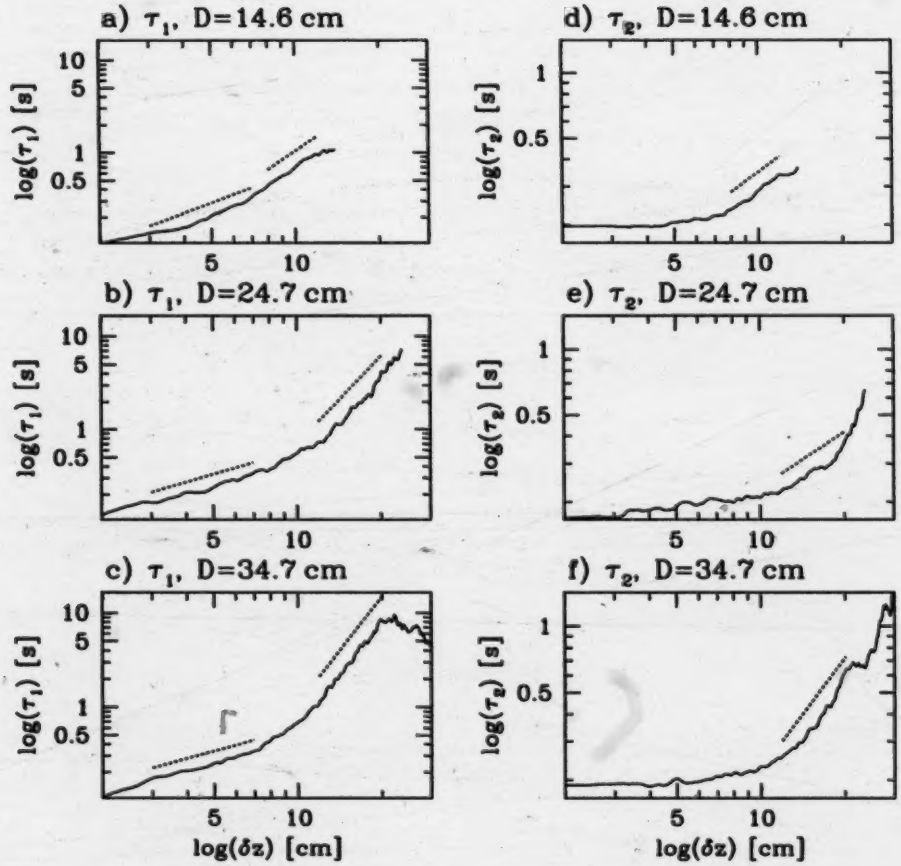

Figure 2.7: Comparison of profiles for timescales $\mathcal{T}_2$ and $\mathcal{T}_1$. Log-log plots of eddy time-scales $\mathcal{T}$ as a function of distance from grid δz for three depths of tank, D=14.6 cm, 24.7 cm, and 34.7 cm from grid midplane. The (vertically offset) best-fit lines to the plots are given for the ranges $\delta z = 8 - 12$ cm when D=14.6 cm, and $\delta z = 12 - 20$ cm when D=24.7 cm, and 34.7 cm.

We measure δz from the midplane of the grid rather than measuring δz from the virtual origin defined by Hopfinger and Toly (1976). Because the behaviour of the turbulence time-scales near the grid is different from that away from the grid, the dependence of eddy time-scale with δz cannot be meaningfully extrapolated to a virtual origin. In particular, the time-scales characterized

by $\mathcal{T}_2$ are approximately constant functions of δx near the grid and so cannot be extended to $\mathcal{T}_2 = 0$ to determine the virtual origin. Following Hopfinger and Toly (1976), the location of the virtual origin for our experimental configuration would be 1 cm $\pm$ 0.5 cm below the midplane of the grid. Varying the location of the virtual origin by $\pm$ 2 cm from the midplane of the grid resulted in a maximum of a 13 percent difference in the value of the exponent for the power law.

The $\mathcal{T}_1$ power law exponents, p, measured for $3 \leq \delta x \leq 7$ cm $(= 1 - 2S)$ in a series of experiments with different depths, D, are denoted by diamonds in Figure 2.8. The exponents are approximately constant over all values of D, with a value $p \approx 0.79 \pm 0.17$. This suggests that the structure of the turbulence in this range is affected exclusively by the jets from the mixer and not by the tank geometry, as evident in Fig. 2.4a. It has been extensively reported [Thompson and Turner 1975; Hopfinger and Toly 1976; Fernando and Long 1983; Atkinson, Damiani and Harleman 1987] that the individual wake and jet structure persists within 2 stroke lengths of the grid.

At fast time scales, *i.e.* very close to the grid, $\mathcal{T}_1$ is sensitive to the resolution of the time series data. In order to test for the degree of sensitivity we performed the analysis on the same data but at half the resolution. The results were qualitatively the same but with consistently lower values of power law in the near-grid regime and no change in the mid-depth values.

The power law exponents measured for $12 \leq \delta x \leq 20$ cm are denoted by the solid circles in Figure 2.8 for both $\mathcal{T}_1$ and $\mathcal{T}_2$. In experiments with $D < 20$ cm, the power law is instead computed over the range $\delta x = 8 - 12$ cm. These results are denoted by the open circles in Fig. 2.8. The two data points at $D = 22.3$ cm correspond to two different experiments at that depth of tank.

In the experiment with $D = 20\,\text{cm}$ a large exponent is measured because the plot of $\mathcal{T}_1(\delta z)$ does not show a sharp distinction between near-grid and mid-grid regimes. The best-fit line in the common range of $\delta z = 12 - 20\,\text{cm}$ used to establish the power law was taken at the curve in the plot similar to the elbows seen in Fig. 2.7.

When the ratio of D to W is approximately $1:1$ the counter-rotating cells of the mean circulation are not observed, and the turbulence is expected to act as if it is fully three-dimensional. In experiments with progressively larger D, a large-scale circulation is more pronounced and the measured values of p are larger. Whether characterized by $\mathcal{T}_1$ or $\mathcal{T}_2$, generally we find that the power law exponent at mid-depth in the tank increases with increasing D.

These plots clearly demonstrate how the turbulent scaling at mid-depth is distorted by the presence of a bottom boundary, even though the boundary is many eddy length-scales below the scaling region. The turbulence is affected by the large-scale circulation that develops and deviations from horizontally homogeneous turbulence theory become more pronounced in experiments with $D \gg W$.

The dynamics of the large-scale circulation is illustrated in Figure 2.9 which shows the results of the cross-correlation analysis performed on an experiment with $D = 42\,\text{cm}$. Whereas the time series in Figs. 2.4 and 2.5 qualitatively show the existence of the circulation, the cross-correlation effectively determines the slopes of the streaks in these images and so measures the velocities.

Typical velocities for the vertical motions are $2.0\,\text{cm/s}$ for the overall downwelling motion and $1.5\,\text{cm/s}$ for the return flow near the sides. These measured velocities are consistent with estimates of the velocities based on observations. The velocities are calculated at nine points using a Gaussian weighted average

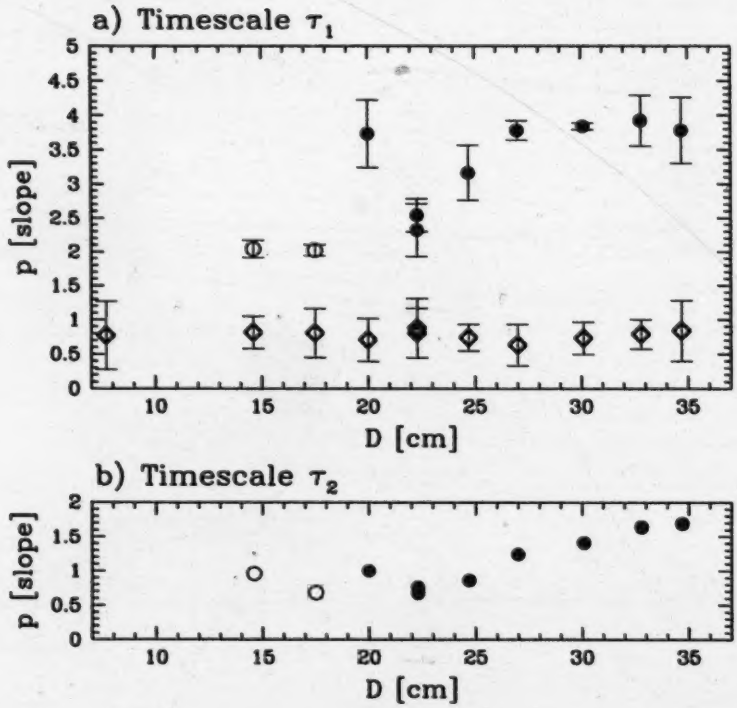

Figure 2.8: Power law dependence of timescale with distance from grid for experiments with varying depth of tank, D. The different symbols represent different ranges of data used to calculate the slopes of the best-fit lines to the logarithmic plots of Figure 2.7. Solid circles: $\delta z = 12 - 20\,\mathrm{cm}$; open circles: $\delta z = 8 - 12\,\mathrm{cm}$ (the total depth of tank is less than 20 cm); diamonds: $\delta z = 3 - 7\,\mathrm{cm}$. The error bars give the standard deviation of the best-fit lines. In b) the error bars are within the size of the circles.

of 506 velocities determined directly from the cross-correlation analyses. The accuracies in the final velocity measurement are determined from the standard deviation of the averaging process. The accuracy of the measured velocities ranges from 0.3 cm/s to 1.2 cm/s, depending on the intensity and duration of the streaks in the original time series. The vertical velocities with accuracies close to 0.3 cm/s are those at the centre and sides of the tank. These are the regions where the vertical motion in the circulation is strongest and the

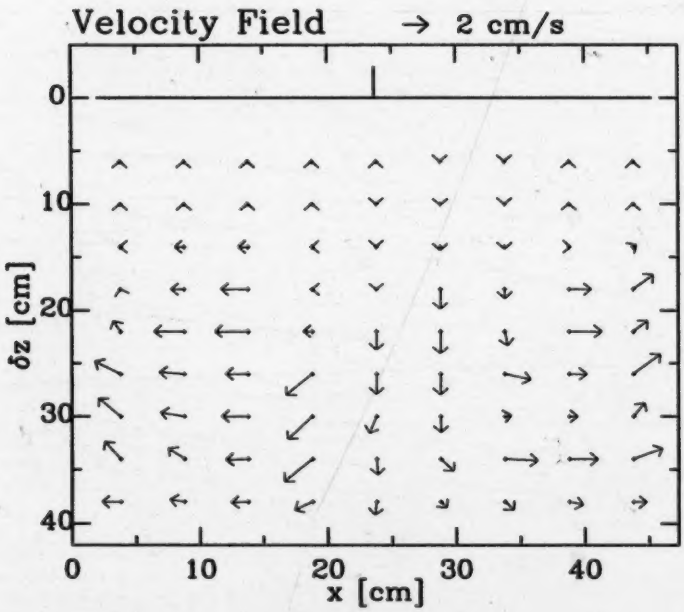

Figure 2.9: The velocity field from cross-correlation analysis for the same experiment as in Figures 2.4 and 2.5, in which counter-rotating cells are prominent. The depth of tank is $D = 42\,\text{cm}$. The velocity scale is illustrated by the arrow above the plot.

cross-correlation signal is unambiguous.

Similarly, the magnitude of the horizontal velocities is typically 2.0 cm/s measured with an accuracy between 0.5 cm/s and 1.2 cm/s. The accuracy is poor at the centre and sides of the tank where the horizontal component of the velocity field is close to zero.

The cross-correlation analysis measures velocities of a strong mean circulation, such as that which occurs in the experiment with $D = 42\,\text{cm}$. In experiments with small D there is no significant mean circulation and such an analysis cannot be done.

2.6 Discussion

Pearlescent dye is a useful tool for visualizing the qualitative features in a turbulent flow and for taking quantitative measurements. The dye can highlight individual eddy motions as seen, for example, by the increase in time-scale from top to bottom of Fig. 2.3a. It can also highlight mean flows in the turbulence. For example, Figs. 2.4 and 2.5 clearly show two tank-scale counter-rotating vortices. Pearlescence also marks the boundary of a turbulent region, as in the deepening of the mixed region shown in Fig. 2.2.

We have developed a non-intrusive technique that uses pearlescent dye to measure the variation in time-scale with distance from the energy source in oscillating grid turbulence over the entire flow field. This technique can be used to measure the local vertical and horizontal velocities of a mean flow in the turbulence.

The change in eddy time-scales with distance from an oscillating grid exhibits different regimes. The time-scale $\mathcal{T}_1$, which best measures piecewise continuous functions, shows distinct near-grid and mid-depth power law scaling regimes. In the regime closest to the mixer, the time-scales exhibit a power law dependence in which the exponent depends exclusively on the distance from the oscillating grid. In the intermediate-depth regime the slopes of the log-log plots increase with increasing depth of the tank. The time-scale $\mathcal{T}_2$ is less sensitive to the temporal resolution, but a power law scaling is not as obvious. Nonetheless, using either of our definitions of eddy time-scale we see the same increasing trend in the time-scale power law with an increase in D. Thus, we have found that the location of the bottom boundary affects the turbulence scaling behaviour over a distance much longer than the characteristic

length-scale of the eddies near the base of the mixing region.

We attribute the change in scaling behaviour to the observed development of a mean circulation which occurs if $D \gg W$. The circulation develops as a result of a transition from fully three-dimensional turbulence in the case where $D \leq W$ to quasi-two-dimensional turbulence in which there is an up-scale cascade of energy for eddies with length-scales larger than W. Embedded within this large-scale turbulence is the small-scale three-dimensional turbulence. The measured time-scales record the variability of eddies much smaller than the mean circulation. The observed increase in power law exponent with an increase in D is thus due to the transition from undistorted eddies to eddies distorted by the mean circulation. Comparison of scaling exponents for experiments with $D \leq W$ with the theoretical scaling in equation (2.8) suggest that $\mathcal{T}_1$ is the more appropriate time-scale to use for measuring three-dimensional turbulence in our experiments.

Although the experiments described in this chapter involve homogeneous fluid with a rigid bottom boundary, experiments reported upon in the next chapter that investige a turbulent mixed layer overlying a stratified fluid have shown that similar dynamics occur when the rigid boundary is replaced with a stratified layer.

These experimental results may indirectly prove useful in interpreting turbulence measurements in the surface mixed region of the ocean. It is common practice to assume the classic "law-of-the-wall" for turbulence scaling in the oceanic boundary layer [Kantha and Clayson 2000]. This assumes that scaling is a function only of distance from the surface. Our results show that scaling may also be affected by the depth of the thermocline underneath the oceanic boundary layer in the presence of a mean circulation, such as Langmuir circula-

tions. These wind-induced circulations have the form of counter-rotating cells similar to the counter-rotating vortices observed in our experiments with large D. Though generated by a different mechanism, and despite the presence of a mean horizontal surface flow, our results suggest that the mean circulations distort the scalings in the turbulence.

Chapter 3

Laboratory Experiments with Internal Waves

3.1 Introduction

In this chapter we use new laboratory measurement techniques to analyze the properties of internal waves that are generated below an approximately homogeneous layer of turbulence that overlies a stratified fluid. We examine a series of mixing box experiments in which the frequency and amplitude of the grid oscillations are fixed. Only the strength of the stratification is varied.

As well as the use of pearlescence to visualize the turbulent mixed region, as described in Chapter 2, in this investigation we use two techniques, both non-intrusive, to visualize the internal wave field. The first set of experiments involves the use of dye-lines to track the movement of isopycnal layers. The second set of experiments employs a new technique called "synthetic schlieren" [Sutherland et al. 1999; Dalziel, Hughes and Sutherland 2000] that visualizes and measures amplitudes of individual wave packets. This method has not

been used previously to measure internal waves generated from turbulence. An advantage of this technique is the ability to record information on the entire wave field for the duration of the experiment. This technique has allowed us to perform the first laboratory investigation into the properties of internal waves generated from a turbulent layer.

The majority of previous mixing box experiments have been performed in tanks with a square horizontal cross-section. To facilitate the use of the synthetic schlieren technique we report on experiments performed in a tank with a large (5:1) aspect ratio. As a consequence of this geometry, we find that mean circulations develop in the mixing region that excite relatively large amplitude internal wave modes on the scale of the tank.

3.2 Experimental Set-Up and Analysis Technique

3.2.1 Apparatus

Experiments are performed in an acrylic tank of horizontal dimensions $W = 9.7\,\text{cm}$, $L = 47.6\,\text{cm}$ and of height $H = 49\,\text{cm}$, as shown in Figure 3.1a. This geometry allows us to record wave motions that are quasi-two-dimensional (in the $x - z$ plane). The two-dimensional nature has been verified with experiments using slit lighting to illuminate the interior of the tank over only a small fraction of the width.

The tank is initially filled up to 2 cm from the top of the tank with uniformly salt-stratified water using the standard "double-bucket" technique [Oster 1965] and a sponge float. The strength of the stratification may be represented by

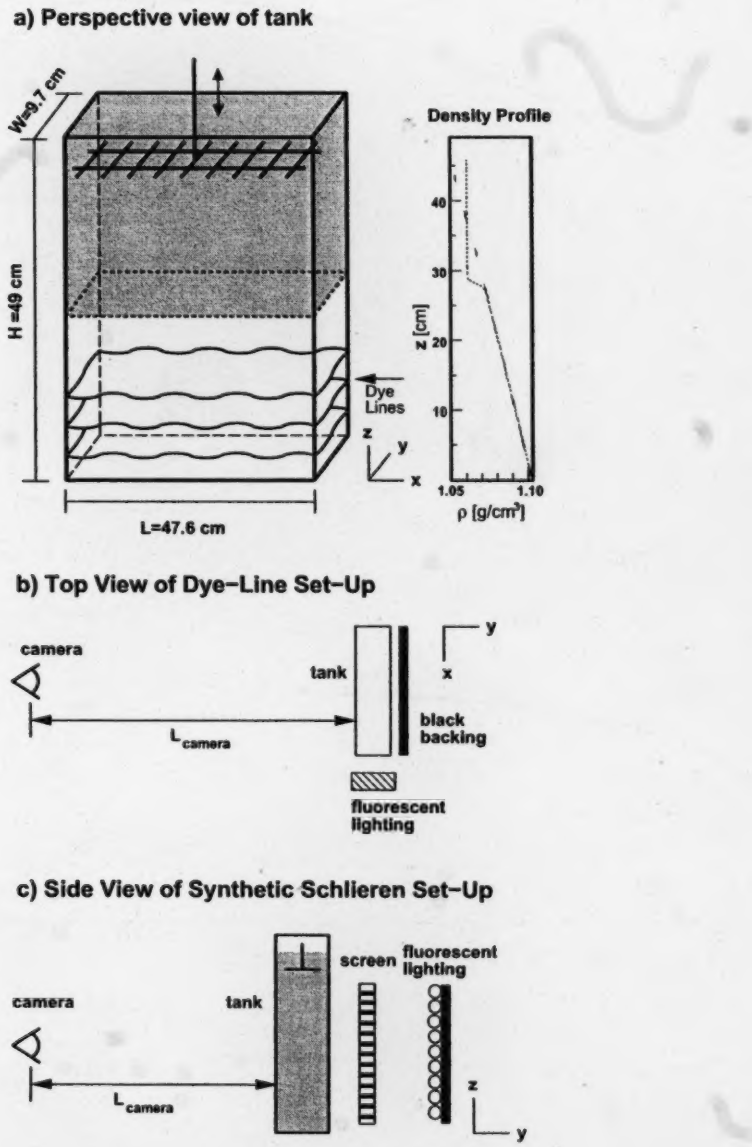

Figure 3.1: The experimental configuration for the two methods. In a) are the tank dimensions. The tank is filled with uniformly salt-stratified fluid and a turbulent mixed layer is created at the top (shaded region) of the tank by the oscillating grid. A sample density profile before and after an experiment is included. The dye-line experimental configuration in shown in b) and the synthetic schlieren configuration in c).

the (constant) buoyancy frequency, N, which in the BOussinesq approximation is defined by

$$N^2 = -\frac{g}{\rho_0}\frac{d\overline{\rho}}{dz} \tag{3.1}$$

where $\overline{\rho}(z)$ is the background density profile, ρ_0 is a reference density ($\approx 1.0\,\mathrm{g/cm^3}$) and g is the gravitational acceleration. The initially constant buoyancy frequency ranges between $0.33\,\mathrm{s^{-1}}$ and $1.40\,\mathrm{s^{-1}}$. A stainless steel mixer is inserted 7 cm from the top of the tank, and 5 cm below the free surface of the water. The mixer is a ladder-shaped square grid of hollow cylindrical bars of diameter 0.6 cm spaced 3.2 cm apart. Rungs extend beyond the struts of the ladder, as described in section 2.2.1, in order to minimize the development of a secondary flow along the tank walls [E and Hopfinger 1986; Fernando and DeSilva 1993]. When switched on, the mixer moves vertically with a frequency of 7 Hz and with a peak-to-peak stroke length of 2.6 cm.

A digital camera is positioned a distance $L_{\mathrm{camera}} \approx 4\,\mathrm{m}$ from the tank. The recorded images in the $x-z$ plane are analyzed using the image processing software package, DigImage [Dalziel 1993] and are described further in the subsections below.

A conductivity probe traverses downward through the tank, measuring the density profile before and after an experiment. Fig. 3.1a shows the typical results. The dotted line, the density profile after the experiment is complete, shows the extent of the interface between the mixed region and the stratified region.

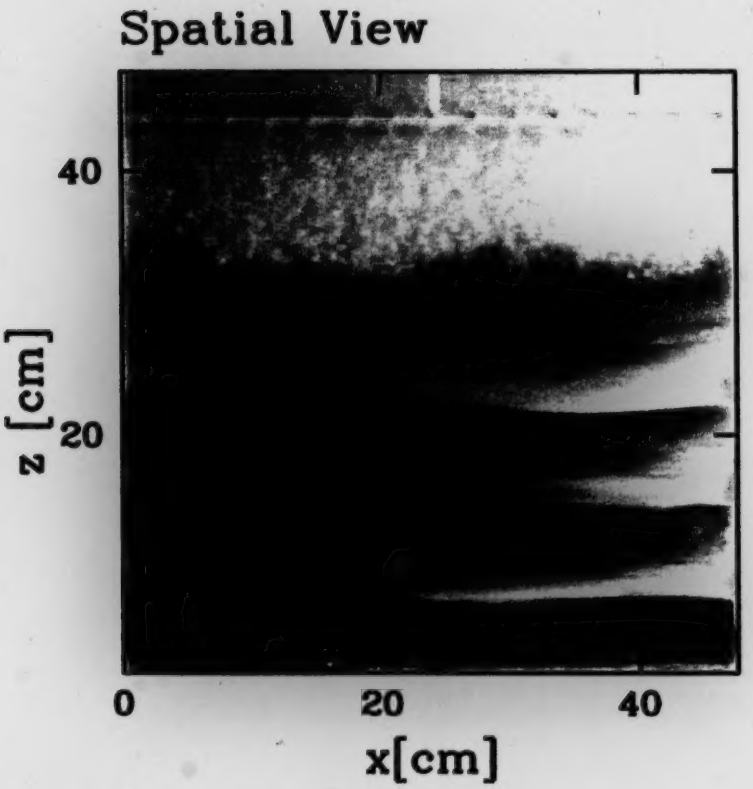

Figure 3.2: View through the front (long side) of a laboratory experiment. Three dye lines mark the vertical motions of isopycnal layers and are illuminated from the right. The turbulent region extends from $z = 47\,\text{cm}$ to $z \approx 27\,\text{cm}$.

3.2.2 Dye-Line Technique

In the first set of experiments, Rhodamine dye is added to the sponge float three times during filling in order to mark three isopycnal layers. This dye is illuminated throughout the interior of the tank by a bank of fluorescent lights on the right side of the tank. A sheet of black paper is fastened to the back of the tank. The plan view of the configuration is shown in Fig. 3.1b. A pearlescent dye (Mearlmaid Natural Pearl Essence) is distributed across the top of the tank prior to the start of the experiment in order to highlight the

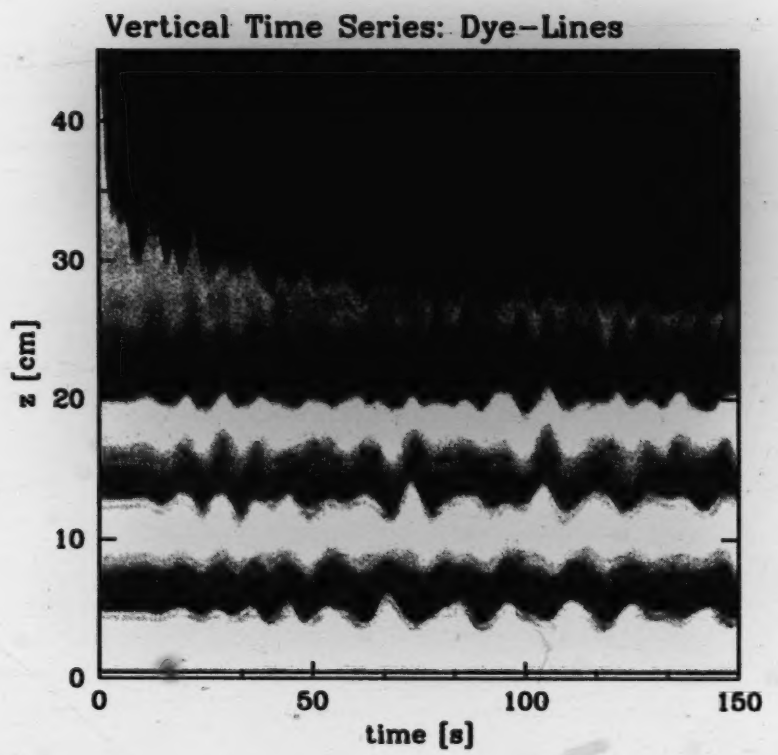

Figure 3.3: a) A sample false-colour vertical time series image for an experiment with $N = 0.79\,\mathrm{s}^{-1}$. The horizontal location of the time series is at $x = 29.9\,\mathrm{cm}$ from the left side of the tank. The bottom of the turbulent region is approximately at $z = 28\,\mathrm{cm}$. The vertical motions are tracked by the three dye-lines (dark bands) at isopycnal layers with mean vertical positions 5.4, 12.7 and 20.5 cm above the bottom of the tank.

turbulent motions, as in the previous experiments of Chapter 2.

A view through the front of the tank in a dye-line experiment for which $N = 0.79\ \mathrm{s}^{-1}$ is shown in Figure 3.2 at time $t = 2.4T_{buoy}$, where $T_{buoy} = 2\pi/N$ is the buoyancy period. The turbulent region at the top is highlighted by the pearlescent dye and the oscillating grid can be seen near the top of the turbulent region. The three isopycnal layers marked by the fluorescent dye can be seen in the lower part of this image.

The time evolution throughout an experiment of the vertical position of the three dye-lines can clearly be seen in a vertical time series, shown in Figure 3.3 for the first 150 s of an experiment in which $N = 0.79\,\mathrm{s}^{-1}$. Also evident from the lower extremity of the top dark region in this image is the position of the base of the mixing region. The time series is constructed from the digitized images of the experiment by storing the pixel column at $x = 29.9$ cm (29.9 cm from the left side of the tank) at successive time steps in a single image. The temporal resolution is limited by the standard NTSC video frame rate and can be as small as 1/30 th second. The resolution of the image shown in Fig. 3.3 is 0.3 s. In all our experiments 23 vertical time series are taken simultaneously at 23 evenly spaced horizontal positions between $x = 1.4$ and $x = 46.2$ cm.

The image in Fig. 3.3 has been enhanced with a false-colour grey scale. The intensities of the Rhodamine-dye-lines are related to the dye-layering process and are not significant for our investigation. There is negligible diffusion of the dye-lines for the duration of the experiment. The bottom of the mixed layer is marked by the vertical extent of the pearlescent-dyed region. This dye, which is initially in a layer at the level of the mixer, is quickly distributed throughout the mixed region in the initial deepening process (the first 10 s) and subsequently marks the base of the region (to within 0.5 cm).

By matching contours to the dye-lines in such time series, the amplitudes and frequencies in the wave field can be measured.

3.2.3 Synthetic Schlieren Technique

The technique of synthetic schlieren [Sutherland et al. 1999] is the second method used to visualize the internal wave field. This method exploits how the index of refraction varies with salinity to measure very small wave amplitudes. Under ideal conditions, in our experiments displacements as small as .001 cm can be detected.

The experimental configuration is shown in Figure 3.1c. A 45×45 cm translucent screen of horizontal black and white lines is placed $L_s = 51.2$ cm behind the long side of the tank. The lines are .25 cm thick and spaced .25 cm apart. A bank of fluorescent lights is placed 25 cm behind the screen and illuminates the screen through the tank. A digital camera is positioned a distance $L_{\text{camera}} = 420$ cm in front of the long side of the tank. The field of view is set to include the entire image of the screen as seen through the tank. In synthetic schlieren, no dye-lines are introduced.

The synthetic schlieren technique is based on the degree of deflection of light as it travels through a stratified medium. The stronger the stratification, the greater the deflection. As they pass through a continuously stratified fluid, internal waves stretch and compress isopycnal surfaces thereby locally adjusting the stratification. Thus the image of the translucent screen becomes distorted as viewed through the tank by the digital camera. By measuring the distortion of the image, that is, by determining the apparent local vertical displacement, Δz, of the horizontal lines in the image, synthetic schlieren indi-

rectly measures the amplitudes of the internal wave field. Explicitly, assuming the waves are uniform amplitude across the width of the tank, the changes in the density gradient are related to Δz according to

$$\Delta N^2 \simeq -\alpha \Delta z. \tag{3.2}$$

Here ΔN^2 is the change in the squared buoyancy frequency due to changes of the vertical density gradient induced by internal waves. In our experiments, the proportionality constant $\alpha = 7.4\,\mathrm{s}^{-2}\,\mathrm{cm}^{-1}$ is based on the tank width, the distance L_s, the relative position of the bottom of the tank with respect to the camera, and physical constants such as gravity and the indices of refraction of air, water and salt water. (For more details on the determination of this constant see Sutherland *et al.* (1999), eq.(2.11).)

As well as measuring the apparent displacement, Δz, of a point on the image from its original position, it is often useful to measure the displacement of a point after a small time step Δt. In this way the time derivative of the ΔN^2 field, N_t^2, is measured:

$$N_t^2 \simeq -\alpha \Delta z / \Delta t \tag{3.3}$$

where Δz is now the relative displacement of a point on the image between successive times.

The formulae (3.2) and (3.3) are exact only for two-dimensional internal waves having constant amplitude across the width of the tank. In our experiments, we find the horizontal scale (in the x-direction) of the internal waves generated by turbulent jets to be on the order of 10 cm, comparable

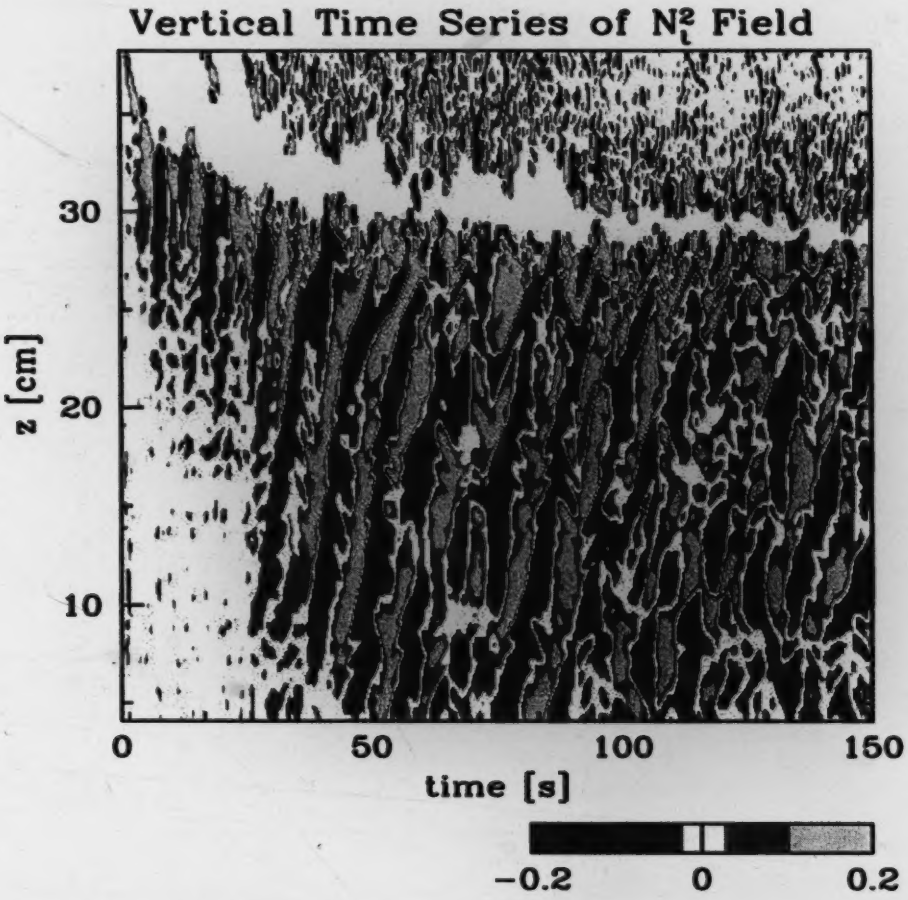

Figure 3.4: A sample vertical time series of an N_t^2 field for an experiment with $N = 1.06$. The horizontal location of the time series is at $x = 36.9\,\mathrm{cm}$ from the left side of tank. The bottom of the turbulent region is approximately at $z = 27\,\mathrm{cm}$. The colour scaling is provided. The amplitudes of the field lie in the range $-0.2 < N_t^2 < 0.2\,\mathrm{s}^{-3}$.

to the width of the tank. Hence we anticipate that the waves are quasi-two-dimensional and that the amplitudes we measure reasonably represent the spanwise average.

From the ΔN^2 field, one can use linear theory to estimate the vertical and horizontal velocity fields. Likewise, the vertical displacement field, ξ, can

be determined from the N_t^2 field. Because the latter field can be determined consistently even for large amplitude perturbations, typically the N_t^2 field is computed. We set $\Delta t = 0.3\,\mathrm{s}$, much smaller than the buoyancy period but large enough to give a substantial signal from the wave field.

Vertical time series are used to examine the temporal as well as spatial behaviour of the wave field. An example of a time series of the N_t^2 field is shown in Figure 3.4. The image is enhanced with a false colour representation. The temporal resolution is 0.3 s and the duration of the time series is 150 s. Because synthetic schlieren is sensitive enough to detect slight thermal variations the image is further enhanced with band-pass filtering to remove high and low frequency thermal variations and high frequency electronic noise. The base of the turbulent region is traced by the descending white region near the top of the image which extends to approximately 27 cm. The frequencies, ω, and vertical wavenumbers, k_z, of the internal waves below the mixing region can be measured directly from these images with the use of Fourier transforms.

3.3 Qualitative Observations

At the start of an experiment, the turbulent region deepens rapidly within approximately the first 10 seconds. Depending upon the strength of the stratification, it continues to deepen approximately another 5 cm over the next two to three minutes. The experiments with homogeneous fluid have shown that the mixed region will extend to the entire depth of the tank after approximately 40 s. Thus, the dynamics of the first 150 seconds capture the process of both the initial establishment of a mixed layer as well as the nearly statistically steady state. In all experiments two counter-rotating vortices are

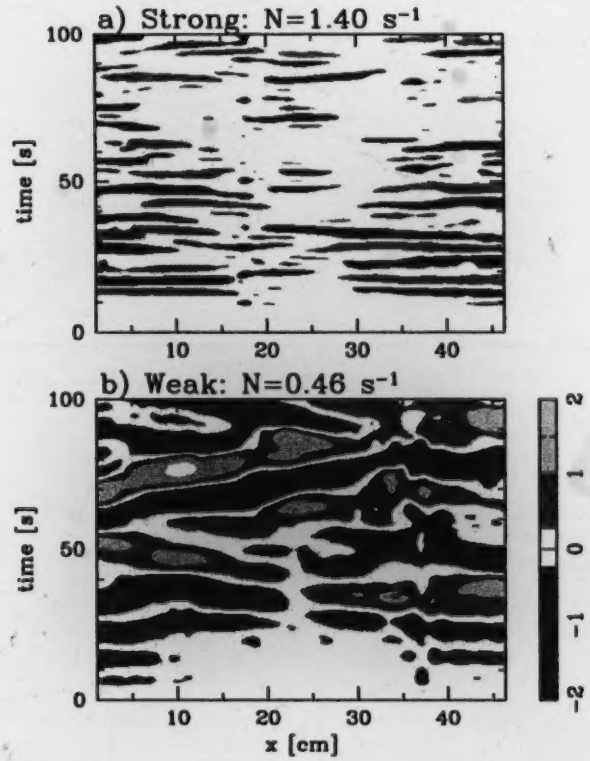

Figure 3.5: Horizontal time series of the vertical displacement from start position of the middle dye-line for a) a strongly stratified experiment, $N = 1.40\,\mathrm{s}^{-1}$ and b) a weakly stratified experiment, $N = 0.46\,\mathrm{s}^{-1}$. The colour scale for both time series is provided at the side panel and is given in units of centimetres.

established within the turbulent region. The vortices are oriented with rotation vectors out of the front of the tank (along the y-axis in Fig. 3.1) with upwelling at the sides, and downwelling in the centre of the tank, as described in the previous chapter. Embedded within these vortices are fast time-scale and small length-scale eddies. The base of the region appears to be deformed by $5 - 10\,\mathrm{cm}$ wide turbulent jets that push vertically down into the stratified region at random positions along the length of the tank.

Large tank-scale waves are generated below the mixing region within sec-

onds of the start of the experiment. The waves resemble "mode 1" or "mode 2" (in the horizontal) standing waves in the tank, with mode 2 most frequently observed. Both modes are quasi-two-dimensional, exhibiting negligible variation across the width of the tank. These tank-scale waves can be seen in the snapshot of an experiment in Fig. 3.2 which shows these tank-scale internal waves by the vertical displacement of dye lines. In the snapshot the dye-lines are displaced upwards at the sides and middle of the tank.

Fig. 3.3 shows typical tank-scale internal wave dynamics. The dye-line contours are synchronized for the first 40 seconds of the time series; such motion is characteristic of internal wave modes. After 40 seconds transient wave packets destroy this regularity. These wave packets travel down through the three Rhodamine-dyed isopycnal layers, a feature which is seen in many experiments. The transient wave packets have horizontal wavelengths on the order of one quarter of the tank length and seem to be generated from the smaller-scale turbulent jets described above.

The particular modal structure to the wave field can be seen in Figure 3.5, which plots the vertical displacement of a dye-line over 100 s for both a strongly stratified and a weakly stratified experiment. In both cases initially the overall structure to the wave field is mode 1 ($\lambda_x = 2L$ with a node in the centre of the tank). For the strongly stratified experiment (Fig. 3.5a), after approximately one minute the modal structure switches to mode 2 (with horizontal wavelength $\lambda_x = L$ and nodes at $x = \frac{L}{4}, \frac{3L}{4}$). Travelling waves are observed in both experiments (for example, beginning at $t = 50$ s in Fig. 3.5b, but the overall standing wave structure can be seen throughout the duration of the time series.

The standing waves are on the scale of the counter-rotating vortices in the

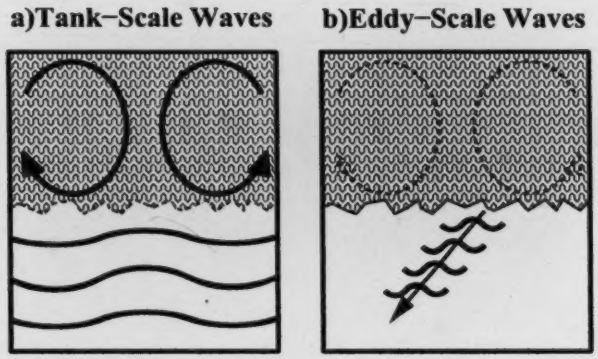

Figure 3.6: Schematic views through the long side of the tank depicting the two scales of internal waves. a) A mean circulation in the mixed region excited tank-scale internal waves. Dye lines marking isopycnal layers highlighted these large-scale motions. b) Smaller-scale downward-propagating internal waves were generated on the scale of the smaller eddies and jets in the turbulence.

turbulence. The vortices, although a permanent feature in the turbulence, are not perfectly stationary and irregularly force the fluid beneath on the scale of the tank. The standing waves persist for the duration of the experiments with amplitudes that are maintained throughout the experiment and damp down on a time-scale on the order of 20 buoyancy periods after stopping the mixer. This shows that these waves do not develop only as a consequence of transient start-up dynamics. Rather, they are continuously invigorated by the action of the counter-rotating vortices pushing down on the bottom of the mixed region.

The vortices filled the mixed region and had the form shown in the schematic Figure 3.6a, with flow up the short sides of the tank. These vortices continuously excited waves on the scale of the tank. Along with the tank-scale waves, smaller-scale downward-propagating waves were also continuously generated from the eddies and jets in the turbulence, as depicted in Fig. 3.6b. Analysis of the latter waves is discussed in §3.4.2.

3.4 Quantitative Results

3.4.1 Tank-Scale Internal Waves

To plot displacement as a function of time at three vertical levels, we fit a contour to the bottom flank of the time series image of each dye-line. Each contour is decomposed in a Fourier series and from this the average amplitude of the vertical displacement is determined as a function of frequency. The results determined from a moderately stratified experiment are shown in Fig. 3.7 which plots the amplitudes of the three dye-line contours in Fig. 3.3 along with the amplitude of the base of the mixing region. The amplitudes are calculated from the full 150 s of the time series. The first set of plots, Fig. 3.7a-d are calculated from a single time series, taken at $x = 29.9$ cm, a location chosen to avoid the locations of the nodes of the first two horizontal modes of the tank (the dominant tank-scale motions in all experiments). The vertical displacement spectrum is spread throughout the range of allowable wave frequencies $\omega < N$.

The base of the mixing region (Fig. 3.7a) exhibits a broad band of frequencies including those well above the buoyancy frequency. No distinct peaks appear except for $\omega \approx 0$. Because the location of the mean position of the base of the turbulent region changes gradually with time and the mean position of the dye line contours is arbitrary, the mean value, corresponding to $\omega = 0$, has been removed in all plots.

The turbulent motions excite both propagating ($\omega \leq N$) and evanescent ($\omega > N$) waves. In Fig. 3.7b-d amplitudes are peaked at distinct frequencies and there is relatively little energy in motions with frequencies greater than N. The vertical dotted line indicates the value of the buoyancy frequency for

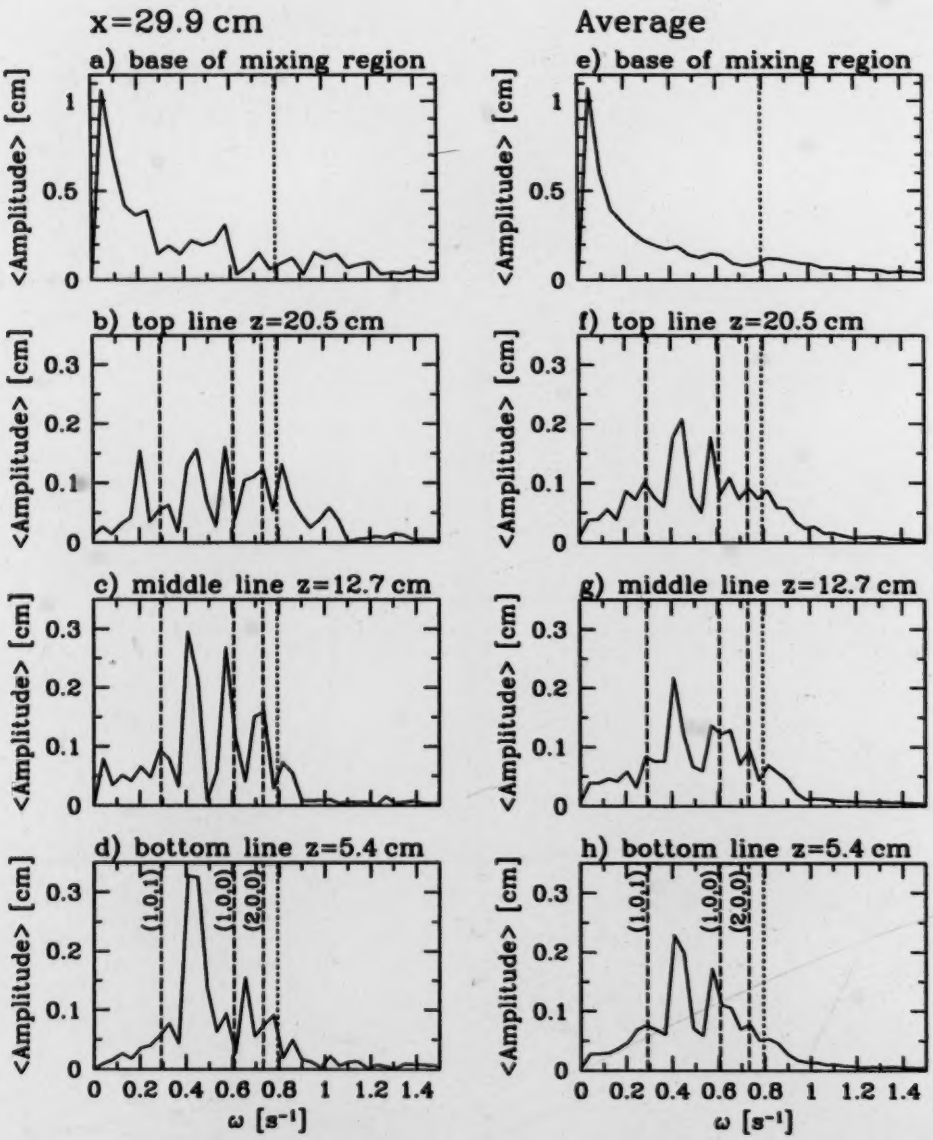

Figure 3.7: Average amplitudes of contours of the dye-lines from the vertical time series in Fig. 3.3 as calculated from the Fourier series components. The amplitudes are given for a) the base of the mixing region, b) the top, c) the middle, and d) the bottom dye-line. The plots on the left (a-d) are the amplitudes calculated from the single time series of Fig. 3.3 taken at the horizontal position $x = 29.9\,\text{cm}$. The plots on the right (e-h) are the average amplitudes for 23 time series taken across the tank. The dotted vertical line denotes the value of N and the dashed vertical lines denote the value of ω corresponding to the first three modes of the tank, as indicated in d) and h).

this experiment, $N = 0.79\,\mathrm{s}^{-1}$. The equations for the modes of the tank are described in Appendix B. The vertical dashed lines in Fig. 3.7b-d indicate the predicted frequencies of the lowest modes of the tank with wavenumbers given by (B.3) using $(n, m, p) = (1, 0, 0)$, $(2, 0, 0)$, and $(1, 0, 1)$, and depth $H = 27\,\mathrm{cm}$.

The second set of plots, Fig. 3.7e-h show the average of the amplitude measurements for the 23 time series across the tank. These plots are typical of all the experiments. The spectrum, though broad, has dominant peaks and decays for $\omega > N$ and for ω close to zero. The frequencies of the first three standing wave modes, indicated by the dotted lines, are not coincident with the dominant observed frequencies. The peaks are likely associated with a superposition of modes with comparable amplitudes or with modes having a more complex vertical structure.

Because the spectrum is spread over a range of frequencies an alternate description of the amplitude of the internal waves is used. Root-mean-square amplitude measurements of the contour lines in each of the 23 time series across the tank are calculated for times $t = 20 - 150\,\mathrm{s}$. This eliminates the time lag in establishing the waves. The modal structure is reconstructed by measuring the variation of the rms amplitude as a function of the horizontal position from which the time series is extracted for each dye-line. For example, the rms amplitude has a minimum at the centre of the tank and two maxima at the sides of the tank for experiments with dominant mode 1 standing waves. The approximate amplitude of the wave motion itself is found by multiplying the rms amplitude by $2^{1/2}$. For perfectly sinusoidal waves of the form $A\sin(\omega t)$, the procedure of finding the rms amplitude and multiplying by $2^{1/2}$ gives the amplitude A.

Fig. 3.8a plots the measured maximum amplitude of the middle dye-line

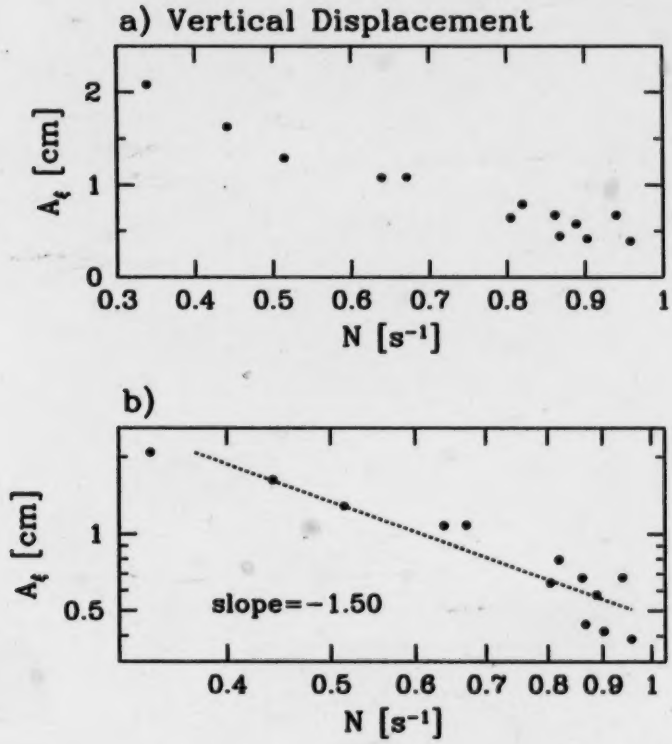

Figure 3.8: a) The variation in amplitude, A_ξ, of vertical isopycnal fluctuations, ξ, with buoyancy frequency across all experiments, and b) log-log plot of this data. The best-fit line to the logarithmic data is included, and has a slope of -1.50 ± 0.08.

plotted against the buoyancy frequency for a range of experiments. In general, we find a decreasing trend in the amplitude with increasing buoyancy frequency. Fig. 3.8b plots the same results on a logarithmic scale. The slope of the best-fit line has a value of -1.50 ± 0.08. The same analysis is performed on the top and bottom dye-lines, using either the average amplitude across the 23 time series or the maximum amplitude, and starting from $t = 0$ or $t = 20\,\mathrm{s}$. In all cases the slope of the best-fit line ranges between -1.29 and -1.54 with an average value of -1.5 ± 0.2. If only the maximum value is used, the slopes

lie between -1.45 and -1.54, for all dye-lines and for both temporal ranges. This suggests a power law relation of the form

$$A_\xi \sim N^{-1.5} \tag{3.4}$$

where A_ξ denotes amplitude of the vertical displacement of isopycnal lines.

3.4.2 Synthetic Schlieren Results

In contrast to the dye-line observations, the standing waves are not the dominant feature captured by the synthetic schlieren images. This is because synthetic schlieren is sensitive to small-scale variations. For example, the synthetic schlieren image in Fig. 3.4 is dominated by turbulent jet-scale downward-propagating waves. The modal large-amplitude waves are seen as the superimposed regular chevron structures in the N_t^2 field throughout the background of the image. It is the transient wave packet bursts that have the strongest signal. The ability to resolve the transient waves from the tank-scale modes is another advantage to the synthetic schlieren technique. The N_t^2 field captures the signal due to downward-propagating waves generated from the base of the turbulent region: the corresponding phase lines move upward in time.

Fourier transforms are used to determine the vertical wavenumbers and frequencies of the internal waves. The power spectra results of the N_t^2 field in Fig. 3.4 are determined from the squared discrete Fourier coefficients and are given in Figure 3.9a. The transform is computed from a window of the field ranging between $t = 0 - 150\,\mathrm{s}$ and $z = 17 - 27\,\mathrm{cm}$. This range is chosen to maximize the temporal range while limiting the vertical range to below the base of the mixing region. We find that the amplitudes of the wave packets

decrease as they travel downward away from the mixing region and the signals from the standing waves rival the signals from the transient wavepackets near the bottom of the tank. Attenuation of the signal from the downward propagating wavepackets is likely due to both viscous and dispersive effects since time-scale calculations of both effects reveal values on the same order as those for wave propagation. The dispersion time-scale is based on the dispersion of a wave beam in oscillating cylinder experiments under similar conditions. In order to measure the properties of the transient downward propagating waves, the bottom of the stratified region is therefore excluded from the Fourier series.

The most notable feature of the spectrum in Fig. 3.9 is that the frequencies and wavenumbers are localized around $\omega = 0.58 \pm 0.02\,\mathrm{s}^{-1}$ and $k_z = -0.7 \pm 0.3\,\mathrm{cm}^{-1}$. To characterize the overall frequencies in the field, rather than simply taking the maximum value of the peak, the power spectra are averaged over all vertical wavenumbers. The result is given as the dashed line in Fig. 3.9b. The plot illuminates the broad spectral nature of the N_t^2 field, but clearly shows a drop-off of frequency above the buoyancy frequency, indicated by the vertical dotted line, and a peak around $\omega = 0.59\,\mathrm{s}^{-1}$. To determine the approximate peak of the frequency spectrum, the averaged data is smoothed by a Gaussian running average with a bin size of $0.1\,\mathrm{s}^{-1}$. The results of the smoothing are given in Fig. 3.9b as the solid line and show a peak frequency of $0.61\,\mathrm{s}^{-1}$.

A similar method is applied to the wavenumber spectra, the results of which are given in Fig. 3.9c. The vertical wavelengths of the internal waves are approximately the size of the transform window and thus the Fourier series cannot well resolve those values. The smoothing operation gives a more reliable estimate of the vertical wavenumber. Here the bin size for the Gaussian

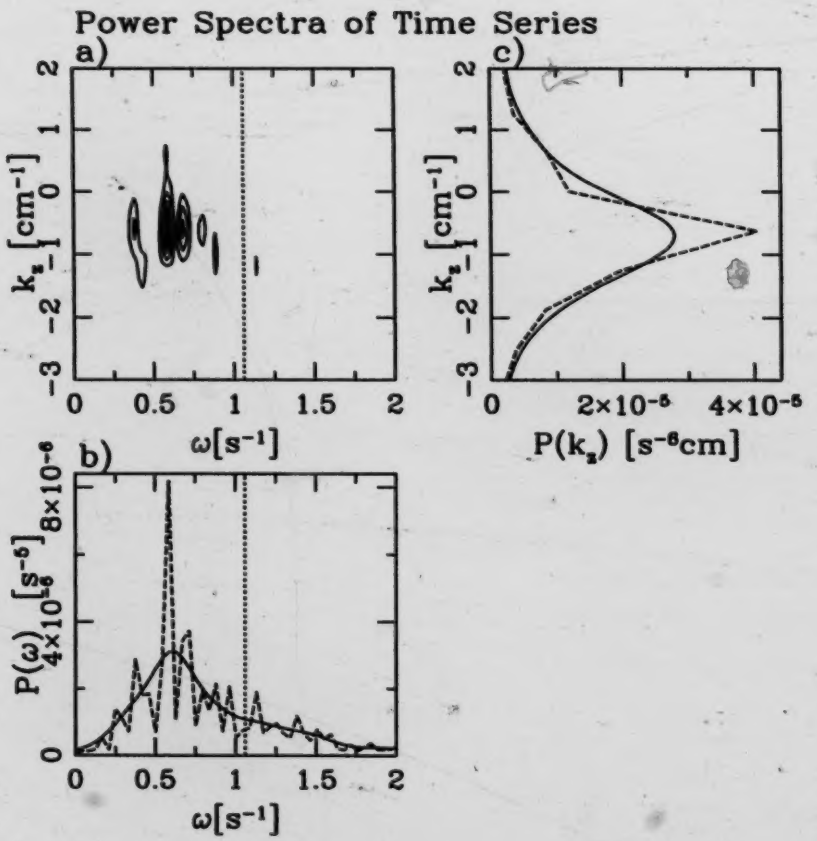

Figure 3.9: The frequencies and wavenumbers present in Fig. 3.4. In a) is the power spectra of the N_t^2 vertical time series in Fig. 3.4 for the range $t = 0$–$150\,\mathrm{s}$ and $z = 17 - 27\,\mathrm{cm}$. The maximum value is 1.3×10^{-3} s^{-5}cm with contours every 2×10^{-4}. The $k_z - \omega$ spectra is averaged over all k_z values, and the resulting ω-profile is given as the dashed curve in b). The solid line is the Gaussian smoothing to the ω-profile. The vertical dotted line indicates the buoyancy frequency. In c) is the k_z-profile from the $k_z - \omega$ spectra averaged over all ω values, as well as the smoothed data.

smoothing is $0.5\,\mathrm{cm}^{-1}$, approximately the extent of the vertical wavenumber resolution. The maximum of the smoothed curve occurs at $k_z = -0.68\,\mathrm{cm}^{-1}$. Though the errors are comparable to the value of $|k_z|$ itself, this analysis at least re-affirms that the spectral analysis captures downward propagating

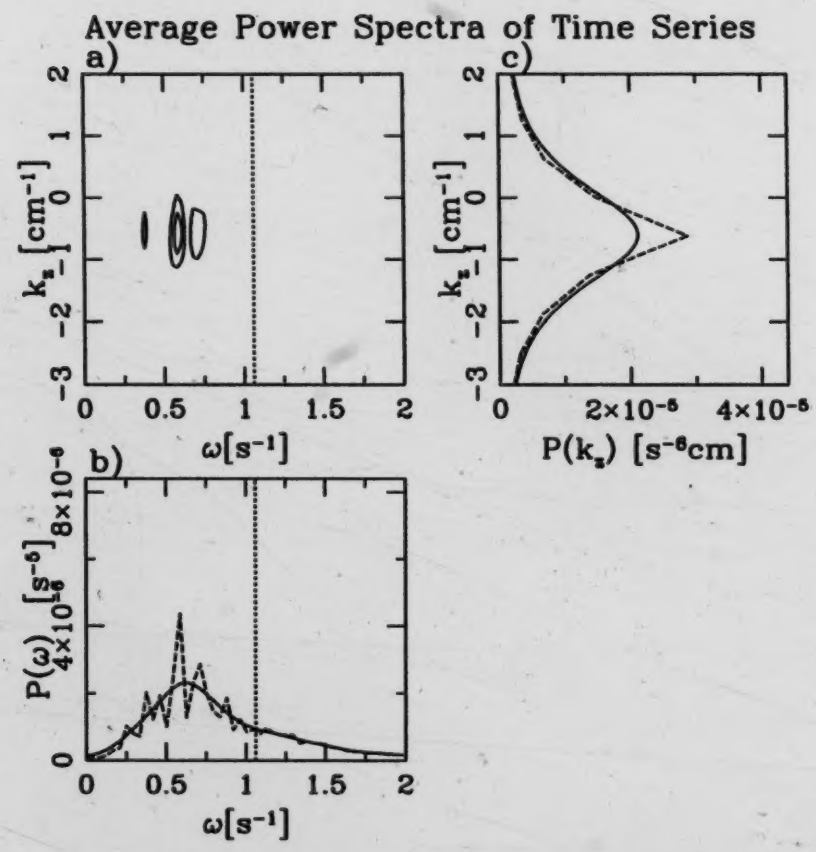

Figure 3.10: Average frequency and wavenumber information for the experiment in Fig. 3.4. a) The individual power spectra are calculated for each of 23 time series across the tank, then averaged. The individual frequency and vertical wavenumber profiles are calculated as in Fig. 3.9 b) and c), respectively, from the averaged spectra in a). All plots are on the same scale as Fig. 3.9.

waves.

For a statistically more accurate measure of the frequencies present throughout the entire wave field, rather than at a single horizontal position, the power spectra are calculated for each N_t^2 field and then averaged across all 23 time series, resulting in the single power spectra given in Figure 3.10a. The same averaging and smoothing method is applied to the averaged spectra, the results of which are in Fig. 3.10b and c, and shown on the same scale as Figure 3.9.

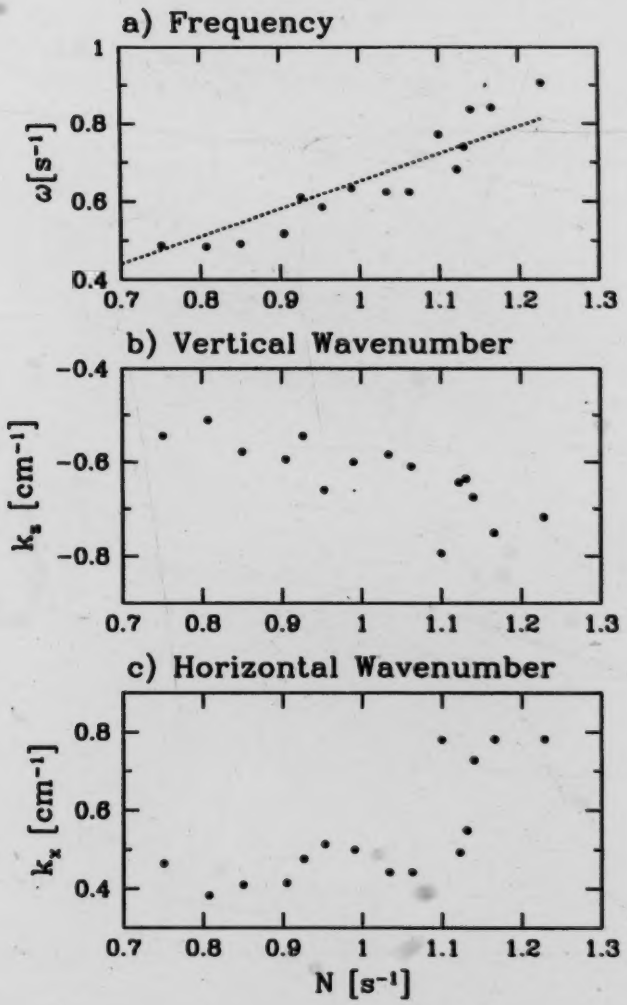

Figure 3.11: The trend in dominant internal wave frequencies and wavenumbers with experimental parameter N calculated from the peaks of the average ω and k_z profiles such as in Fig. 3.10b) and c). Horizontal wavenumbers, k_x, are calculated from k_z, ω and N. The best-fit line to the frequency data and the origin, $(\omega, N) = (0, 0)$, is shown in a) and has a slope of 0.71 ± 0.05. This trend corresponds to waves with an angle of propagation to the vertical of $\Theta = 45°$.

The averaging process does not increase the breadth of the spectrum. However, the profiles exhibit less pronounced peaks. For this particular experiment we find $\omega = 0.62\,\mathrm{s}^{-1}$ and $k_z = -0.61\,\mathrm{cm}^{-1}$.

The power spectra analysis is performed on all experiments, and the peak values for the averaged spectra are given in Figure 3.11, plotted against N. In Fig. 3.11a the measured frequencies follow an increasing trend, and in Fig. 3.11b the measured vertical wavenumbers, although difficult to resolve, seem to follow a decreasing trend. To eliminate any bias between experiments based on transform box size, all fields are Fourier transformed from $t = 0 - 150\,\mathrm{s}$ and from the base of the mixing region to 10 cm below the mixing region. Fig. 3.11c shows the corresponding horizontal wavenumber, k_x, calculated from the measured values ω, k_z and N, and using the linear dispersion relation (B.1).

To measure the amplitudes of the waves in the tank, the rms average of the N_t^2 field is calculated for $t = 30 - 150\,\mathrm{s}$ and the result is multiplied by $2^{1/2}$. The first 30 seconds is not included in the average in order to ensure a fully developed wave field. For example, the results for the experiment in Fig. 3.4 are given in Figure 3.12. In Fig. 3.12a are the amplitude results for the single N_t^2 field. The wave amplitudes, although fluctuating, tend to decrease with distance away from the turbulent region (approximately at $z = 27\,\mathrm{cm}$). The average of all 23 time series across the tank is given in Fig. 3.12b. The dashed lines indicate the standard deviation of the 23 time series.

To characterize the overall amplitude of the waves for each experiment, a best-fit line is taken through $z = 14 - 25\,\mathrm{cm}$ (dotted line in Fig. 3.12b) and the amplitude at the base of the turbulent region is calculated based on the best-fit line. The results of this calculation over all experiments is given in Figure 3.13a. For Boussinesq linear plane waves in a uniformly stratified fluid, the amplitude of the N_t^2 field, $A_{N_t^2}$, is related to the vertical displacement, A_ξ,

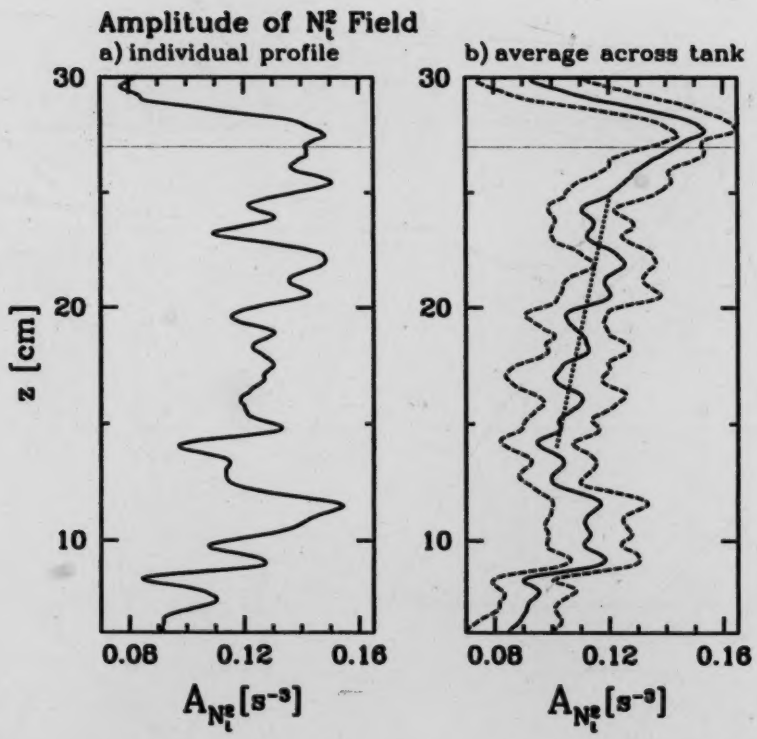

Figure 3.12: Amplitude measurements of the N_t^2 field. In a) the amplitude of the N_t^2 field in Fig. 3.4 is calculated from the rms average across times $30 - 150$ s resulting in a value for the field as a function of z. In b) is the average and standard deviation (dashed lines) of the profiles for the 23 time series across the tank. The best-fit line used to calculate the overall value for the amplitude at the base of the turbulent region is included (dotted line). The base of the turbulent region extends to $z = 27$ cm and is marked by the horizontal line.

by

$$A_{N_t^2} = k_z \omega N^2 A_\xi, \tag{3.5}$$

This relation, along with relations of other wave fields to the vertical displacement is provided in Appendix A. In Fig. 3.13b is the calculated vertical displacement amplitude determined in each experiment based on the previ-

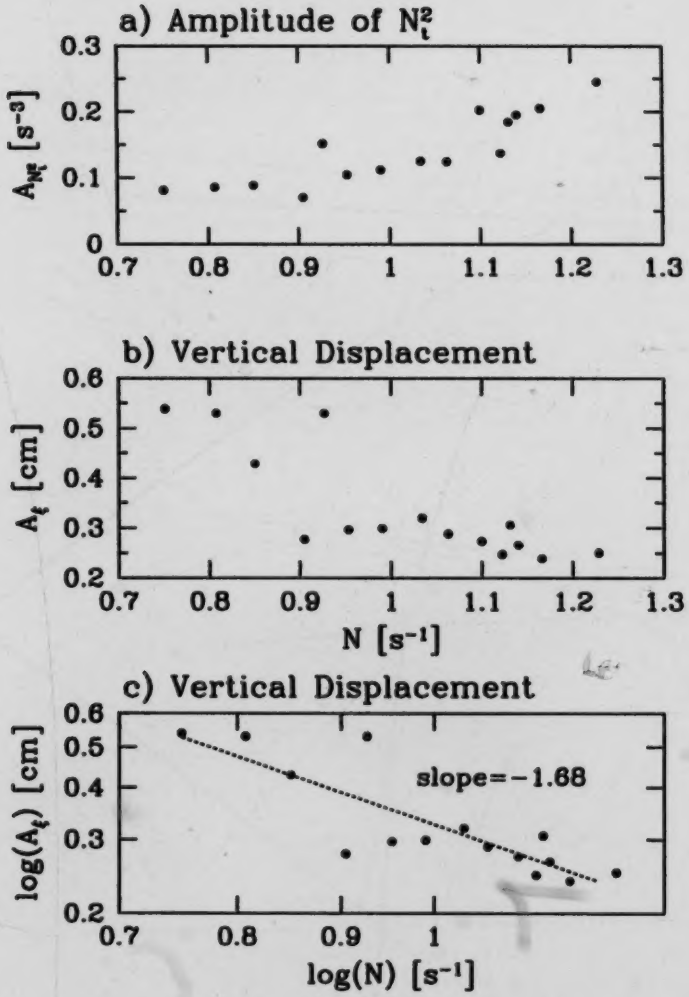

Figure 3.13: The overall amplitude measurements of the schlieren experiments as a function of the stratification, N. In Fig. 3.13a) is the amplitude of the N_t^2 field. In Fig. 3.13b) is the vertical displacement amplitude, A_ξ calculated using (3.5). In Fig. 3.13c) is the vertical displacement amplitude, A_ξ on a logarithmic scale and the best-fit line with slope -1.68 ± 0.04.

ous results for ω, k_z and N. The amplitude measurements generally have a decreasing trend. To compare these results for turbulent jet-scale waves with those of tank-scale waves (Fig. 3.8b), the best-fit line to the logarithmic plot of the vertical displacement is shown in Fig. 3.13c. The slope of the best-fit

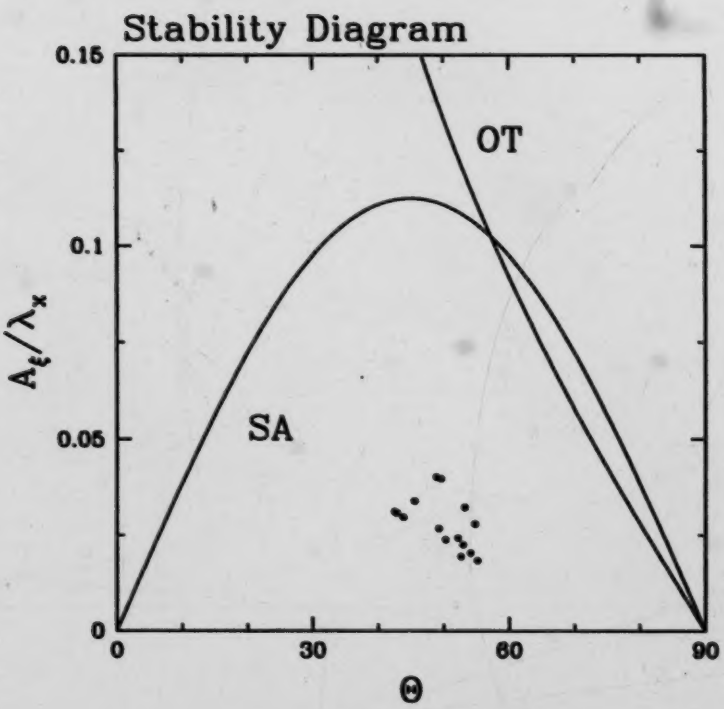

Figure 3.14: The relative amplitudes A_ξ/λ_x of the downward propagating internal waves plotted against their angle of propagation to the vertical, Θ. The curve denoted "SA" is the critical relative amplitude at which the waves at that angle should become unstable by self-acceleration. The curve denoted "OT" is the relative amplitude at which the waves should overturn.

line suggests a power law relationship of the form

$$A_\xi \sim N^{-1.68}. \tag{3.6}$$

To illustrate the significance of the vertical displacement amplitude of these waves, in Figure 3.14 A_ξ is divided by the corresponding horizontal wavelength, λ_x, (as calculated from k_x) and plotted against the angle of propagation of the waves with respect to the vertical, Θ. Explicitly, $\Theta = \tan^{-1}(|k_z|/k_x) =$

$\cos^{-1}(\omega/N)$. Linear theory predicts A_ξ/λ_x and $A_{N_i^2}$ are related by

$$\frac{A_\xi}{\lambda_x} = \frac{1}{2\pi} \frac{1}{N^2\sqrt{N^2-\omega^2}} A_{N_i^2} \tag{3.7}$$

(see Appendix A). The calculation of relative amplitude from the schlieren field, $A_{N_i^2}$, involves only the more reliable measured values N and ω and not the values of k_z and k_x.

Surprisingly, we find that across all experiments the properties of the dominant small-scale waves collapse onto a narrow range of relative amplitude and angles of propagation.

Included in Fig. 3.14 are the critical amplitudes for two types of internal wave instabilities. For plane internal waves to become statically unstable, relatively dense fluid is lifted by the waves to the extent that it overlies less dense fluid. The critical relative amplitude for this instability is given by:

$$\frac{A_\xi}{\lambda_x} \equiv A_{OT} = \frac{1}{2\pi} \cot\Theta \tag{3.8}$$

where "OT" denotes overturning. The second instability is one in which waves interact resonantly with the wave-induced mean flow. The critical amplitude, when the maximum horizontal velocity of the wave-induced mean flow matches the horizontal group velocity of the waves, is given by

$$A_{SA} = \frac{1}{2\pi\sqrt{2}} \sin 2\Theta. \tag{3.9}$$

The "SA" denotes self-acceleration condition. Details can be found in Sutherland (2001).

Our analyses show that the waves generated below the turbulent mixing

region are large in that their vertical displacement amplitude is $2-4$ percent of their horizontal wavelength and approximately one quarter of the amplitude at which they would break.

The angles of wave propagation to the vertical all lie within $\Theta = 42° - 55°$, with an average value of 50°. Thus, although turbulent eddies can excite a broad frequency spectrum, the largest amplitude waves have a frequency that is an approximately constant function of N.

If the waves experience a significant decay within a short distance from the generation region, one would expect to observe the waves with the fastest vertical group velocity below the mixed region because these can travel the furthest before the effects of dissipation and diffusion reduce their amplitude. However, this explanation for our observations is unsatisfactory, as demonstrated by Figure 3.15. This shows a continuation of the laboratory time series begun after the oscillating grid was stopped. At the bottom of the figure is a plot of the root-mean-square wave field in time and averaged over $5 \leq z \leq 25\,\mathrm{cm}$. The waves decay slowly and require 30 buoyancy periods in order to decay by 50 percent. Within 10 buoyancy periods, the wave field fills the tank, which suggests that the spectrum of the wave field in Fig. 3.9 would be much broader and the dominant frequencies in Fig. 3.14 would lie closer to those corresponding to $\Theta = 35°$ if the observed angle of propagation was due to differences in group velocity.

Although the amplitude of the waves is large enough that nonlinear effects may become important, it is unlikely that such weakly nonlinear effects as wave-wave interactions become significant during the course of an experiment. Corroborating evidence is given by experiments by McEwan (1971) designed to examine interactions between free wave modes and a forced standing wave.

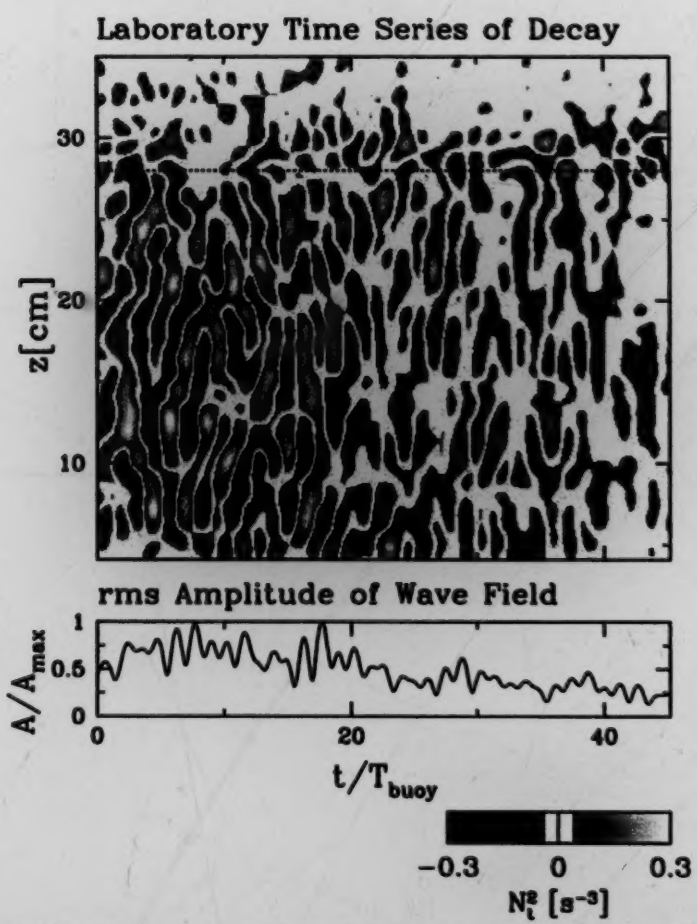

Figure 3.15: Time series for the laboratory experiment in Fig. 3.4, started as the oscillating grid is turned off, to show the decay of the wave field in time. The mixed region extends to $z = 28\,\text{cm}$. A plot of the root-mean-square amplitudes over the range $5 \leq z \leq 25\,\text{cm}$ is provided below, normalized by the maximum amplitude in the wave field.

He found that the growth of secondary modes depended on the amplitude of the fundamental modes and the buoyancy frequency such that for N between 0.35 and 1.69 s^{-1} the critical (nondimensional) amplitude A_ξ/λ_x ranged from 0.01 to 0.03. Although the amplitudes of the strongest waves observed in our experiments are within this range, even in the ideal circumstance of the monochromatically-forced experiments the evolution of secondary waves required times on the order of 40 buoyancy periods, longer than the duration of our experiments.

In follow-up experiments McEwan and Plumb (1977) examined the nonlinear interaction between a long-wave and a fine-scale wavepacket and found that the interaction mechanism was sensitive to irregular forcing of the long wave, requiring much larger amplitudes to maintain instability than with continuous regular forcing. When resonant interactions did occur, the result was the generation of an equal and opposite wavepacket, which arrested the downward propagation of the packet and resulted in a standing wave. This feature is not observed in our experiments.

Furthermore, on the basis of his 1971 experiments, McEwan concluded that the resonant modes could be assumed to be linearly independent. Likewise although the waves in our experiments are moderately large amplitude, we believe the use of linear theory to calculate wave properties is justified.

3.5 Discussion

Dye-line and schlieren analyses reveal two scales of internal wave motions. The large-scale motions have a modal (tank-scale) structure and small-scale transient wavepacket bursts are observed on the scale of the turbulent jets. These

results suggest that there are two mechanisms for generating internal waves from the turbulence in our experimental situation. One generation mechanism appears to be the two counter-rotating vortices in the turbulence. The other is from "bursts" of turbulent jets that break into the stratified region. These bursts are not on the scale of the smallest eddies, but rather on an intermediate scale between the smallest eddies and the tank-scale circulation. Our observations suggest that the two wave excitation phenomena are decoupled.

A high aspect-ratio tank has necessarily been used for these experiments in order to visualize and measure quasi-two-dimensional waves. Even in mixing box experiments performed in tanks with square horizontal cross-sections, large-scale circulations are observed to develop in the mixing region. An advantage of the high aspect-ratio geometry is that we can analyze the structure of the circulation and the tank-scale internal wave modes it generates. We are also able to measure the scale of turbulent jets that excite downward-propagating waves. Because the scale of these jets is on the order of the tank width we are able to measure the wave characteristics, such as frequency and amplitude, using synthetic schlieren.

The small-scale wave field observed is not a random superposition of arbitrary waves. Rather than exhibiting a broad spectrum of frequencies, the internal waves instead show a narrow range of frequencies centered on a constant fraction of the buoyancy frequency, $\omega \approx 0.7N$. As well, the amplitudes of both large- and small-scale waves have an inverse dependence on the buoyancy frequency as $A_\xi \sim N^{-1.5\pm0.2}$. The wave amplitudes are a substantial fraction of their potential breaking amplitudes. Insights and proposed explanations of these results are gained through numerical simulations discussed in the chapters that follow.

Chapter 4

Numerical Simulations - Large Scale Forcing

4.1 Introduction

Large-scale waves on the same scale as the mean circulation in the mixed region were observed in the laboratory experiments, and appeared to be continuously generated by the action of the stationary vortices. We have continued this investigation of the generation of internal waves from a mixed layer using numerical simulations with a large-scale forcing to a mixed region in the form of two counter-rotating vortices, such as observed in the laboratory experiments. The numerical simulations model a uniformly stratified Boussinesq fluid underlying a homogeneous mixed region. The simulations solve the fully nonlinear, nonhydrostatic, Navier-Stokes and mass conservation equations in two dimensions.

4.2 Numerical Model

4.2.1 Model Description

The simulations solve the equations for the basic-state fields of vorticity, ζ, and perturbation density, ρ, which are as follows, in dimensional units:

$$\frac{D\zeta}{Dt} = \frac{g}{\rho_0}\frac{\partial \rho}{\partial x} + \nu \nabla^2 \zeta + F_\zeta \tag{4.1}$$

$$\frac{D\rho}{Dt} + w\frac{d\overline{\rho}}{dz} = \kappa \nabla^2 \rho \tag{4.2}$$

where subscripts denote partial derivatives, $D/Dt = \partial/\partial t + \mathbf{u}\cdot\nabla$ is the material derivative, ρ_0 is the density at a reference level, ν is the kinematic viscosity, κ is the substance diffusivity, and the pressure and density are expressed in terms of their background and perturbation values:

$$\rho_{total} = \overline{\rho}(z) + \rho(x,z,t) \tag{4.3}$$

$$p_{total} = \overline{p}(z) + p(x,z,t) \tag{4.4}$$

$$\frac{d\overline{p}}{dz} = -\overline{\rho}g. \tag{4.5}$$

The vorticity field is forced with the term F_ζ, described in the sections below.

Consistent with the Boussinesq approximation, the fluid is incompressible. Hence

$$u_x + w_z = 0. \tag{4.6}$$

Therefore, one can define a streamfunction which is related to the horizontal and vertical velocity components by $(u, w) = (-\psi_z, \psi_x)$, so that the velocities

can be determined from the vorticity by inverting the elliptic equation:

$$\nabla^2 \psi = -\zeta. \tag{4.7}$$

Equations (4.1) and (4.2) are evolved using second order finite differences in the vertical, Fourier spectral methods in the horizontal, and are stepped forward in time using a leapfrog method with an Euler backstep every 20 time intervals to minimize splitting errors. The details of the numerical model are given in Sutherland and Peltier (1994).

The domain is a horizontally periodic channel with free-slip upper and lower boundary conditions. In the simulations reported upon here the domain extends from $-20 \leq x \leq 20\,\text{cm}$, and either $0 \leq z \leq 80\,\text{cm}$ or $-80 \leq z \leq 80\,\text{cm}$. The domain is set to be of comparable width to the laboratory experiments, but approximately twice as deep, in order to delay bottom reflection and to ensure observations of the downward propagating waves alone. The spatial resolution of the simulations are either $\Delta x = \Delta z = 0.16\,\text{cm}$ or $\Delta x = \Delta z = 0.08\,\text{cm}$, with a temporal resolution of $\Delta t = 0.002\,\text{s}$. The domain size is chosen as a compromise between extending the wave region and computation time. For example, a simulation with $-80 \leq z \leq 80\,\text{cm}$ requires approximately 2 hours using 16 CPUs on the WestGrid supercomputer cluster (www.westgrid.ca) to run one second of the simulation. Simulations are run typically for 60 s, requiring a total of 2000 CPU hours.

4.2.2 Initial Conditions

The mixed layer is simulated by a homogeneous top layer that overlies a uniformly stratified region. The initial stratification is given by:

$$N = \begin{cases} 0 & 60 \leq z \leq 80 \\ N_0^2 & 0 \leq z < 60. \end{cases}$$

The values of the physical parameters are $\nu = 0.01\text{cm}^2/\text{s}$, $\text{Pr} = \nu/\kappa = 1$ and a range buoyancy frequencies $N_0^2 = 0.1 - 10\,\text{s}^{-2}$. The kinematic viscosity is chosen to be that of water. The unphysically high value for the diffusivity, $\kappa = \nu$, is chosen in order to damp out small-scale numerical noise and so maintain numerical stability. The vorticity field in the mixed region is continuously forced by the term $F_\zeta(x, z, t)$ in equation (4.1).

Two counter-rotating vortices are continuously forced in the mixed region as shown, for example, in the spatial view in Figure 4.1b. Explicitly,

$$\begin{aligned} F_\zeta &= F_0 \exp\left[-\frac{1}{2}\left(\frac{(x+10)^2 + (z-70)^2}{\sigma^2}\right)\right] \\ &- F_0 \exp\left[-\frac{1}{2}\left(\frac{(x-10)^2 + (z-70)^2}{\sigma^2}\right)\right]. \end{aligned} \tag{4.8}$$

The value of the forcing amplitude, F_0, is varied between $F_0 = 0.001 - 1\text{s}^{-2}$. The width of the Gaussian vortices is varied between $\sigma = 0.5$ and $\sigma = 2.0\,\text{cm}$. This forcing to the vorticity is added at every time step. The vortices are symmetrically placed within the mixed region. Otherwise, the horizontal balance of vorticity is broken if the vortices are either asymmetrically placed in the horizontal, or if the aspect ratio of the mixed region is not 1:1. In such cases, a mean flow develops in the mixed region.

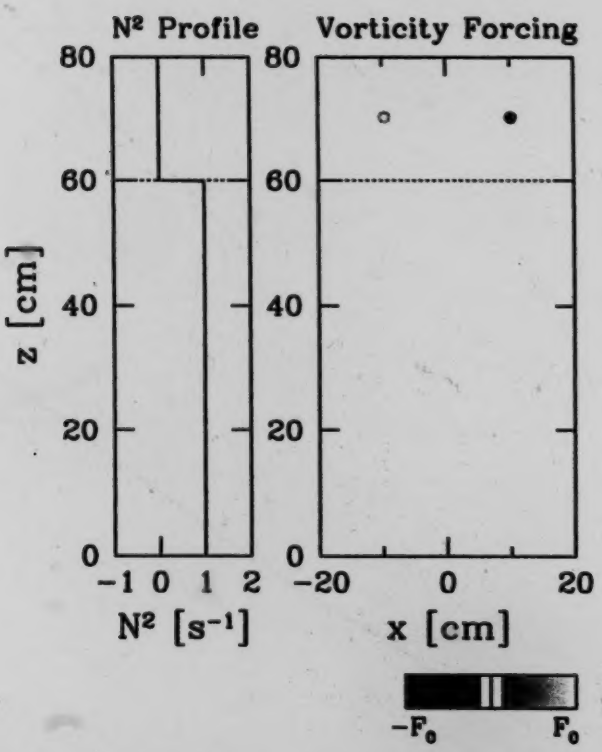

Figure 4.1: a) Background N^2 profile. The mixed region extends from $60 < z \leq 80\,\mathrm{cm}$, with linear stratification underneath. b) Spatial forcing to the vorticity. The mixed region is continually forced with 2 counter-rotating Gaussian vortices, centered within the mixed region.

4.2.3 Damping of the Mixed Region

With viscosity fixed at $\nu = 0.01\,\mathrm{cm}^2/\mathrm{s}$, this continual large-scale forcing to the mixed region results in a continual increase of energy in this region. In the first set of simulations described in this section, no artificial damping is added to the mixed region. The forcing amplitude is kept low, at $F_0 = 0.1\,\mathrm{s}^{-2}$. Larger values of forcing result in the rapid development of fine filament structures which lead to numerical instability. The radius of the vortices is $\sigma = 2\,\mathrm{cm}$, which is large enough to generate a mean circulation, but small enough so that the vortices do not interact. The time-scale for viscous diffusion, based

on a vortex of area $4\pi\,\mathrm{cm}^2$ is on the order of $4\pi/0.01 \approx 1200\,\mathrm{s}$, which is much longer than the simulation run times of 60 s.

To counteract the potential influence of the increasing energy in the mixed region, in the second set of simulations a Rayleigh damping term, $-r\zeta$, is added to the forcing in the mixed region, in which the damping constant $r = 0.1$. In these simulations the forcing amplitude is $F_0 = 1.0\,\mathrm{s}^{-1}$ and the width of the vortices is set at the smaller value of $\sigma = 0.5\,\mathrm{cm}$. At each time step the forcing is added to the mixed region, and Rayleigh damping removes $r\zeta$ from the vorticity field. Steady-state is achieved through a balance between Rayleigh damping and forcing, not through viscosity. This occurs on a time-scale on the order of time $\tau = 1/r$. For our simulations, $\tau = 10\,\mathrm{s}$. In Figure 4.2 are plots of the average perturbation kinetic energy within the mixed region for both types of simulations. Consistent with our order of magnitude estimate, near steady-state is reached between 25 and 50 s in Fig. 4.2b.

4.3 Observations

4.3.1 Wave Fields

A sample vertical displacement field is shown in Fig. 4.3. The basic state field for the simulations, the perturbation density field, is scaled by $d\bar{\rho}/dz$ below $z = 60\,\mathrm{cm}$ so the results correspond to the vertical displacement for linear internal waves (Appendix A). Hence, in the figures that follow, the perturbation density field will be referred to as the vertical displacement field, ξ. In Fig. 4.3 the vorticity field is superimposed on the figure to show the structure of the vortices. Below the mixed region, waves are generated by

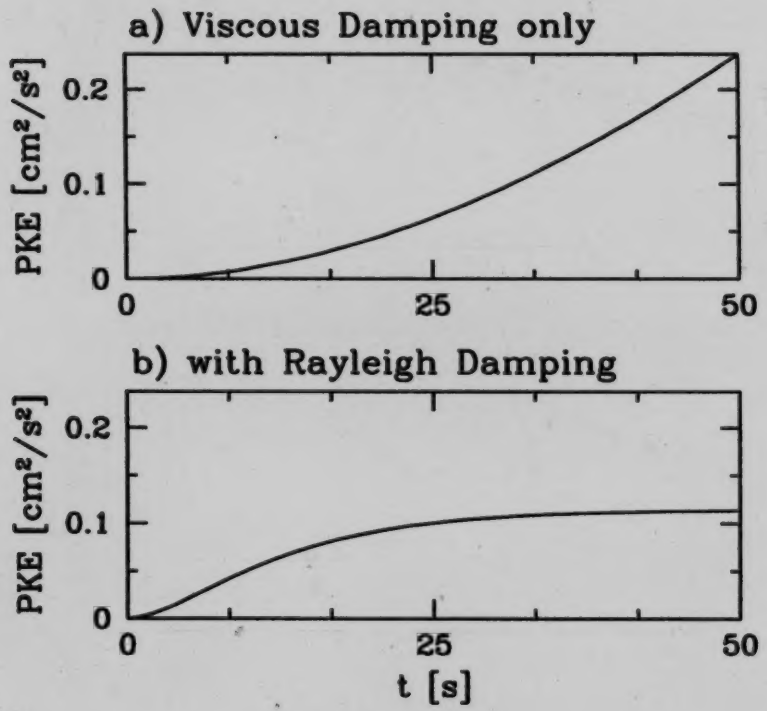

Figure 4.2: Average perturbation kinetic energy within the mixed region as it evolves in time. a) Damping of the energy is due to only the effects of viscosity (of water). $F_0 = 0.1\,\mathrm{s}^{-2}$ and $\sigma = 2\,\mathrm{cm}$. b) Rayleigh damping is added to the mixed region. $F_0 = 1.0\,\mathrm{s}^{-2}$ and $\sigma = 0.5\,\mathrm{cm}$.

the motion of the vortices and have the same horizontal mode 2 structure as observed in the experiments. The waves propagate downward in time with upward phase propagation. Dense fluid is pulled up the sides of the domain, with the edge of the mixed region pushing into the dense fluid in the middle of the domain. The vertical domain of these simulations is extended to $-80 \leq z \leq 80\,\mathrm{cm}$ to avoid bottom reflection over the times of interest.

In the laboratory experiments, the spectra of frequencies present in the vertical motions of the isopycnal layers were complicated, with several peaks

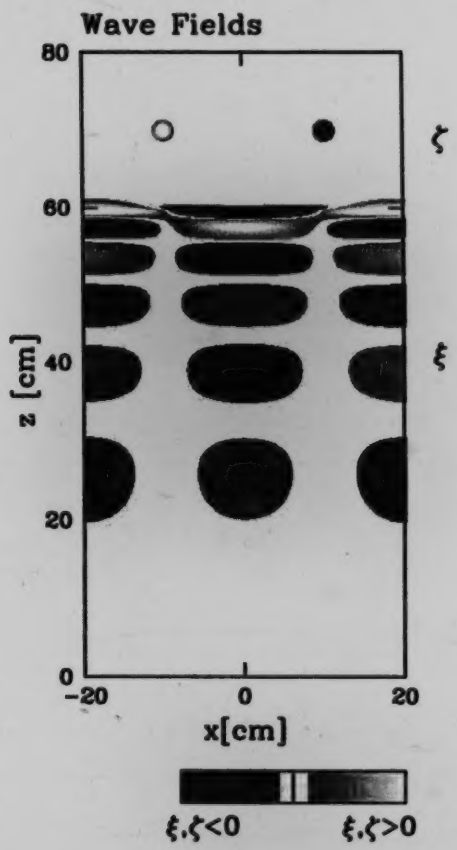

Figure 4.3: The vorticity field, ζ, (visible for $z > 60$) is superimposed on the vertical displacement field, ξ, (mostly visible for $z < 60$). Both fields are at $t = 3T_{buoy}$ for a numerical simulation with $N = 1.0\,\mathrm{s}^{-1}$. The dimensions of the simulation extend beyond the figure to $z = -80\,\mathrm{cm}$. Both fields are normalized and the colour map indicates regions of positive and negative fields.

that did not correspond to the simplest vertical modes. Fig 4.3 qualitatively shows the dispersive nature of the wave field and aids in understanding the experimental results. The vertical wavelengths vary with distance from the mixed region (or alternatively, with time) and there is no modal structure in the vertical.

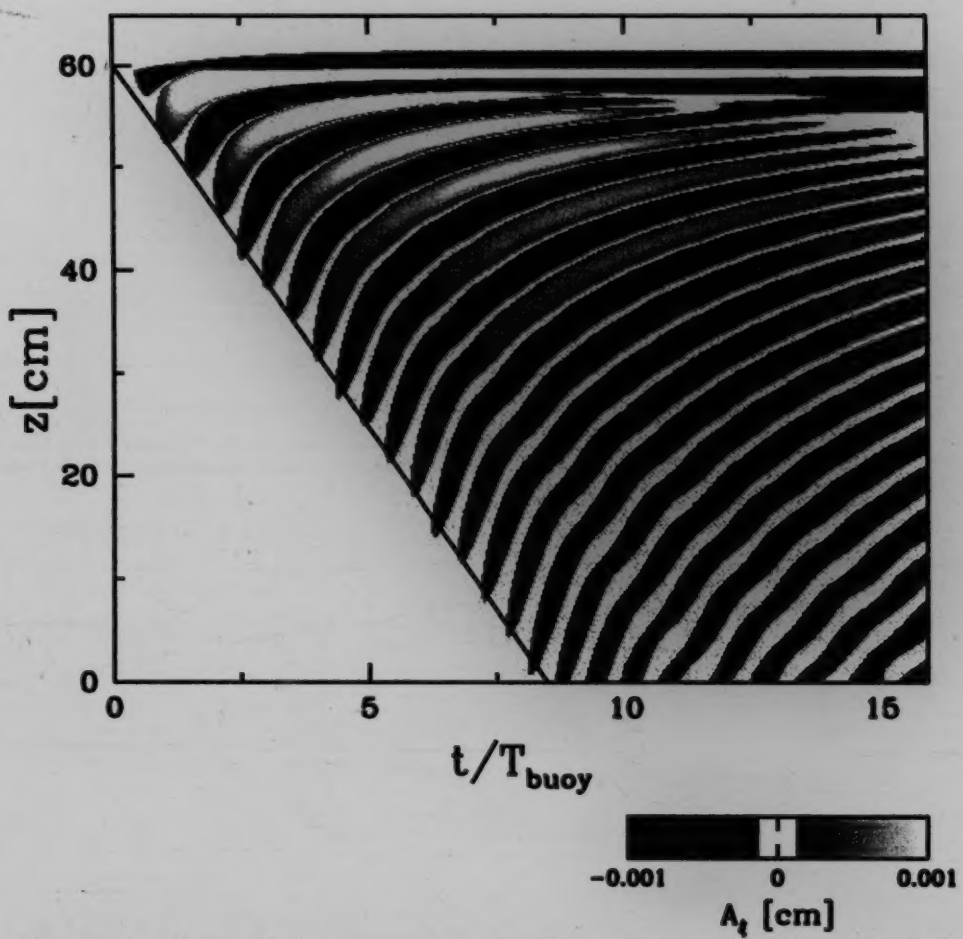

Figure 4.4: A sample false-colour vertical time series image for a simulation with $N = 1.0\,\mathrm{s}^{-1}$. The horizontal location of the time series is at $x = 10.0\,\mathrm{cm}$. The time series is scaled with the buoyancy period.

4.3.2 Time Series

Figure 4.4 is a vertical time series for a simulation with Rayleigh damping, and with a value of the buoyancy frequency of $N = 1.0\,\mathrm{s}^{-1}$. The wave field disperses as the waves travel down through the tank with the longer wavelengths travelling faster than the shorter wavelengths. Following a wave crest in the time series, the vertical position of the crest is approximately determined by

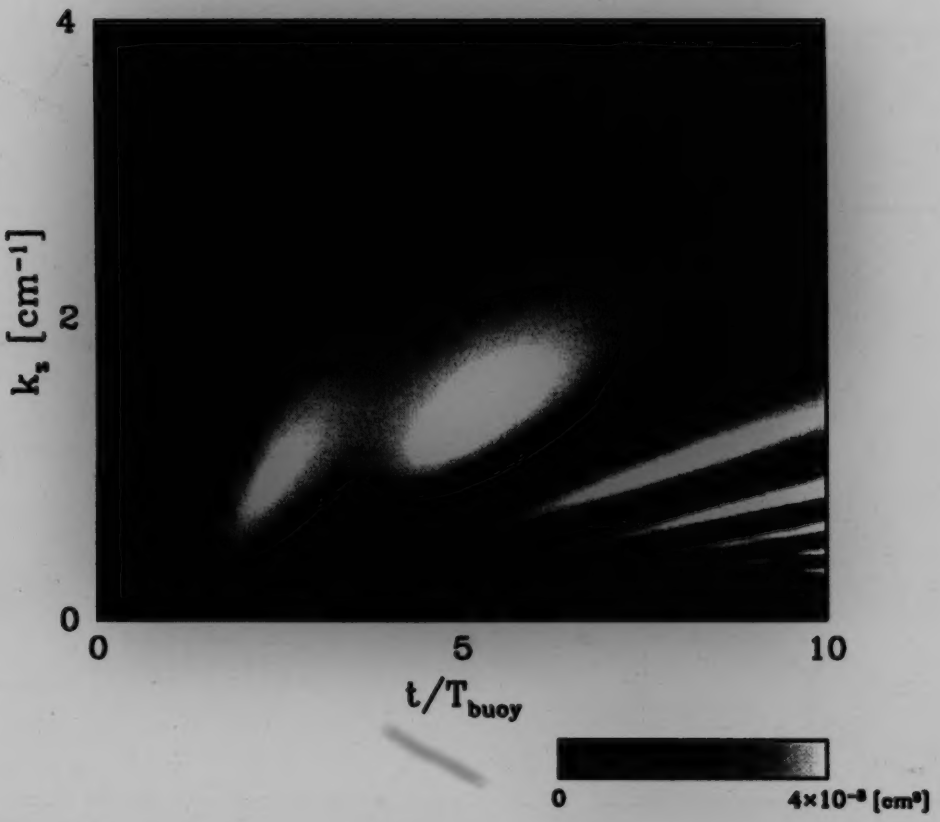

Figure 4.5: Spectrum of vertical wavenumbers in Fig. 4.4 as they vary in time. Pure white regions indicate squared Fourier amplitudes greater than $4 \times 10^{-8}\,\mathrm{cm}^3$ to a maximum value of $4 \times 10^{-7}\,\mathrm{cm}^3$.

$z = 8t^{1/3}$. For a range of simulations with $N = 0.1 - 10\,\mathrm{s}^{-1}$, covering two decades of buoyancy frequency, the time series all initially follow the pattern of the time series shown when scaled in time with T_{buoy}.

The diagonal line in Fig. 4.4 illustrates the maximum vertical group velocity for waves with a wavelength of 20 cm (the extent of one vortex). Explicitly, $c_{gz} = \frac{N}{k_x}\cos^2(\Theta)\sin(\Theta)$, which is maximized for waves travelling at $\Theta \approx 35°$. Waves travelling at the maximum group velocity for the observed horizontal wavelength of 40 cm (see Fig. 4.3) would have twice this velocity. Surprisingly, it appears the subharmonic modes dominate the energy transport.

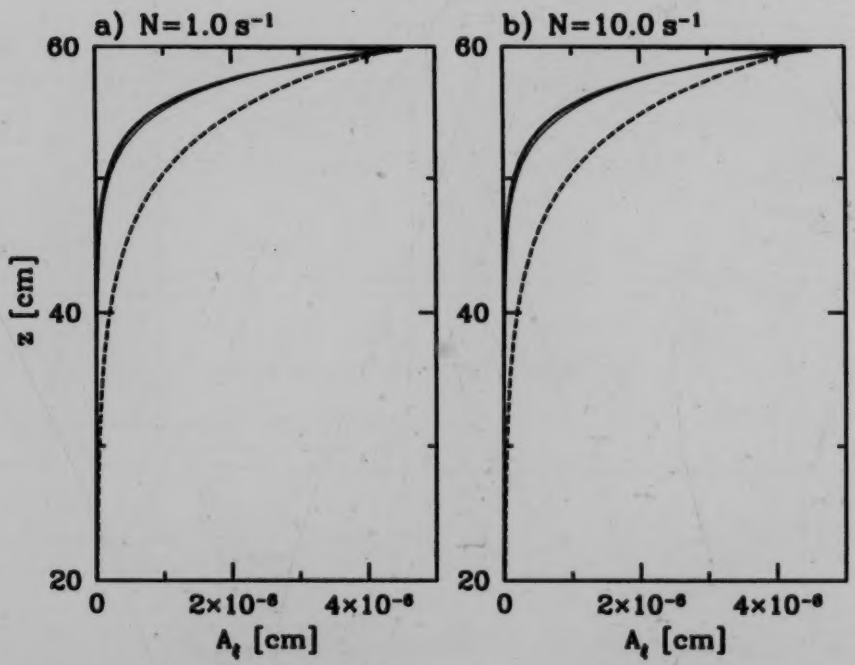

Figure 4.6: The profile of the initial vertical displacement field amplitude at x=-10 cm, t=1 s. a) $N = 1.0\,s^{-1}$. b) $N = 10.0\,s^{-1}$. Included are two curves for the exponential decay of amplitude from source for $k_x = 20$ cm (dotted) and $k_z = 40$ cm (dashed).

Looking at the vertical wavenumbers present in the above time series, one can again see the dispersive nature of the wave field. Figure 4.5 shows the power spectrum of waves as it varies in time. The spectrum broadens in time, with no dominant vertical wavelength. In particular, the period of the initial packet of waves is near the buoyancy period, which corresponds to nearly infinite vertical wavelengths. Until the initial wave group reflects off of the bottom (at $t \approx 7T_{buoy}$) the results correspond very closely to simulations with $0 \leq z \leq 80$ cm.

The stratified region responds to the initial appearance of the vortices within the mixed region as it does to an impulse: all vertical wavelengths are

generated. The strongest signal occurs initially when all wavenumbers are generated. The wavefield shows an exponential decay with distance from the mixed region, as for evanescent waves, with an e-folding scale on the order of the width of the tank. The initial exponential form of the wavefield is shown in Figure 4.6.

If the initial wave field is a response to an impulsive force with all frequencies and vertical wavelengths generated, the vertical structure of the downward-propagating wave field will follow for the highest frequencies:

$$\begin{aligned} A_\xi(z,t) &= A_0 \exp[i(k_x z - \omega t)] \\ &= A_0 \exp[k_x z\sqrt{1 - N^2/\omega^2} - i\omega t] \\ &\approx A_0 \exp(k_x z) \exp[-\frac{1}{2} k_x z N^2/\omega^2 - i\omega t], \end{aligned} \tag{4.9}$$

in which it is understood one takes the real part of these expressions. Here we have used the dispersion relation for internal waves (A.9) taking the branch cut for downward propagating and bounded waves as $z \to -\infty$. Included in Fig. 4.6 are two exponential curves, $\exp(k_x z)$, corresponding to values of $k_x = 20\,\text{cm}$ and $40\,\text{cm}$. The observed initial exponential profile closely follows the $k_x = 20\,\text{cm}$ curve. This horizontal length scale corresponds with the group velocity observation in the time series of Fig. 4.4. It appears that the initial impulse generates a broad spectrum of waves but transport is dominated by waves having a horizontal wavelength on the scale of the single vortex.

The horizontal wavelength is set by the length scale of the forcing, but the vertical wavelength is unconfined. To view this dispersion of vertical wavelengths, in Figure 4.7 is a series of vertical displacement profiles corresponding to the time series in Fig. 4.4.

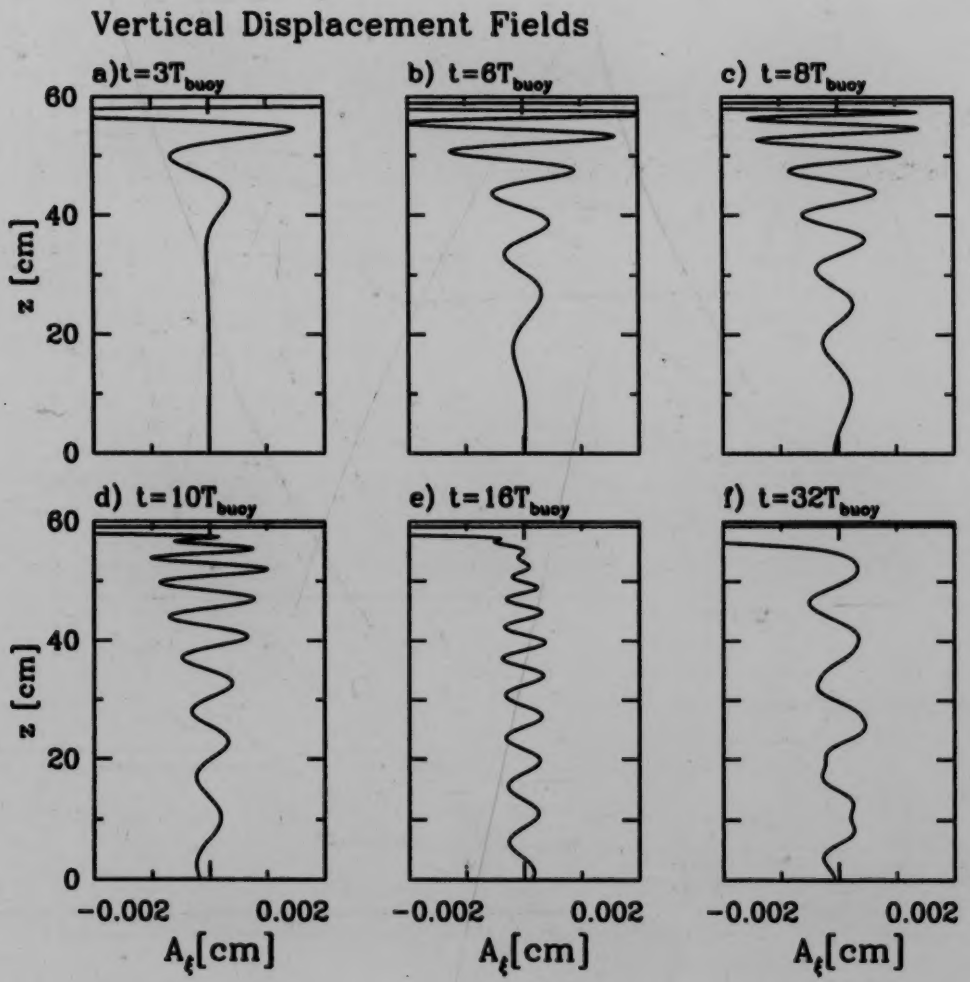

Figure 4.7: Profiles of vertical displacement amplitudes illustrating the variation in vertical wavenumber with time. The profiles are taken from Fig. 4.4 at the corresponding times shown. The forcing to the mixed region reaches steady state at approximately $50\,\mathrm{s} = 8T_{buoy}$.

As time progresses (Figs. 4.7a - c), the longer wavelengths travel faster into the stratified region, although the amplitude continues to decay exponentially from the base of the mixed region. As seen in Fig. 4.2b, however, the kinetic energy in the mixed region does not reach steady state until 50 s ($8T_{buoy}$ for $N = 1\,\mathrm{s}^{-1}$). Once steady state is reached there is a noticeable decrease in the amplitudes in the stratified region (Figs. 4.7d - e). This can also be seen in the upper right-hand corner of Fig. 4.4. The waves continue to be generated, but in part due to weaker forcing and also due to interactions with bottom-reflected waves the exponential envelope to the wave field smooths into an even distribution throughout the column (Fig. 4.7f). The "modal" structure to the horizontal remains throughout the duration of the simulations.

If the forcing to the mixed region is varied as $(1+\epsilon)F_\zeta$, where ϵ is a random number between -0.1 and 0.1, the regular structure seen in the profiles of Fig. 4.7 is modified, but the decay of the wave field's amplitude envelope with distance from the mixed region is unaffected. The perturbation to the stratified region by the vortices (upwelling at the sides, downwelling in the centre) appears to be the dominant source of the initial broad spectrum wave field.

4.4 Results

4.4.1 Wave Amplitudes with No Rayleigh Damping

The dependence of wave amplitude on the buoyancy frequency is first calculated for the more straightforward case of the simulations without the added Rayleigh damping. In a similar manner to the laboratory calculations, rms

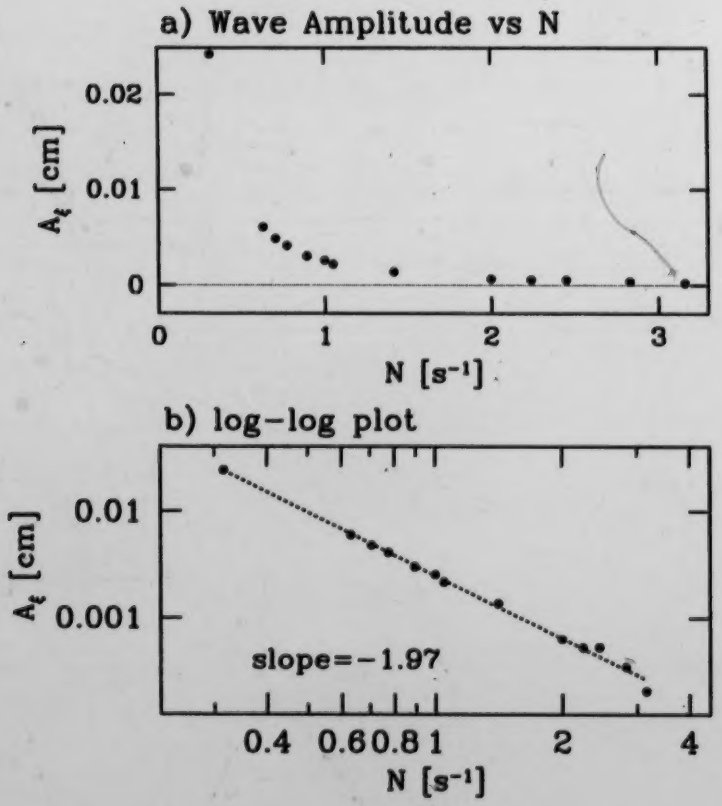

Figure 4.8: a) Variation of A_ξ with N for the simulations without Rayleigh damping. b) Variation on a logarithmic scale. The slope of the best-fit line is -1.97 ± 0.03.

averages of the wave field are calculated over one buoyancy period at one horizontal position, and averaged across a series of 39 horizontal positions across the tank. The results are shown in Figure 4.8 along with the results plotted on a logarithmic scale. The slope of the best-fit line to the logarithmic plot suggests a variation of amplitude with buoyancy frequency as

$$A_\xi \sim N^{-1.97 \pm 0.03}. \tag{4.10}$$

Transient effects non-negligibly contribute to the large magnitude of this

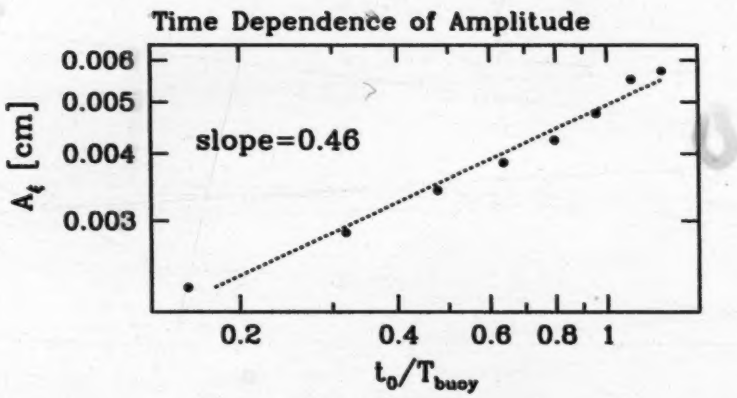

Figure 4.9: Variation of A_ξ with t_0 on a logarithmic scale for the simulations without Rayleigh damping. A_ξ is calculated from the average amplitude over a buoyancy period starting at time t_0. The slope of the best-fit line is 0.46 ± 0.03.

exponent. With no Rayleigh damping, the amplitudes of the wave field at a fixed vertical location increase in time due to the steadily increasing energy in the mixed region, as seen in Fig. 4.2a. An estimate of the time dependence of the wave amplitude is calculated by rms averages across the horizontal of the wave field at a fixed vertical location averaged over one buoyancy period starting at time t_0. In Figure 4.9 is a logarithmic plot of the average wave amplitude as it depends on t_0. In this case,

$$A_\xi \sim \left(\frac{t_0}{T_{buoy}}\right)^{0.46\pm0.03} . \tag{4.11}$$

This result is typical for a wide range of N. Thus, the energy associated with the waves increases approximately linearly in time. Since $T_{buoy} = 2\pi/N$, this time dependence introduces a secondary dependence on the buoyancy frequency as $A_\xi \sim N^{0.46}$. Together with (4.10), this implies a steady-state

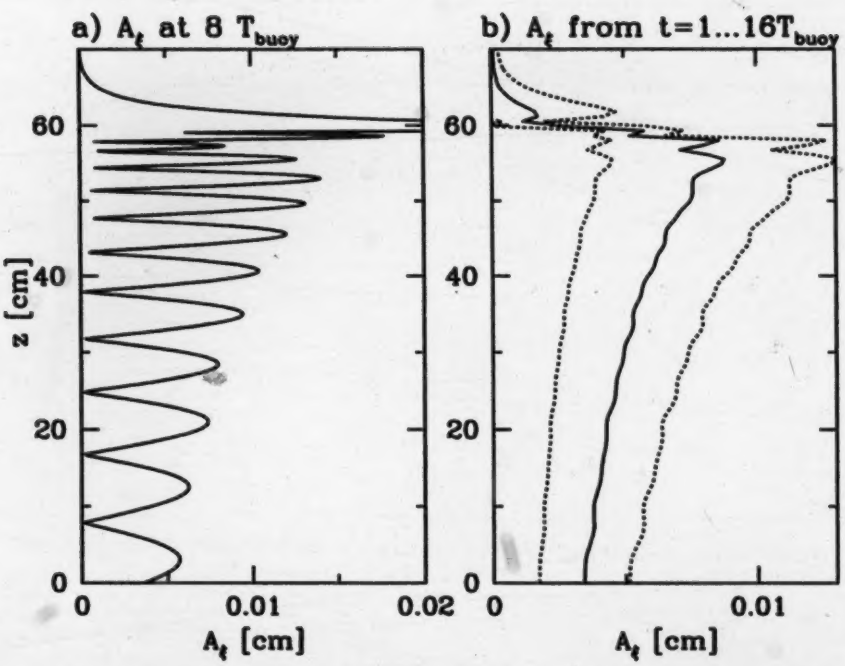

Figure 4.10: Amplitude measurements of the vertical displacement field. In a) the rms horizontal average of the vertical displacement field is calculated at time $t = 8T_{buoy}$. The rms amplitude in time from $t = 1 - 16T_{buoy}$ is calculated from 39 time series. In b) is the average profile and standard deviation (dotted lines).

relation between amplitude and buoyancy frequency of

$$A_\xi \sim N^{-1.51\pm0.05}. \tag{4.12}$$

4.4.2 Wave Amplitudes with Rayleigh Damping

Rayleigh damping is added to the mixed region in order to counteract the steady increase of energy in the mixed region. To continue the investigation into the dependence of the wave amplitude on the forcing and the buoyancy frequency, rms averages are again taken across time series and the results

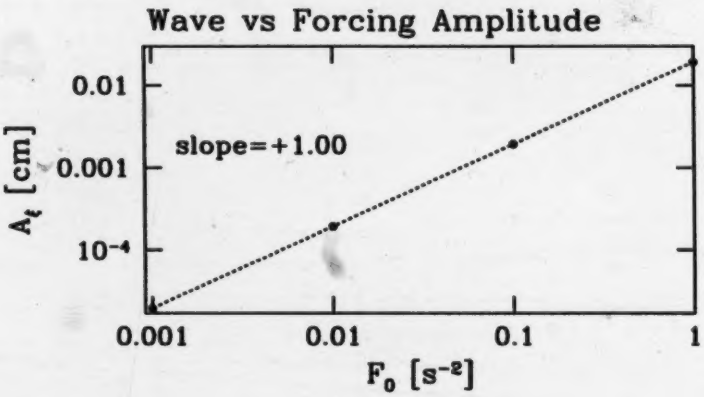

Figure 4.11: Variation of A_ξ with mixed region forcing amplitude, F_0, on a logarithmic scale.

averaged across 39 horizontal positons in the tank.

A sample rms profile for the simulation with $N = 1.0\,s^{-1}$ is provided in Figure 4.10b, along with the horizontal rms profile at $t = 8T_{buoy}$ in Fig. 4.10a. In this simulation the time series are averaged from $t = 1 \ldots 16T_{buoy}$. The standard deviation for the averaging process is included as the dotted lines, as in the laboratory analysis. The amplitudes again decay with distance from the mixed region as evident in the figure.

In a series of simulations in which the amplitude of the forcing, F_0 in equation (4.8), varies from 0.001 to 1, the rms amplitudes in the wave field directly scale with the forcing amplitude as

$$A_\xi \sim F_0^{1.0\pm0.0001}. \tag{4.13}$$

However, the wave field in the Rayleigh damping simulations still responds to a change in forcing amplitude with time, as seen in Fig. 4.7. When $t \approx 8T_{buoy}$

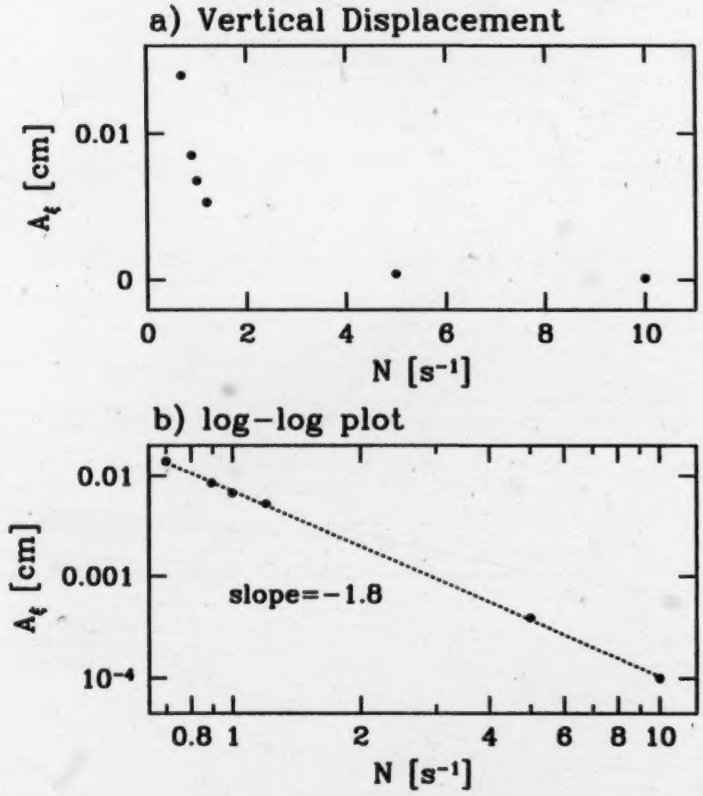

Figure 4.12: a) Variation of A_ξ with N. b) Variation on a logarithmic scale. The slope of the best-fit line is -1.8 ± 0.1.

the energy in the mixed region reaches steady state and the wave excitation amplitude consequently decreases. The range of buoyancy frequencies in the simulations corresponds to buoyancy periods between 0.6 s and 63 s. The most consistent measure of characteristic amplitude for a simulation was to calculate the average amplitude (rms in the horizontal) between two fixed vertical positions, $z = 45$ and 55 cm at a fixed time relative to the buoyancy frequency and before bottom reflection.

Characteristic amplitudes compared at $t = 8T_{buoy}$ as they vary with N are shown in Figure 4.12a together with a logarithmic plot in Fig. 4.12b. The

slope of the best-fit line to the logarithmic plot shows a trend of $A \sim N^{-1.8\pm0.1}$. Over a range of comparisons between choices of amplitude measurements, the results combine to give a power law relation of the form

$$A_\xi \sim N^{-1.9\pm0.4}. \tag{4.14}$$

The magnitude of the exponent is larger than what was observed in the experiments. This probably is due to the unsteadiness of the wave field as it adjusts to steady forcing at $t \approx 8T_{buoy} \approx 50\,\mathrm{s}$. The buoyancy period varies between simulations, and the overall wave properties scale with the buoyancy period, but the forcing establishes steady-state at $t = 50\,\mathrm{s}$ regardless of the strength of the stratification below. This leads to some error in comparison between simulations. Since the short T_{buoy} simulations reflect off of the bottom well before 50 s, comparison between experiments after the point of steady state forcing is impractical. Specifically, to extend the bottom boundary far enough to avoid bottom reflection is too computationally expensive to implement. The simulations with Rayleigh damping were an attempt to achieve steady-state within the mixed region, but the effects of transients were unavoidable.

The perturbation kinetic energy within the mixed region is constant between simulations for the Rayleigh damping case, but the kinetic energy associated with the wave field varies with N. The average perturbation kinetic energy between $z = 45$ and 55 cm at $t = 8T_{buoy}$, normalized by the average value within the mixed region is shown in Figure 4.13. The kinetic energy decreases with an increase in the buoyancy frequency as PKE $\sim N^{-1.5\pm0.1}$ with values between 0.04 and 0.001 percent of the average mixed region value.

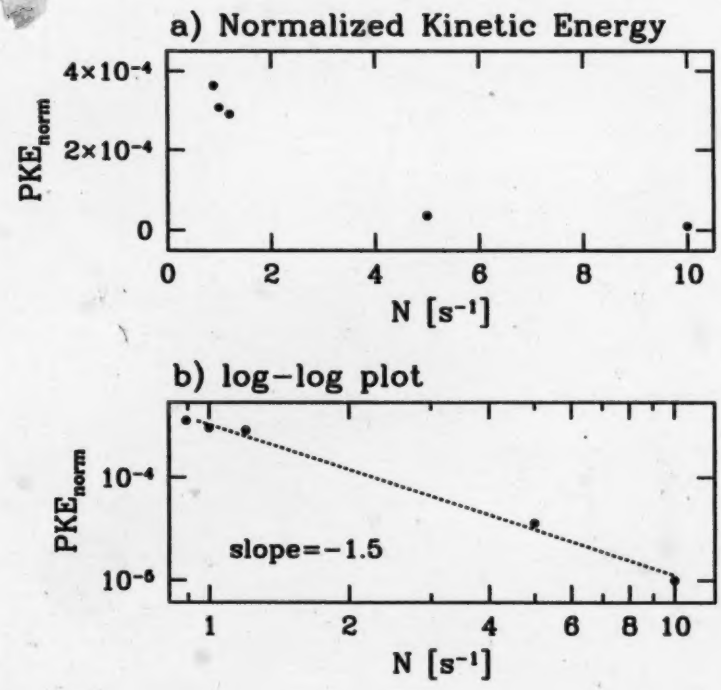

Figure 4.13: Variation of kinetic energy with N. The kinetic energy values are normalized by the average kinetic energy in the mixed region, after reaching steady state.

4.5 Discussion

The spin-up of stationary vortices in a mixed layer has been shown to generate internal waves in an adjacent stratified region. The numerical simulations generate waves having properties consistent with those of the large-scale waves in the laboratory experiments. The waves last for the duration of the investigation, they are of mode 2 in the horizontal, with no simple modal structure in the vertical, and the amplitudes vary inversely with N.

An initial burst of vorticity to a mixed region at the start of the simulations generates waves on the horizontal scale of the vortices, but at all vertical

wavelengths. The longest vertical wavelengths travel downwards the fastest as the wavefield disperses in time. The spin-up time, over which the forced vorticity field reaches steady state, is independent of the buoyancy period and introduces a second time-scale. However, when the time series for the simulations with damping are scaled by the buoyancy period, they have the same qualitative features for the initial wavepackets across the range of buoyancy frequencies examined. This implies that the leading packet of waves that propagate away from the mixed region are generated from the initial impulsive forcing. The long-time behaviour is affected by the subsequent forcing and resulting wave characteristics, such as the amplitude, are determined primarily by the buoyancy frequency.

Due to the horizontal modal structure of the waves, the angle of propagation cannot be determined. If all possible frequencies are generated by the initial impulse, the front of the initial wavepacket would correspond to those waves travelling at the maximum possible group velocity which occurs at $\Theta = 35°$. This implies a horizontal wavelength of 20 cm, based on the observed group velocity. This is half of the total width of the mixed region and equal to the width of a single vortex. Conversely, assuming a horizontal wavelength of 40 cm for the initial wavepacket, this would restrict the frequencies within the wavepacket to a maximum angle of propagation of 12°, an unrealistically small value. Further corroborative evidence for expecting transport to be dominated by single vortex-scale waves is evident in the e-folding depth of the exponential envelope to the initial vertical displacement field. Despite this empirical evidence, an understanding of this subharmonic initial forcing remains unclear.

Chapter 5

Numerical Simulations - Small-Scale Forcing

5.1 Introduction

Two scales of internal waves were observed to be excited by the turbulence in the laboratory. The mean circulations in the laboratory experiments generated tank-scale waves. In addition, smaller-scale downward-propagating waves were generated from the turbulent jets and eddies. In the previous chapter numerical simulations of counter-rotating vortices in a mixed layer generated internal waves on the horizontal scale of the domain. In this chapter we describe a continuation of the numerical simulations in which we simulate the generation of eddy-scale waves by imposing a continually forced random vorticity field in the mixed region.

5.2 Numerical Model

The numerical simulations were performed with the same model as described in section 4.2.1. In the majority of simulations, the domain extends from $-20 \leq x \leq 20\,\mathrm{cm}$, and $0 \leq z \leq 80\,\mathrm{cm}$ with the spatial resolution of $\Delta x = \Delta z = 0.08\,\mathrm{cm}$, and a temporal resolution of $\Delta t = 0.002\,\mathrm{s}$. The mixed region extends from $60 < z \leq 80\,\mathrm{cm}$ and the buoyancy frequency again ranges from $0.1 \leq N \leq 10\,\mathrm{s}^{-1}$.

The spectral components of the vorticity field are randomly forced each time-step at the higher wavenumbers. Two types of forcing are used. In the first, the wavenumbers are continually forced with a Gaussian envelope centered at a peak wavenumber, k_f, and with a spread of k_σ:

$$F_\zeta^*(k_x, k_z) = A_F^* \exp\left[-\frac{1}{2}\left(\frac{(k_x - k_f)^2 + (k_z - k_f)^2}{k_{\sigma^2}}\right)\right] \tag{5.1}$$

where $*$ denotes the spectral component, A_F^* is a random variable with $-F_0 \leq \mathrm{Re}\{A_F^*\}, \mathrm{Im}\{A_F^*\} \leq F_0$, and the amplitude of forcing, F_0, varies between 0.0001 and $1\,\mathrm{s}^{-2}$. Each of the real and imaginary components of F_ζ^* are forced separately at each time step. The forcing wavenumber varies between $k_f = 10\,\mathrm{cm}^{-1}$ and $k_f = 13\,\mathrm{cm}^{-1}$. The width in spectral space varies between $k_\sigma = 2\,\mathrm{cm}^{-1}$ and $k_\sigma = 4\,\mathrm{cm}^{-1}$. This corresponds to forcing at scales less than 1 cm.

In the second type of forcing, the vorticity is simply forced in a box of spectral space such that $6.28 \leq k_f \leq 18.85\,\mathrm{cm}^{-1}$, which corresponds to forcing at scales between 1 cm and 0.3 cm.

In addition to the forcing described above, test simulations were performed

in which the random field was forced with an energy spectrum that would follow a k^{-3} spectrum, as in two-dimensional turbulence. The response of the wavefield to the forcing was found to be independent of the type of forcing used, and only varied with the higher energy associated with forcing at larger wavelengths.

Unlike the large-scale forcing of two counter-rotating vortices, the energy in the mixed region reached a mean steady state within 20 s of the simulation due to balance with viscous (Laplacian) diffusion. There was no need for artificial Rayleigh damping of the mixed region in these simulations.

As with the large-scale vortex forcing simulations, typical runs require on the order of 1000 CPU hours. Running in parallel on many CPUs makes these simulations feasible.

5.3 Observations

5.3.1 Qualitative Features

At the start of a simulation both intermediate-scale waves, on the order of 1 cm, and small-scale waves are generated from the base of the mixed region. Similar to the simulations with counter-rotating vortices, the wave field initially has an exponential decay with depth from the mixed region which includes both propagating and evanescent waves. The wave amplitudes remain several orders of magnitude higher within 1 cm below the mixed region than in the lower portion of the stratified region throughout the duration of the simulations. The large-scale waves are the fastest waves to propagate into the depth of the stratified region, although waves on a range of scales continue to be excited,

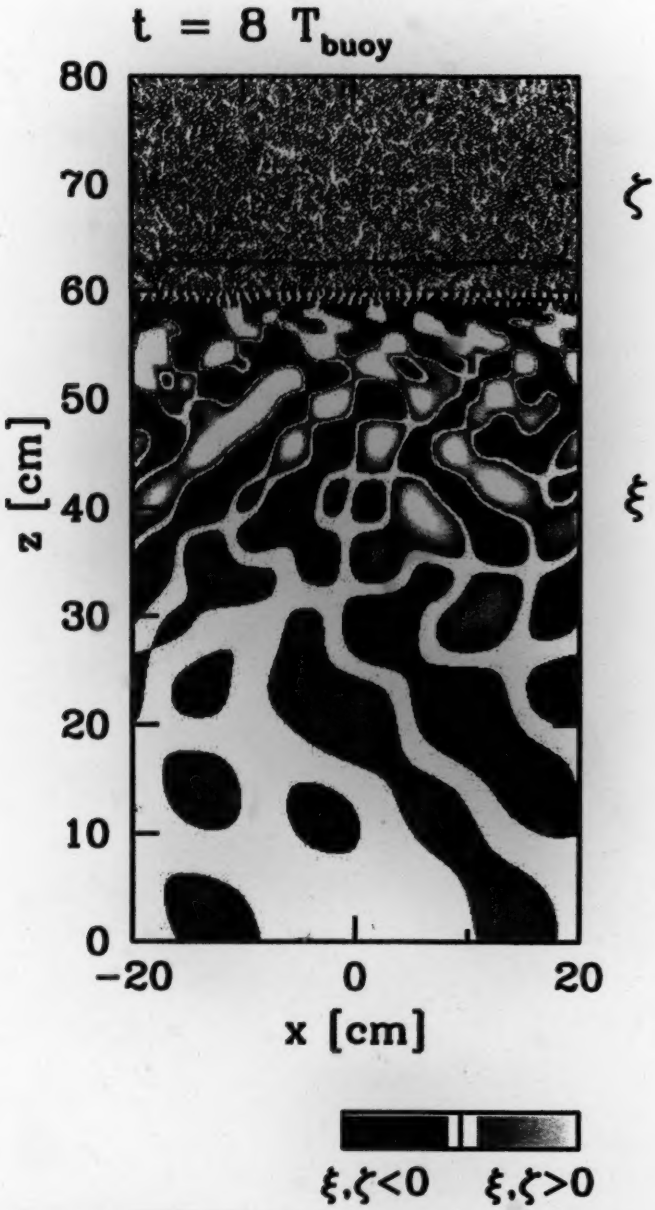

Figure 5.1: Instantaneous wave fields at time = 8 T_{buoy} for a simulation with $N = 1.0\,s^{-1}$ and $-80 \leq z \leq 80$. The vorticity field, ζ, (visible between $60 < z \leq 80$) is superimposed on the vertical displacement field, ξ (visible between $0 < z < 62$). The aspect ratio of length to height for the image is 1:1. Both fields are normalized and the colour map indicates regions of positive and negative fields.

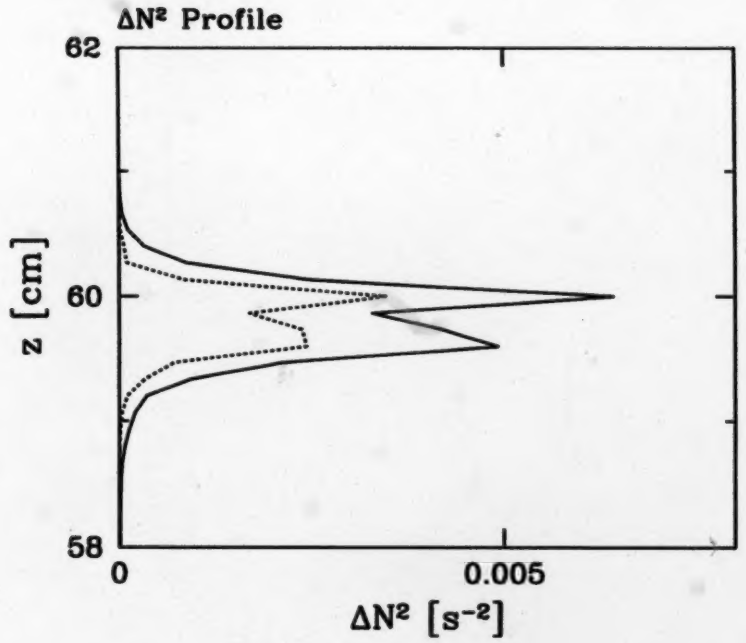

Figure 5.2: Location and structure of the interface between the mixed region and the stratified region. The solid line indicates the change to the background density gradient, ΔN^2, averaged across the horizontal at time $t = 8T_{buoy}$, for a simulation with $N = 1.0\,\mathrm{s}^{-1}$. The dotted line is ΔN^2 at time $t = 1\,\mathrm{s}$.

propagating down through the stratified region.

In Figure 5.1 is a snapshot of the basic state fields for a simulation with $N = 1.0\,\mathrm{s}^{-1}$ at time $t = 8T_{buoy}$ in the simulation. Vertical displacement and vorticity are superimposed in the same frame in order to show the relative length scales in the two regions. The wave field in the simulation shows many of the same properties as in the laboratory experiment. For example, the angle of propagation of the waves is centered around $\Theta = 45°$. As well, wavelengths in the intermediate range between the largest scales in the tank, $L = 40\,\mathrm{cm}$, and the smallest forced scales in the mixed region, $L < 1\,\mathrm{mm}$, are excited.

An interfacial layer immediately develops between the mixed region and the

stratified region. In Figure 5.2 is the ΔN^2 field averaged across the horizontal at times $t = 1\,\mathrm{s}$ and $8T_{buoy}$. The layer is approximately 1 cm thick, with larger gradients in density at the top and bottom of the layer. The amplitude of the displacement field within the first centimeter below the mixed region and within the base of this interfacial layer is large enough to be beyond the scale of the colour map in Fig 5.1. It is from the base of this layer that propagating waves (with frequencies less than the buoyancy frequency) are excited.

A vertical time series of the displacement field for the simulation in Fig. 5.1 is shown in Figure 5.3. The time series is taken for 16 buoyancy periods beginning when the vorticity is first forced. The regular structure to the wave field is the most noticeable feature of this time series. At the start of the simulation, a regular train of waves is generated, reminiscent of the waves generated by the initial impulse in the simulations with the counter-rotating vortices. The diagonal line in the figure is the calculated group velocity for waves with a length scale of 40 cm (the largest horizontal scale) and an angle of propagation of 45° (the observed angle of propagation). These waves are likely a response to the initial impulsive forcing. The wave field at later times, in the upper right-hand corner of Fig. 5.3, does not have the same regularity as produced by these initial waves. The analysis of the wave properties in the sections that follow will focus on these latter waves.

In the series of simulations with buoyancy frequency ranging across $N = 0.1 \ldots 10.0\,\mathrm{s}^{-1}$ the time series all exhibited the same general behaviour as in Fig. 5.3, once scaled in time with the buoyancy period. The transient waves travel at the same vertical group velocity and with the same period.

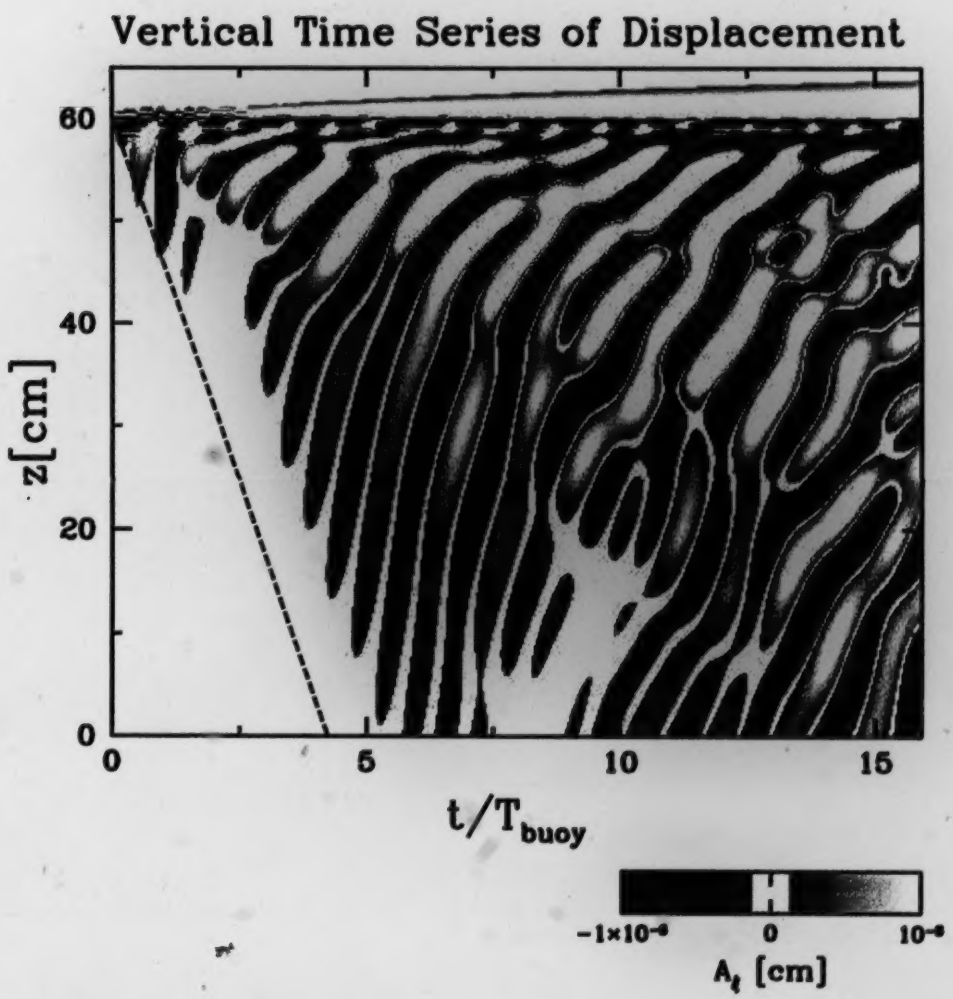

Figure 5.3: a) A sample false-colour vertical time series image for the simulation in Fig. 5.1 with $N = 1.0\,\mathrm{s}^{-1}$ and $-80 \leq z \leq 80\,\mathrm{cm}$. The horizontal location of the time series is at $x = -5.0\,\mathrm{cm}$. The time series is scaled with the buoyancy period. The diagonal line indicates the vertical group velocity for waves with an angle of propagation of 45° and a horizontal wavelength of 40 cm, the width of the total domain.

5.3.2 Length Scales

The length scales of the waves increase with distance from the mixed region.

As the simulation progresses and the wave field develops beyond the initial

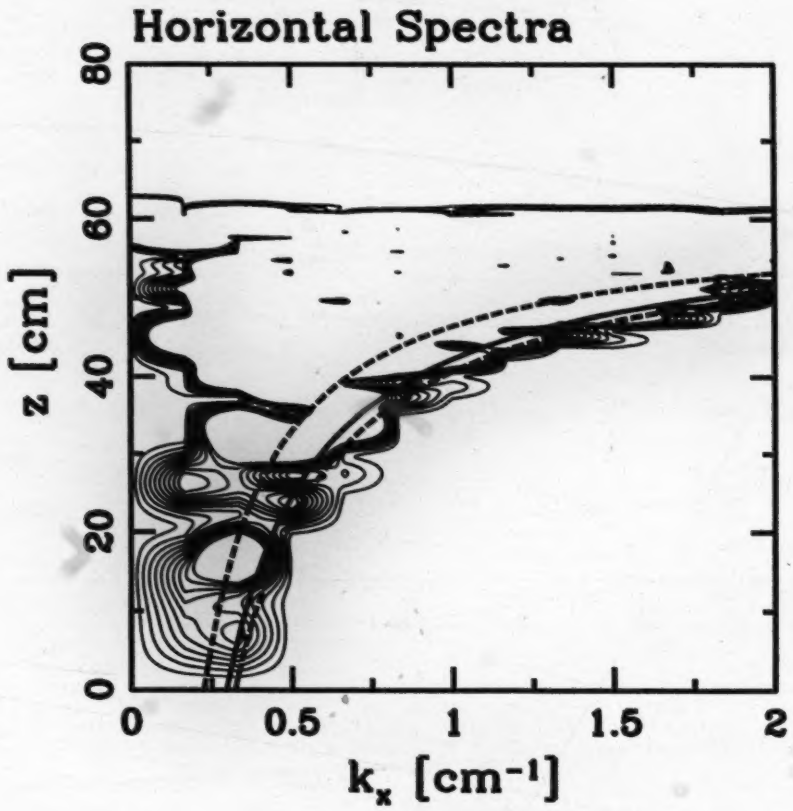

Figure 5.4: The vertical profile of horizontal wavenumbers, calculated from the vertical displacement field in Fig. 5.1. The solid line is the maximum vertical excursion at time $8T_{buoy}$ for waves with horizontal wavenumber k_x travelling at $\Theta = 45°$. The dashed lines to the right and left are the maximum excursions for waves travelling at $\Theta = 35°$ and $\Theta = 55°$ to the vertical, respectively. The contour interval for the squared Fourier amplitudes is $2 \times 10^{-14}\,\mathrm{cm}^3$. The contours are plotted to $2 \times 10^{-13}\,\mathrm{cm}^3$, although the maximum value is $2.4 \times 10^{-6}\,\mathrm{cm}^3$.

stage, the small-scale waves propagate deeper into the stratified region. In Figure 5.4 is a vertical profile of the horizontal wavenumbers determined from the vertical displacement fields. The figure shows the spectrum of horizontal wavenumbers at 8 buoyancy periods into the simulation. The contour interval

is small and shown only for small values in order to highlight the edges of the spectrum. The spectrum shows the decrease of small wavelength waves with distance from the mixed region. The figure also shows the broad spectrum of wavelengths within the interface between $z = 59$ and 60 cm.

The vertical group velocity for linear internal waves is given by

$$c_{gz} = \frac{N k_x k_z}{(k_x^2 + k_z^2)^{\frac{3}{2}}}, \tag{5.2}$$

where k_x is the horizontal wavenumber and k_z is the vertical wavenumber. For waves travelling at 45°, $k_x = -k_z$ the corresponding vertical depth for a wave with wavenumber k_x at time t is

$$z = c_{gz} t = 2^{-\frac{3}{2}} \frac{N}{k_x} t. \tag{5.3}$$

This curve is included in Fig 5.4 as the solid line, along with dashed lines for waves with angles of propagation of 35° (right) and 55°(left). The length scales of the wave field are shown to be determined by the propagation speed of the waves, and no preferred length scales are excited.

The evolution of the length scales over time is shown in the series of plots in Figure 5.5a-d. The wavelengths fill the possible area, until perhaps $16 T_{buoy}$, when the smallest wavelengths do not appear as strongly in the spectrum.

Increasing the horizontal domain in the simulations results in the initial appearance of larger scales and larger amplitudes. However, after the initial transient waves have propagated outside of the field of view, the wave field has the same structure as dictated by the relation (5.3). Simulations in which the domain is either doubled or quadrupled do show different transient behaviour

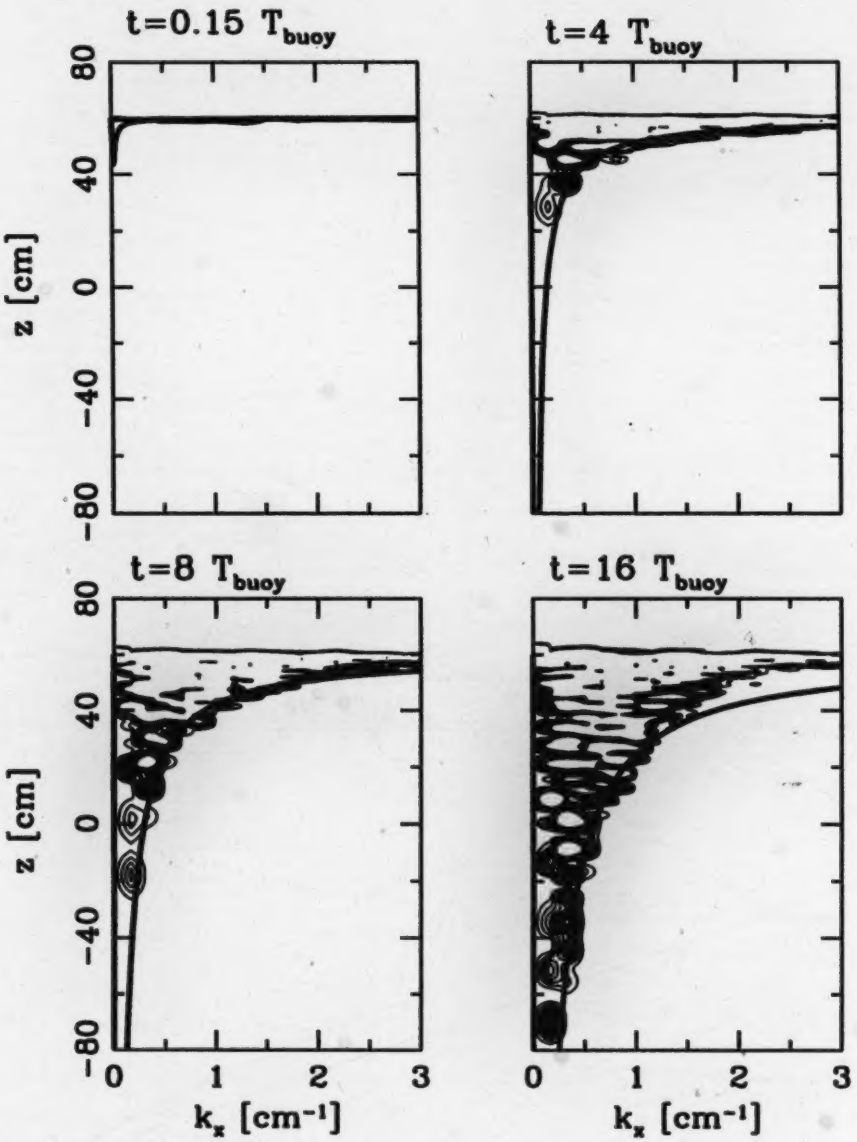

Figure 5.5: Vertical Profiles of horizontal wavenumber, k_x, at $t = 0.16, 4, 8,$ and $16T_{buoy}$ for the simulation in Fig. 5.1. The maximum vertical excursion at each time of waves with horizontal wavenumber k_x travelling at $\Theta = 45°$ are included in all plots. The contour range for all plots is the same as in Fig. 5.4.

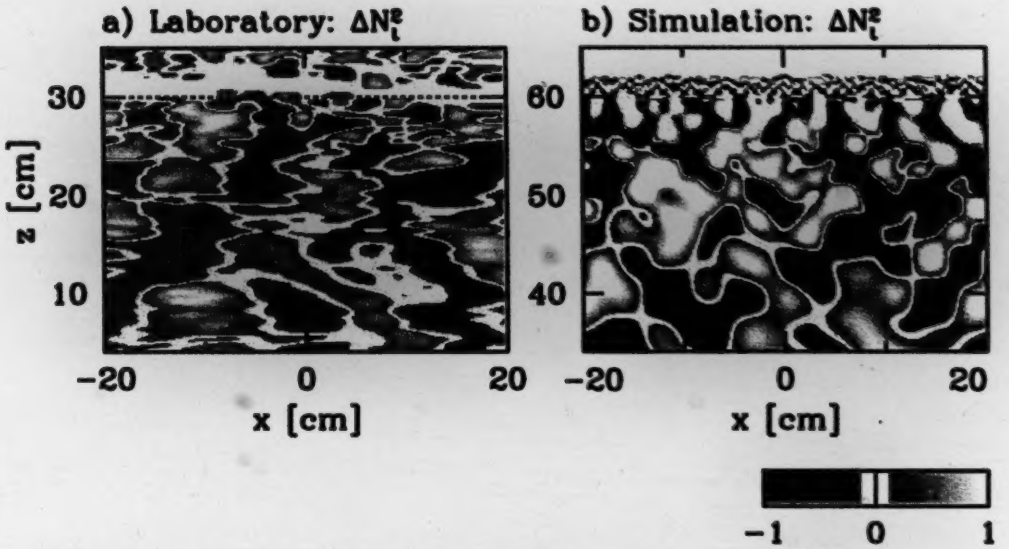

Figure 5.6: Comparison of internal wave fields at time = 10 T_{buoy} for a laboratory experiment and a simulation. a) The schlieren field, $\partial(\Delta N^2)/\partial t$, for a laboratory experiment in which $N = 1.06\,\mathrm{s}^{-1}$. The mixed region is marked by the horizontal dashed line. b) Schlieren field computed from a numerical simulation in which $N = 1.0\,\mathrm{s}^{-1}$ and a density jump is added from $59 < z \leq 60\,\mathrm{cm}$ to match the laboratory conditions. The field of view corresponds to a). The aspect ratio of length to height is 1:1 in both panels. Both fields are normalized. The colour map indicates regions of positive and negative fields.

and have larger amplitude waves. However, the long-term behaviour is unaffected by the domain size and snapshots at $t = 8T_{buoy}$ have a similar structure in all cases.

5.3.3 Comparison with Laboratory Experiments

In order to compare directly the qualitative features of the simulations with the laboratory experiments, a sample experimental wave field is shown in Figure 5.6a along with a corresponding numerical simulation. In this experiment, $N = 1.06\,\mathrm{s}^{-1}$. The field is shown ten buoyancy periods into the experiment at

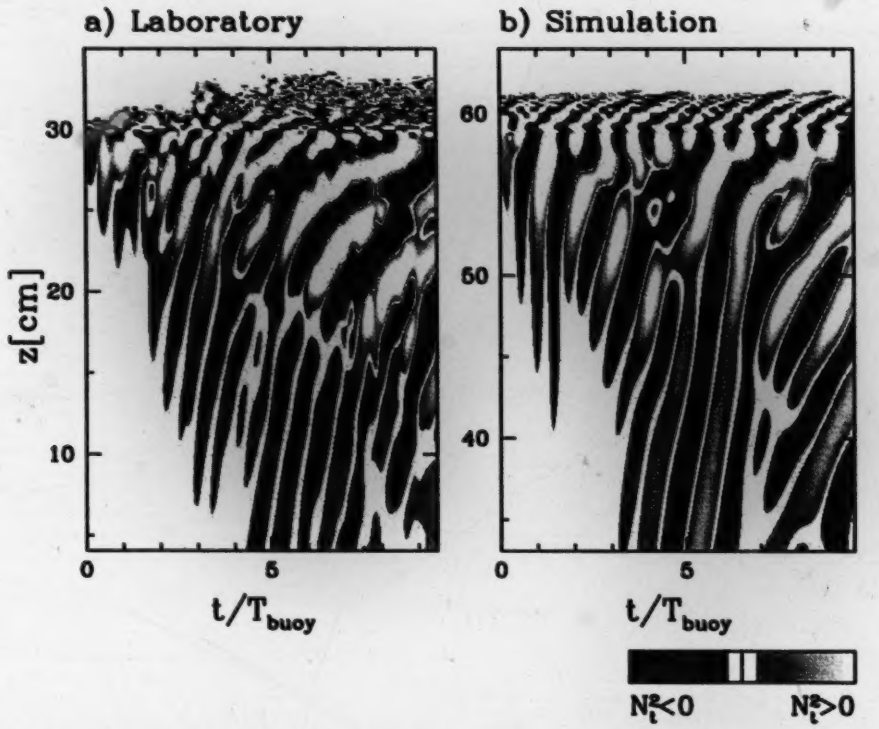

Figure 5.7: Vertical time series of the N_t^2 fields corresponding to a) the laboratory experiment in Fig. 5.6 and b) the numerical simulation. In the experimental situation, the mixed region deepened from $z = 47\,\mathrm{cm}$ to $z = 35\,\mathrm{cm}$ within the first 10 seconds and then to $z = 30\,\mathrm{cm}$ within the time frame of image. The colour scale is arbitrary and indicates regions of positive and negative fields.

which time the mixed region has deepened to $z = 30\,\mathrm{cm}$. The field shown is the field directly measured by the synthetic schlieren technique. In Fig. 5.6b is the schlieren field for a simulation in which $N = 1.0\,\mathrm{s}^{-1}$. The field of view shown has the same dimensions as in Fig. 5.6a and is also taken at $t = 10T_{buoy}$.

Vertical time series of the schlieren fields for the experiment and the simulation in Fig. 5.6 are shown in Figure 5.7. The time series are taken for 10 buoyancy periods and begin when the oscillating grid is turned on and when

the vorticity is first forced, respectively. The same frequencies and the same length scales are present in both figures despite the very different forcings to the mixed region and despite the two-dimensionality of the simulations.

5.3.4 Effect of the Interface

The excitation of waves from the mixed region occurs across the interface between the mixed region and the stratified region. The snapshot image shows the complexity of the wave field within the interface. The vertical profiles of horizontal wavenumbers show that all possible wavelengths are generated within this region. In the experiments, a density step existed between the mixed region and the top of the main stratified region. For example, see Fig. 3.1a. The density step was created during the establishment of the mixed layer by mixing the initially uniformly stratified tank. Complementary experiments with no density step showed no qualitative differences for the wave field in the main stratified region.

Figure 5.8 compares two simulations, both with $N = 1.0\,\mathrm{s}^{-1}$ but one with and one without a density step underneath the mixed region. Specifically, the right panels show simulations having a density step simulated by enhanced buoyancy frequency $N = 3.0\,\mathrm{s}^{-1}$ between $59 < z \leq 60$. This approximately reproduces the conditions of the experiments described in Chapter 3.

In Figs. 5.8a and c are time series for the simulations. The time series in c shows that the initial transient wave field has a less regular structure than in a. The response to the initial impulsive forcing is possibly modified by the pre-existing thick interface. Comparison of the frequency spectra (not shown) of the fully developed wave fields yields no significant difference in frequencies

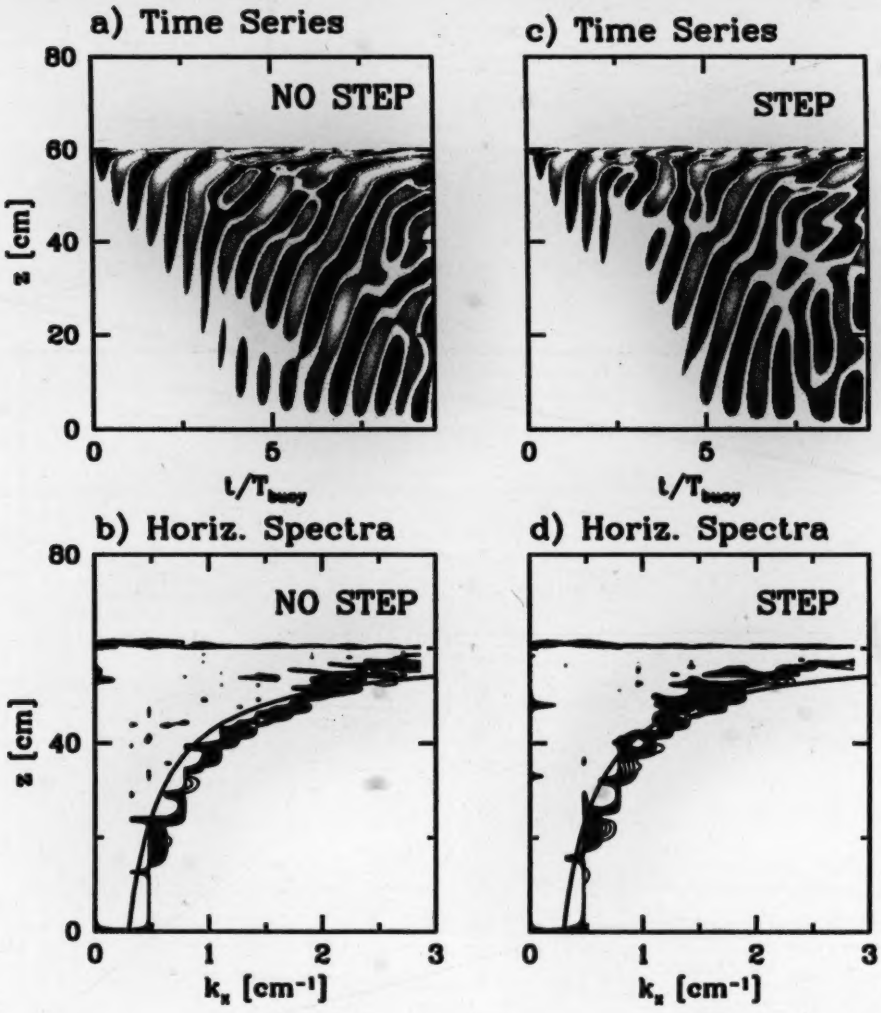

Figure 5.8: The effect of adding a density step. In a) and b) are the vertical displacement time series and horizontal spectra at $t = 8T_{buoy}$ of a simulation with no imposed density step between the mixed layer and the stratified region. In c) and d) are the corresponding plots for a simulation with an added density jump between $59 < z \leq 60$. The density jump is simulated by locally increasing N^2 from $1.0\,\mathrm{s}^{-1}$ to $3.0\,\mathrm{s}^{-1}$. The colour map for a) and c) follows Fig. 5.3 with $|A_\xi| < 8 \times 10^{-5}\,\mathrm{cm}$. The contours for the squared Fourier amplitudes in b) and d) are plotted to $2 \times 10^{-11}\,\mathrm{cm}^3$ by $1 \times 10^{-12}\,\mathrm{cm}^3$.

of the generated waves well below the mixed region. The vertical profiles of horizontal wavenumbers are shown in Figs. 5.8b and d. The profiles are similar although the small wavelengths just below the mixed region contain less energy

in the imposed density step simulation.

This comparison suggests that the interface between the mixed region and the stratified region acts as a partial filter for the evanescent waves and as a conduit through which the random white noise forcing in the mixing region connects to the regular internal waves below.

5.4 Results

5.4.1 Wave Amplitudes

The vertical displacement field in Fig. 5.1 shows highly elevated wave amplitudes at the base of the mixed region, the amplitude decreasing with distance from the source. Plotted in Figure 5.9a is a profile of root-mean-square vertical displacement amplitude averaged first in time across a time series from $t = 20 \ldots 60\,\mathrm{s}$ and second in space for time series at 39 horizontal positions across the simulation. The standard deviation of the averaging process is included as the dashed lines. The profile is shown only for a limited vertical range near the interfacial layer. The amplitudes again decrease at the top of the profile (in the middle of the interfacial layer) and correspond to the decrease in the ΔN^2 field of Fig. 5.2.

In Fig. 5.9b is the same profile on a logarithmic scale. The horizontal dotted line in both plots indicates $z = 58\,\mathrm{cm}$. The wave amplitudes exhibit two regimes, one within the interfacial region and one in the uniformly stratified region. There is a sharp decay in amplitude below the interfacial region. The decay from source does not seem to follow a single exponential decay, as expected for evanescent waves.

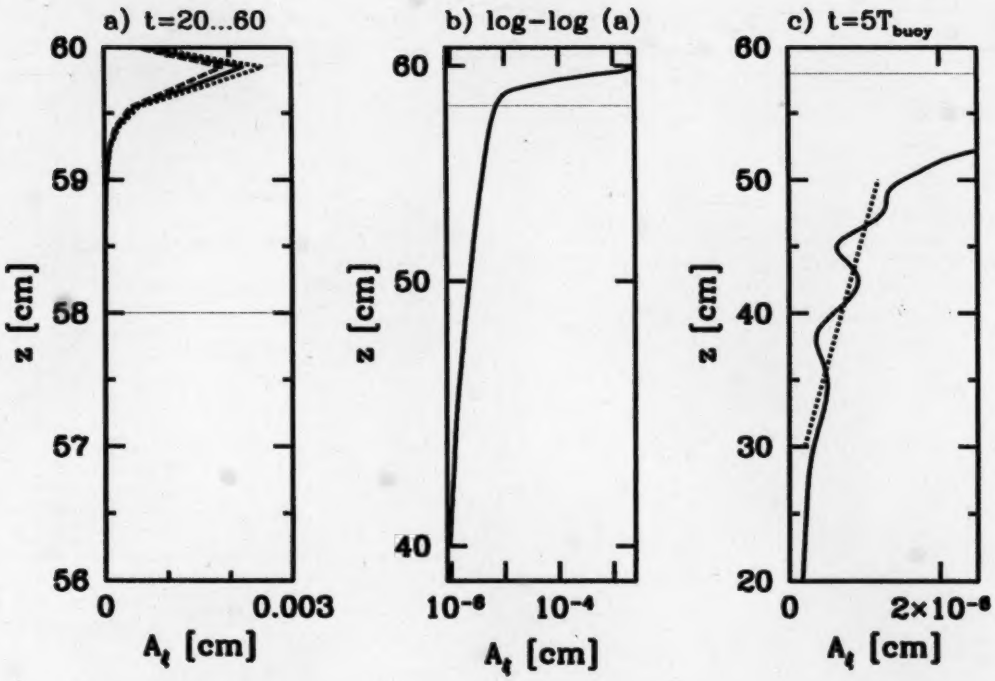

Figure 5.9: In a) is the horizontally and temporally averaged vertical displacement amplitude, A_ξ, across $20 \leq t \leq 60\,\mathrm{s}$ as a function of z for a simulation with $N = 1.0\,\mathrm{s}^{-1}$. The vertical range is chosen to emphasize the interfacial region near $z = 59\,\mathrm{cm}$. In b) is the amplitude on a logarithmic scale. The change in wave amplitude regimes between the interfacial region and the stratified region is marked by the horizontal dotted line at $z = 58\,\mathrm{cm}$. In c) is the r.m.s. averaged vertical displacement amplitude for a single displacement field at $t = 5T_{buoy}$. The best-fit-line through the profile between $30 \leq z \leq 50$ is used as a measure of characteristic amplitude for a simulation.

In order to define a single characteristic value for the amplitude in the wave field as it depends on the stratification, it is necessary to avoid both the interfacial region and the possible dependence on time. An amplitude value is calculated from the vertical profile of the horizontally rms averaged displacement field at $t = 5T_{buoy}$. The amplitude value at $z = 50$ based on the best-fit line through $z = 30 \ldots 50\,\mathrm{cm}$ is used as the characteristic amplitude for each simulation. The amplitude profile and best-fit line is provided in

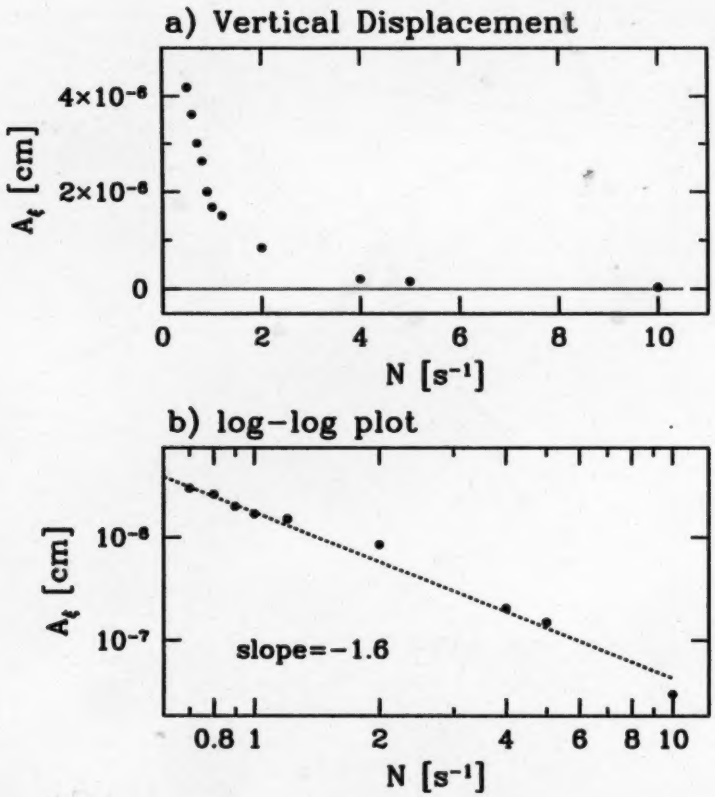

Figure 5.10: a) Characteristic vertical displacement amplitudes as a function of the buoyancy frequency. b) Amplitude variation on a logarithmic scale. The slope of the best-fit line is -1.6 ± 0.1.

Fig. 5.9c.

In Figure 5.10a are the results of the amplitude measurements across the range of simulations, plotted as a function of the buoyancy frequency. As in the laboratory experiments, as well as the counter-rotating vortices, the wave amplitude decreases with an increase in buoyancy frequency. The results are plotted on a logarithmic scale in Fig. 5.10b. The slope of the best-fit line

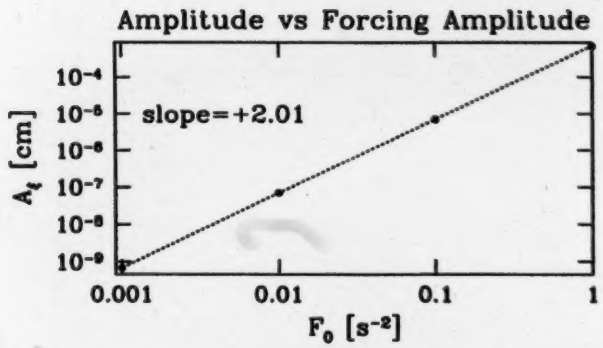

Figure 5.11: Variation of wave amplitude with amplitude of forcing, F_0, to the mixed region. The wave amplitude varies as a function of the square of the forcing amplitude, with the slope to the best-fit line of 2.01 ± 0.002.

through the data shows a dependence of

$$A_\xi \sim N^{-1.6\pm0.1}. \tag{5.4}$$

The variation of wave amplitude does not follow a direct relation to the forcing amplitude, F_0, as was the case for the large-scale forcing. Rather, as seen in Figure 5.11, the wave amplitude depends on the square of the forcing amplitude:

$$A_\xi \sim F_0^{2.01\pm0.002}. \tag{5.5}$$

This nonlinear relationship is unexpected and illustrates the nontrivial transfer of energy from the mixed region to the wavefield. The complexity of the energy transfer between regions was previously seen in the disparity of amplitude magnitudes between the interfacial region and the interior of the stratified region.

As in the simulations with counter-rotating vortices, the kinetic energy

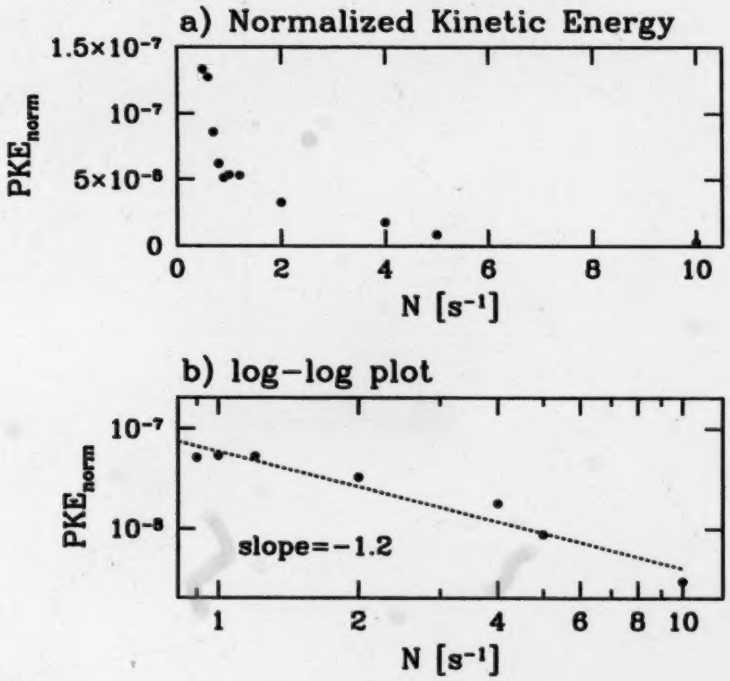

Figure 5.12: Variation of kinetic energy with N. The kinetic energy values are normalized by the average kinetic energy in the mixed region. The values are measured at $t = 8T_{buoy}$.

associated with the wave field again varies with N. In Figure 5.12 is the average perturbation kinetic energy between $z = 45$ and 55 cm at $t = 8T_{buoy}$ again normalized by the average value within the mixed region. The kinetic energy decreases with an increase in the buoyancy frequency as PKE $\sim N^{-1.2\pm0.1}$. The values are a much lower percentage of the values within the mixed region, between 3×10^{-7} and 1×10^{-5}%.

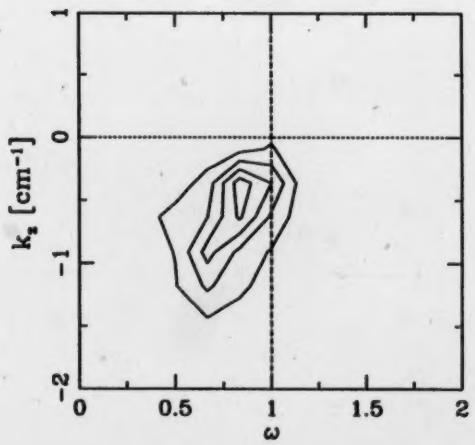

Figure 5.13: Power spectrum of the time series for the numerical simulation in Fig 5.3. The largest peak corresponds to downward-propagating internal waves with angles of propagation of $\Theta = 41°$. The maximum frequency for internal waves is marked by the vertical line at $\omega = N = 1.0\,\mathrm{s}^{-1}$. The maximum value is 7.3×10^{-14} cm^{3}s with contours every 1.5×10^{-14}.

5.4.2 Frequencies

In this set of simulations the forcing to the mixed region is random white noise with an equal partition of forcing amongst all resolvable frequencies. The regularity of the time series in Fig. 5.3 and the visual dominance of internal waves with angles of propagation around 45° in Fig. 5.1 indicate a narrow response in frequency space of the wave field to the random forcing. Following the averaging techniques used to analyze the laboratory data, power spectra of time series are calculated at 39 positions across the horizontal domain and averaged. Figure 5.13 is the result of the averaged power spectra for a simulation with $N = 1.0\,\mathrm{s}^{-1}$. The Fourier transform is calculated in a window from $t = 20 \ldots 60\,\mathrm{s}$ and $z = 25 \ldots 50\,\mathrm{cm}$ in order to avoid the interface region and

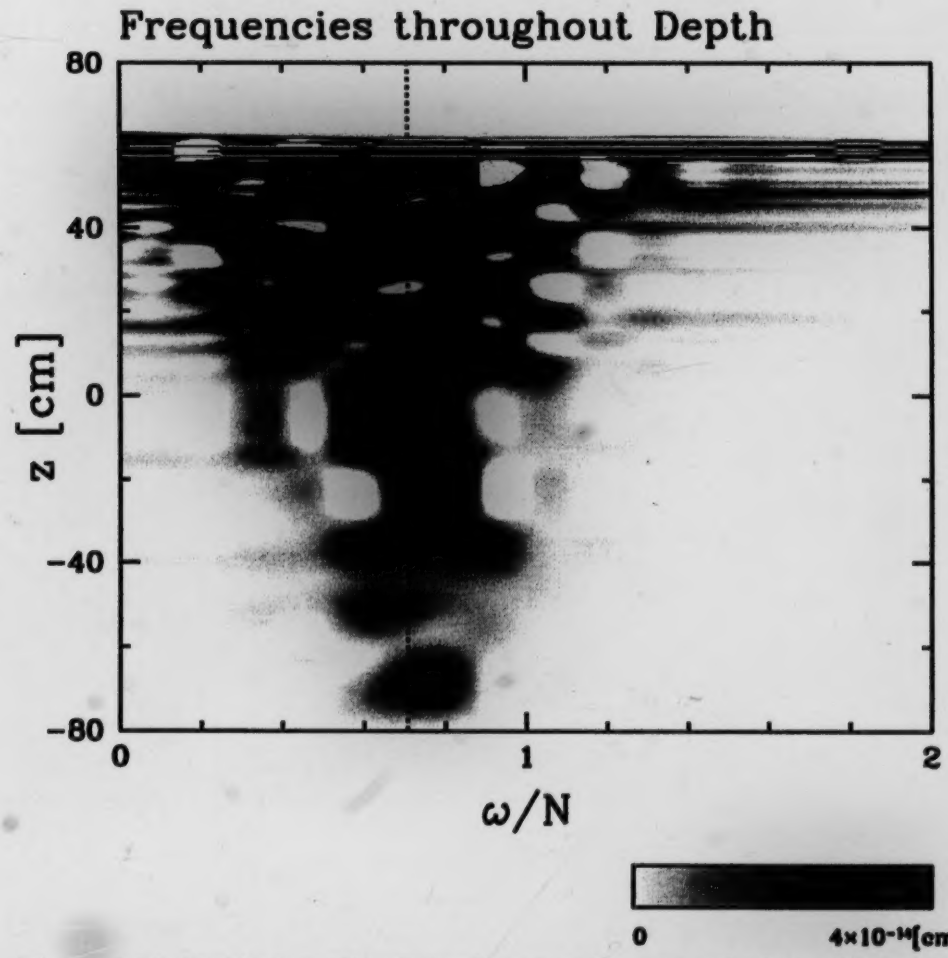

Figure 5.14: Vertical profile of the frequency spectra calculated from a time series from t=$8-16T_{buoy}$ for a deep simulation with $N = 1.0\,\mathrm{s}^{-1}$. The vertical dotted line corresponds to angle of wave propagation of $\Theta = 45°$. Pure black regions indicate squared Fourier amplitudes greater than $4 \times 10^{-14}\,\mathrm{cm}^3$ to a maximum value of $5 \times 10^{-6}\,\mathrm{cm}^3$.

the transient waves. The spectrum is typical of the spectra across the range of buoyancy frequencies. The frequencies of the waves are concentrated around a frequency corresponding to an angle of propagation of $\Theta = 45°$.

In Figure 5.14 is a profile of the frequencies present as a function of depth calculated from a single time series of the deep domain simulation for which

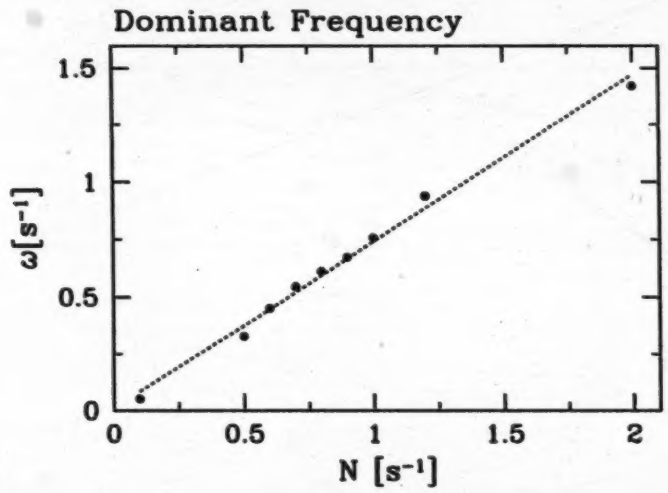

Figure 5.15: Dominant wave frequencies as a function of the buoyancy frequency. The best-fit line through the data gives a characteristic angle of wave propagation for the range of simulations of $\Theta = 43 \pm 2°$.

$N = 1.0\,\mathrm{s}^{-1}$. The duration of the time series is from $t = 8T_{buoy}$ to $16T_{buoy}$. Included in the image is a vertical dashed line indicating the frequency corresponding to $\Theta = 45°$. All frequencies are present within the interface from $z = 59 \ldots 60\,\mathrm{cm}$, seen as the band across the field of view at the top of the stratified region. There is a broader spectrum of frequencies closer to the mixed region centered around the dashed line with a clear narrowing of the spectrum further away from the mixed region.

Characteristic frequencies for simulations with a range of buoyancy frequencies are again calculated based on the spectra in Fig. 5.3. The spectra are averaged across all wavenumbers and smoothed, with the peak taken as the characteristic frequency for the simulation. There is a linear dependence of dominant wave frequency with the buoyancy frequency, as seen in Figure 5.15. Based on the slope of the best-fit line, $\omega = 0.73N$, hence $\Theta = 43°$.

A comparison between the frequency spectra across simulations with buoy-

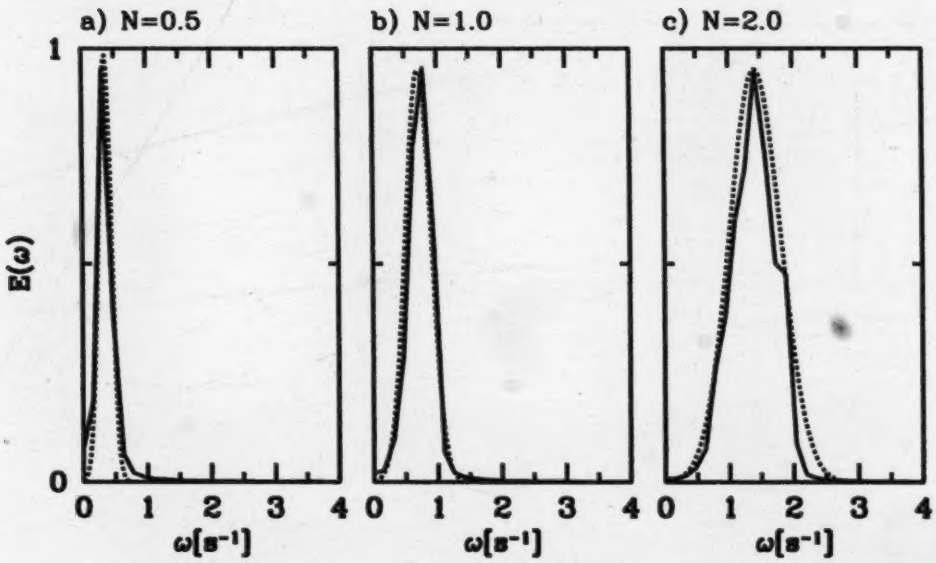

Figure 5.16: The measured normalized frequency spectra for three simulations with $N = 0.5, 1.0$ and $2.0\,\mathrm{s}^{-1}$ are plotted as the solid lines. The universal spectra, defined in equation (5.6) and normalized by $A_E N^{-3/2}$, are plotted as the dotted lines.

ancy frequencies spanning two decades shows a more complex dependence of frequency with N. As N increases, the range of possible internal wave frequencies increases. The peak of the spectra follows $\omega = 0.7N$, but the spread in frequency space also scales directly with N. The amplitudes of the waves decrease away from the peak frequency following approximately a Gaussian form. A universal description of the dependence of the spectrum of internal waves on the buoyancy frequency is empirically given by

$$E(\tilde{\omega}) = A_E N^{-3/2} \exp\left[-\frac{(\tilde{\omega} - \tilde{\omega_0})^2}{2\sigma_\omega^2}\right] \tag{5.6}$$

with $\tilde{\omega} = \omega/N, \tilde{\omega_0} = \cos(45°), \sigma_\omega = 0.2$, and $A_E = 8 \times 10^{-16}\,\mathrm{cm^2 s^{-1/2}}$.

The measured frequency spectra prior to the smoothing operation for three

simulations with $N = 0.5, 1.0$ and 2.0, are plotted in Figure 5.16 along with the corresponding universal spectra. The spectra are normalized by their amplitudes, but plotted on the same frequency scale to highlight the scaling with N. The universal spectrum closely matches the spectrum of waves generated in the simulations.

5.5 Discussion

The wave field generated by random forcing to the vorticity field in a mixed layer overlying a stratified region is not itself random. The most regular property of the wave field is the angle of propagation of the waves, which has a clear peak as in the laboratory experiments with an average angle of $\Theta = 43° \pm 4°$. The wave frequency spectrum adjusts to the range of available propagating wave frequencies (such that $\omega < N$), with a spread in frequency space of approximately $0.2N$ about the mean value of $\omega = 0.707N$.

The amplitudes of the waves vary inversely with N with a consistent trend apparent in numerics and experiments. The amplitudes have a nonlinear dependence on the forcing amplitude, varying as the square of the forcing. This is in contrast to the large-scale forcing simulations discussed in Chapter 4 where the response amplitude varies directly with forcing amplitude.

The random forcing does not impose a length scale. And, as a consequence, all possible vertical wavelengths are present in the simulations. The vertical group velocity of the waves depends on the inverse of the horizontal wavelength, so that the scales of waves seen throughout the domain depends on the time of viewing. As with the counter-rotating vortices, the first set of waves seem to be generated as a response to the impulsive start to the simulation.

The transfer of energy between the mixed layer and the internal waves occurs through the 1 cm thick interfacial layer between the two regions. In the experiments of Perera, Fernando and Boyer(1994) a significant amount of wave energy was trapped within the thin interface between the turbulent region and the stratified region beneath. In our simulations, the frequency and wavenumber spectra show a separation between the interface and the lower stratified region, with the presence of much higher frequencies and wavenumbers in the interface. The wave amplitudes are several orders of magnitudes higher within this region and there is a transition between two regimes of amplitude decay from the mixed layer, without a simple exponential decay from source as expected for evanescent waves. Comparison between simulations with and without an imposed 1 cm thick density jump at the base show a small decrease in higher wavenumbers in the stratified region when a thicker interface is present. As well, the waves generated from the initial impulse of forcing are less regular in the density step case. The interface therefore acts as a filter for the smallest length and time scales, and bridges the separation in scales between the random high-wavenumber vorticity field and the regular internal wave field.

Chapter 6

Discussion

Although a range of frequencies may potentially be excited by turbulence, the spectra of the generated internal wave field exhibit a limited frequency range. The dominant frequencies depend on the strength of stratification. However, the angle of propagation of the dominant waves occurs in a narrow range across all experiments and simulations.

There are two possible explanations: instability and resonance. To demonstrate the former, the line labelled "SA" in Fig. 3.14 is the line of maximum relative amplitude of the waves for each angle before they become unstable due to self-acceleration. Waves with angles of 45° can have the largest relative amplitudes before becoming unstable. Because the observed amplitudes of the waves in the laboratory are approximately 25 percent of that required for breaking, this explanation seems unlikely. In addition, the wave amplitudes in the numerical simulations are necessarily kept very small due to numerical stability. Nonetheless, the angles in the simulations are consistently observed to be $\approx 45°$.

It is more likely that the waves are excited through resonant feedback

with the turbulence. For example, consider the vertical flux of horizontal momentum, given by the Reynolds stress $\rho_0\langle uw\rangle$ (where the angled brackets denote averaging over one period), which can be written for small-amplitude waves in terms of A_ξ by

$$\rho_0\langle uw\rangle = \frac{1}{4}\rho_0 N^2 A_\xi^2 \sin(2\Theta). \tag{6.1}$$

The maximum transport by internal waves occurs when $\Theta = 45°$. Likewise, the vertical energy flux per unit horizontal area carried by waves of amplitude A_ξ can be expressed by

$$F_z = \frac{1}{2}\frac{\rho_0 A_\xi^2 N^3}{k_x}\sin\Theta\cos^2\Theta. \tag{6.2}$$

If the horizontal scale of the waves is fixed in addition to the amplitude, the maximum vertical flux of energy by the waves occurs for waves propagating with the maximum vertical group velocity, that is, for waves with $\Theta = 35°$. Since waves transport energy and momentum away from the turbulent region, waves with Θ in the range $35° - 45°$ may act most efficiently to modify the turbulence in a way that enhances their excitation.

The observation of a narrow frequency spectrum of internal waves generated by turbulence has often been observed, though not quantitatively examined. For example, in the experiments of Linden (1975) the internal waves typically propagated at an angle $\Theta \simeq 35°$ to the vertical.

For a given horizontal wavelength, waves with an angle of propagation of $\Theta = 35°$ travel with the fastest group velocity, in which case those waves would be the first observed. This cannot explain the narrow range of angles

of propagation present in both simulations and laboratory experiments. The group velocity curves in the horizontal spectra in Figs. 5.4 and 5.5 show that a range of angles of propagation have sufficient time to travel into the field of view of the simulations. In particular, the difference in vertical group velocities between $\Theta = 35°$ and $\Theta = 45°$ is negligible. Rather, the dominant wave frequencies correspond to those that carry the most horizontal momentum away from the turbulent region. This suggests that there is an interaction between the wave field and the turbulent mixed region, which excites waves within a narrow frequency band.

The amplitudes of the large- and small-scale internal waves are observed to scale with buoyancy frequency as $A_\xi \sim N^{-p}$ with $p = 1.5 \pm 0.1$ for both the laboratory experiments and the numerical simulations that account for transient growth. This power law scaling can largely be explained if we assume that the vertical energy flux, given by (6.2), is constant across the range of experiments in which only the stratification is varied. In this case $A_\xi \sim N^{-3/2}$. Since energy is supplied to the waves by the turbulence, this is a reasonable assumption if the dynamics of the turbulent region are unaffected by the strength of the stratification in the fluid beneath.

Chapter 7

Conclusions

The numerical simulations in two-dimensions have the same qualitative results as the experiments for both of the cases of the large-scale turbulent forcing and the small-scale turbulent forcing. Large-scale, dominantly mode 2 waves are continuously generated by the mean circulation in the mixed region and random forcing across a range of scales excites downward propagating waves with the same length-scales and frequencies. A large part of the dynamics of the generation of waves from the mixed region is captured by the simulations and suggests that a simplified model can be developed to describe the interaction between internal waves and a turbulent mixed region.

The large-scale vortices may be a potential source of internal waves from the surface mixed layer of the ocean and lakes. Langmuir circulations [Craik and Leibovich 1976] are wind-driven flows that are characterized by counter-rotating cells in the surface mixed region of lakes and the ocean. Though Langmuir cells also exhibit shear along the length of the cells, these circulation cells can span the depth of the mixed layer and border the underlying stratified thermocline. Thus, the existence of large amplitude internal waves

generated from counter-rotating cells embedded in a turbulent layer in our experiments illustrates a potential new mechanism for internal wave generation in the surface mixed region of the ocean.

The mixed region is kept turbulent in the laboratory experiments by an oscillating grid, which provides approximately horizontally homogeneous three-dimensional turbulence. The simulations are in two-dimensions and the mixed region is forced by white noise at high wavenumbers in the vorticity field. The comparisons between the laboratory experiments and the numerical simulations are encouraging despite these differences and help validate the assumption of two-dimensionality in analyzing waves in the experimental data.

The ratio of frequency to buoyancy frequency of the dominant downward propagating waves consistently falls within a narrow band in both laboratory experiments and in numerical simulations under a variety of conditions. The frequency bands scale with the buoyancy frequency in a universal spectrum centered around an angle of propagation of 45°. This narrow frequency range corresponds to waves with the maximum vertical transport of horizontal momentum and appears to be a result of a wave-turbulence interaction.

Either creating a turbulent mixed region in the laboratory with an oscillating grid or randomly forcing a mixed region in numerical simulations of two dimensions results in the generation of internal waves in an underlying uniformly stratified region. The nature of the random forcing to the mixed region is not the governing factor to the response of the stratified region.

There is no preferred length scale to the waves generated by the random forcing, and the results scale in time with the buoyancy period. However, the dependence of wave amplitude on either the forcing amplitude or the buoyancy frequency and the preferred angle of propagation of the waves does not follow

any direct scaling with forcing parameters. Observations suggest that it is the interface between the mixed region and the stratified region which filters the highest wavenumbers and frequencies and dynamically connects the turbulence and internal waves.

Direct application of the results of this idealized study to the generation of internal waves in the ocean is difficult. To begin with, the numerical simulations are in two dimensions and the laboratory experiments are quasi-two-dimensional. Possibly more importantly, ocean turbulence is much more complex than oscillating-grid turbulence and is forced by a variety of sources. As an example in the upper ocean boundary layer, turbulence created by surface wind stress is connected with a mean shear flow. However, the observed properties of the randomly-generated wave field in our experiments and simulations seem to be robust and may be indirectly useful in understanding the spectrum of waves in the ocean.

For an estimate of the scaling of the wave field generated in our simulations up to ocean scales we compare our results with the work of Garwood and Harcourt (1999) who used large-eddy simulations of the oceanic boundary layer in the Labrador Sea to examine the energy flux by turbulence-induced internal waves. They simulated a two-week episode of storm cooling in the freely convecting wintertime Labrador Sea using surface forcing from the surface wind stress and surface buoyancy flux provided by observational data. The buoyancy flux dominated over the wind stress, with convection cells mainly forcing the wave field. The wave field was broad-banded, with a peak frequency near N. Internal waves were observed with amplitudes reaching 30 m at the base of the mixed layer and 10 m in the pycnocline. They found that approximately $10^{-4}\mathrm{W/m^2}$, or 1% of the energy in the mixed layer was transported away by

downward-propagating internal waves.

In our random-forcing simulations, the energy flux into the mixed region is $10\mathrm{W/m^2}$. Details of the energy flux calculations are provided in Appendix C. The wave field has two regimes, as seen in Fig. 5.9. In the lower regime ($z < 58\,\mathrm{cm}$) the wave amplitudes are significantly smaller and carry an estimated $3 \times 10^{-16}\,\mathrm{W/m^2}$ away from the mixed region or $3 \times 10^{-15}\,\%$ of the mixed region energy. In the interfacial regime ($z > 58\,\mathrm{cm}$), wave amplitudes are approximately 2×10^3 times larger, and therefore carry away an estimated $1 \times 10^{-9}\,\mathrm{W/m^2}$ or $1 \times 10^{-8}\,\%$ of the mixed layer energy. Extending to the Labrador Sea, the energy flux by these latter waves would be $1 \times 10^{-10}\,\mathrm{W/m^2}$. Compared to the waves in the simulations of Garwood and Harcourt, the energy flux of these waves is about $1 \times 10^{-8}\,\%$ of those generated by the storm cooling. In our simulations, energy is injected at small enough scales that the energy within the mixed region reaches steady-state by viscous damping alone. Part of the discrepancy between these results may be due to the difference in energy injection scales.

The above calculations suggest that the randomly generated waves in our simulations may not constitute a significant energy sink for the oceanic surface mixed layer. However, turbulence is a source for high-frequency internal waves which are known to be a necessary component of the nonlinear interactions within the spectrum of internal waves in the ocean which ultimately drive mixing within the ocean interior (St.Laurent and Garrett 2002).

REFERENCES

Atkinson, J. F., Damiani, L., and Harleman, D. R. F. (1987) . A comparison of velocity measurements using a laser anemometer and a hot-film probe, with application to grid-stirring entrainment experiments. *Phys. Fluids*, 30(10):3290–3292.

Balmforth, N. J., Ierley, G. R., and Young, W. R. (2002) . Tidal conversion by subcritical topography. *J. Phys. Ocean.*, 32:2900–2914.

Briggs, D. A., Ferziger, J. H., Koseff, J. R., and Monismith, S. G. (1998) . Turbulent mixing in a shear-free stably stratified two-layer fluid. *J. Fluid Mech.*, 354:175–208.

Carruthers, D. J. and Hunt, J. C. R. (1986) . Velocity fluctuations near an interface between a turbulent region and a stably stratified layer. *J. Fluid Mech.*, 165:475–501.

Comte-Bellot, G. and Corrsin, S. (1971) . Simple Eulerian time correlation of full- and narrow-band velocity signals in grid-generated 'isotropic' turbulence. *J. Fluid Mech.*, 48:273–337.

Craik, A. D. D. and Leibovich, S. (1976) . A rational model for Langmuir circulations. *J. Fluid Mech.*, 73:401–426.

Crapper, P. F. and Linden, P. F. (1974) . The structure of turbulent density interfaces. *J. Fluid Mech.*, 65:45–63.

Dalziel, S. B. (1993) . Rayleigh-Taylor instability: Experiments with image analysis. *Dyn. Atmos. Oceans*, 20:127–153.

Dalziel, S. B., Hughes, G. O., and Sutherland, B. R. (2000) . Whole field density measurements. *Expt. Fluids*, 28:322–335.

Dickinson, S. C. and Long, R. R. (1978) . Laboratory study of the growth of a turbulent layer of fluid. *Phys. Fluids*, 21(10):1698–1701.

Dickinson, S. C. and Long, R. R. (1983) . Oscillating-grid turbulence including

effects of rotation. *J. Fluid Mech.*, 126:315–333.

Dohan, K. and Sutherland, B. R. (2002) . Turbulence time-scales in mixing box experiments. *Expt. Fluids*, 33:709–719.

Dohan, K. and Sutherland, B. R. (2003) . Internal waves generated from a turbulent mixed region. *Phys. Fluids*, 15:488–498.

E, X. and Hopfinger, E. J. (1986) . On mixing across an interface in stably stratified fluid. *J. Fluid Mech.*, 166:227–244.

Egbert, G. D. and Ray, R. D. (2000) . Significant dissipation of tidal energy in the deep ocean inferred from satellite altimeter data. *Nature*, 405:775–778.

Fernando, H. J. S. and DeSilva, I. P. D. (1993) . Note on secondary flows in oscillating-grid, mixing box experiments. *Phys. Fluids*, 5(7):1849–1851.

Fernando, H. J. S. and Hunt, J. C. R. (1997) . Turbulence, waves and mixing at shear-free density interfaces. Part 1. A theoretical model. *J. Fluid Mech.*, 347:197–234.

Fernando, H. J. S. and Long, R. R. (1983) . The growth of a grid-generated turbulent mixed layer in a two-fluid system. *J. Fluid Mech.*, 133:377–395.

Fjørtoft, R. (1953) . On the changes in the spectral distribution of kinetic energy for two-dimensional, nondivergent flow. *Tellus*, 5:225–230.

Garrett, C. and St.Laurent, L. (2002) . Aspects of deep ocean mixing. *J. Ocean.*, 58:11–24.

Hannoun, I. A. and List, E. J. (1988) . Turbulent mixing at a shear-free density interface. *J. Fluid Mech.*, 189:211–234.

Hinze, J. O. (1959) . *Turbulence. An Introduction to its Mechanism and Theory.* McGraw-Hill Book Company, Inc., New York.

Hopfinger, E. J. and Toly, J.-A. (1976) . Spatially decaying turbulence and its relation to mixing across density interfaces. *J. Fluid Mech.*, 78:155–175.

Kantha, L. H. and Clayson, C. A. (2000) . *Small Scale Processes in Geophysical*

Fluid Flows. Academic Press, San Diego.

Kit, E. L. G., Strang, E. J., and Fernando, H. J. S. (1997) . Measurement of turbulence near shear-free density interfaces. *J. Fluid Mech.*, 334:293–314.

Ledwell, J. R., Montgomery, E. T., Polzin, K. L., Laurent, L. C. S., Schmitt, R. W., and Toole, J. M. (2000) . Evidence for enhanced mixing over rough topography in the abyssal ocean. *Nature*, 403:179–182.

Linden, P. F. (1975) . The deepening of a mixed layer in a stratified fluid. *J. Fluid Mech.*, 71:385–405.

Llewellyn Smith, S. G. and Young, W. R. (2002) . Conversion of the barotropic tide. *J. Phys. Ocean.*, 32:1554–1566.

Long, R. R. (1978a) . A theory of mixing in a stably stratified fluid. *J. Fluid Mech.*, 84:113–124.

Long, R. R. (1978b) . Theory of turbulence in a homogeneous fluid induced by an oscillating grid. *Phys. Fluids*, 21(10):1887–1888.

McDougall, T. J. (1979) . Measurements of turbulence in a zero-mean-shear mixed layer. *J. Fluid Mech.*, 94:409–431.

McEwan, A. D. (1971) . Degeneration of resonantly-excited standing internal gravity waves. *J. Fluid Mech.*, 50:431–448.

McEwan, A. D. and Plumb, R. A. (1977) . Off-resonant amplification of finite internal wave packets. *Dyn. Atmos. Oceans*, 2:83–105.

McGrath, J. L., Fernando, H. J. S., and Hunt, J. C. R. (1997) . Turbulence, waves and mixing at shear-free density interfaces. Part 2. Laboratory experiments. *J. Fluid Mech.*, 347:235–261.

Munk, W. and Wunsch, C. (1998) . Abyssal recipes II: Energetics of tidal and wind mixing. *Deep Sea Res.*, 45:1977–2010.

Oster, G. (1965) . Density gradients. *Sci. Am.*, 213:70.

Perera, M. J. A. M., Fernando, H. J. S., and Boyer, D. L. (1994) . Turbulent mixing

at an inversion layer. *J. Fluid Mech.*, 267:275–298.

Polzin, K. L., Toole, J. M., Ledwell, J. R., and Schmitt, R. W. (1997) . Spatial variability of turbulent mixing in the abyssal ocean. *Science*, 276:93–96.

R. W. Garwood, J. and Harcourt, R. R. (1999) . Large-eddy simulation of pressure transport below the mixed layer. In Müller, P. and Henderson, D., editors, *Dynamics of Oceanic Internal Gravity Waves, II: Proceedings of the 11th 'Aha Huliko'a Hawaiian Winter Workshop, 1999*, pages 189–196. SOEST Special Publication.

St.Laurent, L. and Garrett, C. (2002) . The role of internal tides in mixing the deep ocean. *J. Oceanogr.*, 58:11–24.

Sutherland, B. R. (1996) . The dynamic excitation of internal gravity waves in the equatorial oceans. *J. Phys. Oceanogr.*, 26:3214–3235.

Sutherland, B. R. (2001) . Finite-amplitude internal wavepacket dispersion and breaking. *J. Fluid Mech.*, 429:343–380.

Sutherland, B. R., Dalziel, S. B., Hughes, G. O., and Linden, P. F. (1999) . Visualisation and measurement of internal waves by "synthetic schlieren". Part 1: Vertically oscillating cylinder. *J. Fluid Mech.*, 390:93–126.

Sutherland, B. R. and Peltier, W. R. (1994) . Turbulence transition and internal wave generation in density stratified jets. *Phys. Fluids A*, 6:1267–1284.

Tennekes, H. and Lumley, J. L. (1972) . *A First Course in Turbulence.* The MIT Press, Cambridge, Massachusetts.

Thompson, S. M. and Turner, J. S. (1975) . Mixing across an interface due to turbulence generated by an oscillating grid. *J. Fluid Mech.*, 67:349–368.

Trenberth, K. E. and Caron, J. M. (2001) . Estimates of meridional atmosphere and ocean heat transports. *J. Climate*, 41:3433–3443.

Turner, J. S. (1973) . *Buoyancy Effects in Fluids.* Cambridge University Press, Cambridge, England.

Voropayev, S. I. and Fernando, H. J. S. (1996) . Propagation of grid turbulence in homogeneous fluids. *Phys. Fluids*, 8(9):2435–2440.

Appendix A

Linear Internal Wave Properties

We begin with the linearized equations of motion for a continuously stratified, incompressible inviscid fluid in two dimensions (x and z), for which there is no mean background flow. If in addition we make the Boussinesq approximation in which we assume that the density varies slowly with height and replace the full density term ρ_T in front of the material derivative by a typical value for the density, ρ_0, the equations are

$$\begin{aligned} \rho_0 \frac{\partial u}{\partial t} &= -\frac{\partial p}{\partial x} \\ \rho_0 \frac{\partial w}{\partial t} &= -\frac{\partial p}{\partial z} - \rho g \\ \frac{\partial \rho}{\partial t} + w \frac{d\bar{\rho}}{dz} &= 0 \\ \frac{\partial u}{\partial x} + \frac{\partial w}{\partial z} &= 0. \end{aligned} \tag{A.1}$$

In these equations ρ and p are the perturbation density and pressure defined

by

$$\rho_T = \overline{\rho(z)} + \rho(x,z,t) \tag{A.2}$$

$$p_T = \overline{p(z)} + p(x,z,t), \tag{A.3}$$

where the background pressure and density are in hydrostatic balance:

$$\frac{d\overline{p}}{dz} = -\overline{\rho}g. \tag{A.4}$$

Combine the previous equations for a single equation in the vertical velocity, w,

$$\frac{\partial^2}{\partial t^2}\nabla^2 w + N^2\frac{\partial^2}{\partial x^2}w = 0 \tag{A.5}$$

where

$$N^2 = -\frac{g}{\rho_0}\frac{d\overline{\rho}}{dz} \tag{A.6}$$

is the buoyancy frequency.

We will look for periodic solutions for the field variables of the form

$$q = A_q \exp\left[i(k_x x + k_z z - \omega t)\right], \tag{A.7}$$

where k_x is the horizontal wavenumber, k_z is the vertical wavenumber, ω is the frequency, and it is understood that we take the real portion of equation(A.7).

Substituting

$$w = A_w \exp\left[i(k_x x + k_z z - \omega t)\right] \tag{A.8}$$

into equation(A.5) and assuming that N is constant yields the dispersion re-

lation

$$\omega = \frac{Nk_x}{\sqrt{k_x^2 + k_z^2}} = N\cos\Theta \tag{A.9}$$

where Θ is the angle of propagation of the wave to the vertical. The dispersion relation illustrates an important aspect of internal waves: the buoyancy frequency is the largest frequency for propagating waves. Waves with frequencies such that $\omega > N$ exponentially decay from their source and are called "evanescent" waves.

The phase velocity is

$$\mathbf{c_p} = \frac{\omega}{K}\frac{\mathbf{K}}{K} \tag{A.10}$$

where $\mathbf{K} = (k_x, k_z)$ is the wavenumber vector with magnitude K. The group velocity is the velocity of the energy transport and is defined by

$$\mathbf{c_g} = \frac{\partial\omega}{\partial k_x}\hat{\mathbf{i}} + \frac{\partial\omega}{\partial k_z}\hat{\mathbf{k}}. \tag{A.11}$$

In particular, the vertical group velocity is

$$\begin{aligned} c_{gz} &= \frac{\partial}{\partial k_z}\frac{Nk_x}{\sqrt{k_x^2 + k_z^2}} && \text{(A.12)} \\ &= -\frac{Nk_xk_z}{(k_x^2 + k_z^2)^{3/2}} && \text{(A.13)} \\ &= -\frac{N}{k_x}\sin(\Theta)\cos(\Theta)^2. && \text{(A.14)} \end{aligned}$$

It is interesting to note that

$$\mathbf{c_g} \cdot \mathbf{c_p} = 0, \tag{A.15}$$

so that the phase velocity is perpendicular to the group velocity.

Table A.1: Polarization relations for linear inviscid Boussinesq internal waves in the (x, z) plane. The complex amplitudes of horizontal velocity u, vertical velocity w, perturbation density ρ, perturbation pressure p, streamfunction ψ, and vorticity ζ are expressed in terms of vertical displacement, ξ. Included are the schlieren fields ΔN^2 and N_t^2.

$A_u = \imath \frac{k_z \omega}{k_x} A_\xi$	$= \imath N \sin\Theta A_\xi$
$A_w = -\imath\omega A_\xi$	$= -\imath N \cos\Theta A_\xi$
$A_\rho = (-d\bar{\rho}/dz) A_\xi$	$= \frac{\rho_0}{g} N^2 A_\xi$
$A_p = \imath \frac{\rho_0 N^2 k_z}{K^2} A_\xi$	$= \frac{\rho_0 N^2}{2k_x} \sin 2\Theta A_\xi$
$A_\psi = -\frac{\omega}{k_x} A_\xi$	$= -\frac{N}{k_x} \cos\Theta A_\xi$
$A_\zeta = -\frac{\omega}{k_x} K^2 A_\xi$	$= -N k_x \sec\Theta A_\xi$
$A_{\Delta N^2} = -\imath m N^2 A_\xi$	$= -\imath N^2 k_x \tan\Theta A_\xi$
$A_{N_t^2} = k_z \omega N^2 A_\xi$	$= -N^3 k_x \sin\Theta A_\xi$

The vertical displacement field, ξ, is given by

$$\frac{\partial \xi}{\partial t} = w. \tag{A.16}$$

By substituting plane wave solutions for the variables u, w, p and ρ into the equations of motion (A.1) the amplitudes can be expressed in terms of the amplitude for the vertical displacement, A_ξ. These are listed in Table A.1.

The vertical flux of horizontal momentum, given by the Reynolds stress $\rho_0 \langle uw \rangle$ (where the angled brackets denote averaging over one period), can be written in terms of A_ξ by

$$\rho_0 \langle uw \rangle = \frac{1}{4} \rho_0 N^2 A_\xi^2 \sin(2\Theta). \tag{A.17}$$

The maximum transport by internal waves occurs when $\Theta = 45°$.

The average kinetic energy per unit volume is

$$KE = \frac{1}{2}\rho_0\langle u^2 + w^2\rangle \tag{A.18}$$

$$= \frac{1}{4}\rho_0(1 + \frac{k_z^2}{k_x^2})\omega^2 A_\xi^2 \tag{A.19}$$

$$= \frac{1}{4}\rho_0(\frac{K^2}{k_x^2})\omega^2 A_\xi^2. \tag{A.20}$$

The average potential energy per unit volume is

$$PE = \frac{1}{2}\frac{\langle g^2\rho^2\rangle}{\rho_0 N^2} \tag{A.21}$$

$$= \frac{1}{4}\rho_0 N^2 A_\xi^2 \tag{A.22}$$

$$= E_k, \tag{A.23}$$

so that the total energy per unit volume is $E = 2PE = 2KE$. The vertical energy flux per unit horizontal area carried by waves of amplitude A_ξ is then

$$F_z = Ec_{gz} \tag{A.24}$$

$$= \frac{1}{2}\frac{\rho_0 A_\xi^2 N^3}{k_x}\sin\Theta\cos^2\Theta. \tag{A.25}$$

For fixed k_x, this is a maximum when $\Theta = \tan^{-1}(1/\sqrt{2}) \simeq 35°$.

Appendix B

Standing Wave Theory

We assume an inviscid Boussinesq fluid in the absence of any shear. For plane periodic waves, the linear dispersion relation is given by:

$$\omega = N\sqrt{\frac{k_x^2 + k_y^2}{k_x^2 + k_y^2 + k_z^2}} = N\cos\Theta \tag{B.1}$$

where k_x, k_y and k_z are the along-tank, across-tank and vertical wavenumbers, respectively, ω is the wave frequency and Θ is the angle of propagation to the vertical.

The largest scale internal waves observed in the experiments typically are a superposition of standing wave modes. In a bounded domain the range of wavenumbers is limited to a discrete number of modes. Requiring no normal flow out of the bottom or side walls of the tank, the vertical displacement field is given in a co-ordinate system with the origin at the bottom corner of the tank as follows:

$$\xi = A_\xi \cos(k_x^n x)\cos(k_y^m y)\sin(k_z^p z)e^{-i\omega t}. \tag{B.2}$$

Here A_ξ is the amplitude and the wavenumber components now hold the discrete values

$$(k_x^n, k_y^m, k_z^p) = (n\frac{\pi}{L}, m\frac{\pi}{W}, (p+1/2)\frac{\pi}{H}), \tag{B.3}$$

with n, m, and p being non-negative integers. Here L and W are the length and width of the tank, respectively, as shown in Fig. 2.1. The top of the stratified region, at $z = H$, is bounded by a turbulent region. In deriving (B.2) and (B.3) it is assumed that the amplitude of the waves with respect to z is largest at the base of the mixing region, the source of the internal wave energy.

Appendix C

Calculations of Internal Wave Energy Flux

In our random-forcing simulations, vorticity is input at amplitude F_0 into the mixed layer at each wavenumber within a range $(k_1 \leq k_x \leq k_2)$, $(k_1 \leq k_z \leq k_2)$ at each time step Δt. The vorticity forcing is related to the energy through a series of equations. First, the vorticity is related to the streamfunction by

$$\zeta = -\nabla^2 \psi \tag{C.1}$$

so that, following Appendix A, the complex amplitudes (denoted in this context by the zero subscript) are related by

$$\psi_0 = F_0 / K^2 \tag{C.2}$$

where K is the magnitude of the wavenumber. The velocity amplitudes are related to the streamfunction amplitude by

$$u_0 = -ik_z\psi_0, w_0 = ik_x\psi_0. \tag{C.3}$$

These equations combine to give

$$\frac{1}{2}(u_0^2 + w_0^2) = \frac{1}{2}(k_x^2 + k_z^2)\psi_0^2 = \frac{1}{2}K^2\psi_0^2 = \frac{1}{2}F_0^2/K^2. \tag{C.4}$$

Therefore, the energy spectrum of the forcing to the mixed region is defined in terms of the vorticity forcing amplitude as

$$E(K) = \frac{1}{2}\rho_0 F_0^2/K^2 \tag{C.5}$$

where $E(K)$ is the energy spectrum.

Assume F to be a typical rms value for the random variable F_0. The total energy input at each time-step is then

$$\begin{aligned} E_{total} &= \int_{k_{x1}}^{k_{x2}}\int_{k_{z1}}^{k_{z2}} E(\mathbf{K})d\mathbf{K} && \text{(C.6)} \\ &\approx C\frac{1}{2}\rho_0\int_{K_1}^{K_2}\frac{F_0^2}{K}dK && \text{(C.7)} \\ &\approx CF^2\rho_0\log(K2/K1), && \text{(C.8)} \end{aligned}$$

where C is an order(1) constant.

In our simulations, $F = 1.0\,\mathrm{s}^{-1}$ (per wavenumber, per timestep), $K2/K1 = 120/40 = 3$, $\rho_0 = 1.0\mathrm{g/cm}^3$ and $\Delta t = 0.002\,\mathrm{s}$.

The rate of energy input per unit volume is then $\approx 500\,\mathrm{g/(cm\ s^3)}$. The

"volume" of the mixed region is $40\times20\times1 = 800\,\mathrm{cm}^3$, assuming the simulations extend a unit width in the y-direction. The rate of total energy input is then $4\times 10^5\,\mathrm{g\,cm^2/s^3}$. In terms of ocean units, the total energy is $0.04\mathrm{kg\,m^2/s^3} = 0.04\mathrm{W}$. The possible energy flux from the mixed layer is then $0.04/(0.40)(0.01) = 10\mathrm{W/m^2}$.

The vertical energy flux by internal waves is

$$F_z = \frac{1}{2}\frac{\rho_0 A_\xi^2 N^3}{k_x}\sin\Theta\cos^2\Theta. \tag{C.9}$$

The amplitudes of the wave field are given in Fig. 5.9. At $z = 45\,\mathrm{cm}$, $A_\xi \approx 10^{-6}\,\mathrm{cm}$. This amplitude is an average measure for the spectrum of wavenumbers, k_x in the wavefield. The energy flux for a typical wavenumber $k_x = 0.5\,\mathrm{cm^{-1}}$ is then $F_z \approx 3\times10^{-13}\,\mathrm{g/s^3} = 3\times10^{-16}\,\mathrm{W/m^2}$.

Therefore, the vertical energy flux by the waves across a unit horizontal area is $3\times10^{-16}\,\mathrm{W/m^2}$ away from the mixed region or $3\times10^{-15}\,\%$ of the mixed region energy.

The amplitudes of the wave field within the interfacial region ($z > 58\,\mathrm{cm}$) are approximately 2×10^3 times larger, and therefore carry away an estimated $1\times10^{-9}\,\mathrm{W/m^2}$ or $1\times10^{-8}\,\%$ of the mixed layer energy.